Thesis

for obtaining a title of

Doctor of Chemical Engineering of Federal University of Rio Grande do Sul

and a title of

Doctor of Université de Lille 1

Speciality: Chimie organique, minérale, industrielle

by

Alexandre Antônio Bento Carvalho

Investigation of intrinsic activity of cobalt and iron based Fischer-Tropsch catalysts using transient kinetic methods

Thesis supervisor(s):

Andrei Khodakov, Nilson R. Marcilio

Defended on November 23rd, 2017

PANEL OF EXPERT EXAMINERS:

Dr Cuong Pham-Huu, DR CNRS, Université de Strasbourg, Reviewer

Professor Luiz Antônio Mazzini Fontoura, Lutheran University of Brazil, Reviewer

Professor Mark Saeys, Université de Gand

Professor Márcio Schwaab, Federal University of Rio Grande do Sul

Professor Nilson R. Marcilio, Federal University of Rio Grande do Sul

Dr Andrei Khodakov, DR CNRS, Université de Lille

INVITED EXAMINER

Dr Vitaly Ordomsky, E2P2L Laboratory, CNRS-Université de Lille-Solvay

Acknowledgements

Abbreviations, acronyms and symbols list

BET	Brunnett-Hemett-Teller	
CSTR	Continuous stirring reactor tank	
C_X	Gas phase concentration	mol/m$^3_{gas}$
EMSO	Environment for Modeling, Simulation and Optimization	
Fi in	Molar inlet flow	mmol/h
Fi out	Molar outlet flow	mmol/h
$F_V, total$	Total volumetric flow rate	m^3/s
FID	Flame Ionization Detector	
k_{ads}	Rate constant of adsorption	m^3/kg$_{cat}$ s
k_{des}	Rate constant of desorption	1/s
k_n $n = 1$ to 4	Rate constant of methanation reaction mechanism	1/s
N_{total}	Total number of active sites	µmol/g
N_i	Number of adsorbed species $(i = CO, CH_4)$	µmol/g
$NR_i(t)$	Normalized transient response of SSITKA curves	
R_w	Reaction rate of different species	mol/kg$_{cat}$ s
P	Pressure	bar
PDE	Partial Differential Equation	
PFR	Plug flow reactor	
SSITKA	Steady State Isotopic Transient Kinetic Analysis	
SCH_4	Methane selectivity	%
S_{CO_2}	Carbon dioxide selectivity	%
T	Temperature	ºC
t	time	s
TCD	Thermal conductivity detector	
TEM	Transmission Electron Microscopy	
TOS	Time on stream	h
TOF$_{SSITKA}$	SSITKA turnover frequency	s^{-1}

TOF turnover frequency based on cobalt dispersion and steady-state rate measurements of methane   s^{-1}

TPR-H$_2$	H$_2$ programmed temperature reduction	

TPH- MS	Temperature Programmed Hydrogenation with Mass Spectrometry	
V_R	Total volume of the reactor	m^3
W	Mass of catalyst	g
WGS	Water Gas Shift Reaction	
GHSV	Gas Hourly Space Velocity	mL/g_{cat} h
XAS	X-ray absorption spectroscopy	
XCO	CO conversion	%
XRD	X-ray diffraction	
τ_i	Surface residence time determined by SSITKA	s
τ	Surface residence time of the set of Partial Differential Equation (PDE)	s
ρ_b	Specific mass of catalyst bed	kg_{cat}/m^3_{bed}
ρ_{cat}	Specific mass of the catalyst	kg/m^3
ρ_{SiC}	Specific mass of SiC	kg/m^3
ε_{cat}	Catalyst pellet porosity	m^3_{gas}/m^3_{cat}
ε_b	Catalyst bed porosity	m^3_{gas}/m^3_{bed}

Contents

Table List

Chapter 1

Chapter 3

Chapter 4

Chapter 5

Figure List

Chapter 1

Chapter 2

Chapter 3

Chapter 4

Chapter 5

Chapter 6

RESUMO

O desempenho de catalisadores heterogêneos é geralmente atribuído a presença de sítios ativos. A concentração, a atividade intrínseca, a localização e a estabilidade destes sítios são os principais parâmetros de todos os sistemas catalíticos conhecidos. Métodos cinéticos transientes, como análise por SSITKA, são técnicas poderosas para o estudo cinético de reações catalíticas heterogêneas. Catalisadores à base de ferro com a presença de promotores metálicos (Bi e Pb) causaram notável aumento na taxa de produção de olefinas leves, criando a possibilidade de realizar a síntese de Fischer-Tropsch em condições amenas de reação e até mesmo em pressão atmosférica. Experimentos cinéticos transientes mostraram que a dissociação de CO é facilitada na presença de promotores devido a retirada de átomos de oxigênio pela ação do carboneto de ferro. O catalisador de cobalto suportado em zeólita mordenita apresentou maior valor da taxa de reação determinada por SSITKA entre todos os catalisadores suportados em zeólitas estudados. No entanto, ZSM-5 utilizada como suporte apresentou menor taxa de reação, provavelmente devido à localização das nanopartículas de cobalto na superfície externa da zeólita. A localização dos sítios ativos de cobalto em catalisadores bifuncionais formados por cobalto e zeólita apresentou grande impacto sobre a taxa de reação e em particular sobre a seletividade dos hidrocarbonetos. A proximidade entre os sítios ativos de cobalto e os sítios ativos de Brønsted demonstrou ser um parâmetro chave para obter uma alta seletividade e alto rendimento de hidrocarbonetos ramificados. O estudo combinando a análise SSITKA com técnicas de caracterização de catalisadores revelou que a deposição de carbono e a aglomeração de nanopartículas de cobalto durante a reação foram os responsáveis pela desativação do catalisador de cobalto suportado em sílica. A regeneração do catalisador via hidrogenação diminuiu o depósito de carbono e liberou parcialmente os sítios mais ativos para a dissociação de monóxido de carbono, assim como os sítios envolvidos na adsorção reversível de monóxido de carbono. A modelagem SSITKA demonstrou a presença de duas espécies intermediárias de carbono.

RESUMÉ

Les performances des catalyseurs hétérogènes sont généralement attribuées à la présence de sites actifs. La concentration, l'activité intrinsèque, la localisation et la stabilité de ces sites sont des paramètres importants de tous les systèmes catalytiques connus. Les méthodes cinétiques transitoires comme SSITKA sont des outils puissants pour mener à bien les études cinétiques des réactions catalytiques. La promotion des catalyseurs à base de fer avec des métaux utilisés pour la soudure (Bi et Pb) conduit à une augmentation remarquable de la vitesse de production des oléfines légères avec la possibilité d'effectuer la synthèse Fischer-Tropsch dans des conditions très douces (basse pression) voire pression atmosphérique. Les expériences cinétiques transitoires ont démontré la facilité de la dissociation du CO à la surface du carbure de fer en présence des promoteurs par le piégeage d'atomes d'oxygène. Parmi tous les catalyseurs étudiés, les catalyseurs à base de zéolite de type mordenite ont présenté la valeur la plus élevée de la constante de vitesse SSITKA. En revanche, la ZSM-5 utilisée comme support présentait une vitesse de réaction la plus basse, probablement à cause de la localisation de nanoparticules de cobalt uniquement à la surface externe de zéolite. La localisation des sites actifs de cobalt dans les catalyseurs bifonctionnels à base de zéolite et de cobalt a un impact majeur sur la vitesse de réaction et en particulier sur la sélectivité en hydrocarbures. La proximité entre les sites actifs de cobalt et les sites actifs de Brønsted a été considérée comme un paramètre clef pour obtenir une sélectivité et un rendement plus élevés en hydrocarbures ramifiés. Le SSITKA couplé à des techniques de caractérisation a révélé que le dépôt de carbone et l'agglomération des nanoparticules de cobalt étaient responsables de la désactivation du catalyseur cobalt supporté par la silice. Le dépôt de carbone a entraîné une diminution du nombre d'intermédiaires carbonés qui produisent du méthane via leur hydrogénation. La régénération des catalyseurs sous hydrogène diminue le nombre d'espèces de carbone déposées et libère partiellement les sites les plus actifs d'adsorption dissociative et les sites les plus forts d'adsorption réversible du monoxyde de carbone. L'étude de modélisation SSITKA a démontré la présence de deux intermédiaires carbonés.

ABSTRACT

The catalytic performance of heterogeneous catalysts is usually attributed to the presence of active sites. The concentration, intrinsic activity, localisation and stability of these sites are major parameters of all known catalytic systems. Transient kinetic methods such as Steady State Transient Kinetic Analysis (SSITKA) are powerful tools for carrying out kinetic studies of heterogeneous catalytic reactions. Promotion of iron catalysts with metals used for soldering (Bi and Pb) results a remarkable increase in the light olefin production rate with the possibility to conduct Fischer-Tropsch synthesis at very mild reaction conditions (low pressure) and even at atmospheric pressure. Transient kinetic experiments showed facilitation of CO dissociation in the presence of promoters by scavenging O atoms from iron carbide. Cobalt catalyst supported by mordenite zeolite presented higher value of SSITKA rate constant among all catalysts studied. On the other hand, the ZSM-5 as support presented the lowest reaction rate, probably due to the localization of cobalt nanoparticles on the external surface of the zeolite. Localization of cobalt active sites in bifunctional cobalt-zeolite catalysts has a major impact on the reaction rate and in particular on the hydrocarbon selectivity. A proximity between the cobalt active site and Brønsted active sites was found to be a key parameter to obtain higher selectivity and yield of isomerized hydrocarbons. SSITKA combined with catalyst characterization revealed that carbon deposition and cobalt nanoparticle agglomeration were responsible for the deactivation of silica supported cobalt catalysts. The carbon deposition led to a decrease in the number of carbon-chemisorbed intermediates, which yield methane through their hydrogenation. Catalyst rejuvenation in hydrogen lessened the amounts of deposited carbon species and partially released the most active sites of carbon monoxide dissociative adsorption and stronger sites of carbon monoxide reversible adsorption. The SSITKA modeling demonstrated the presence of two intermediates carbon species.

General introduction

Fischer-Tropsch synthesis (FTS) represents a unique opportunity for manufacturing clean fuels and chemicals from both renewable and fossil resources [1-6]. In Fischer-Tropsch (FT) technologies, fossil and renewable resources are first converted to syngas (mixture of carbon monoxide and hydrogen) via gasification, steam reforming and/or partial oxidation. The syngas then reacts on metal, carbide or sulfide catalysts to yield the value-added products.

Different transition metals from Group VIII are used in FTS (e.g., cobalt, nickel, iron and ruthenium). Cobalt catalysts are suitable for the synthesis of middle distillates and waxes. Benefits of cobalt include are highest FT reaction rates compared to iron, a high selectivity to linear paraffins and low water–gas shift (WGS) activity. Considering high cost of cobalt, a high productivity and an extended catalyst life are required to make the FT process economically feasible [3, 7].

Transient kinetic methods including the steady state isotopic transient kinetic analysis (SSITKA) are powerful techniques for the kinetic investigation of heterogeneous catalytic reactions at molecular level. Originally developed by Happel [8] and Biloen [9], SSITKA can be used to determine site heterogeneity, concentration of different types of adsorbed reaction intermediates, surface residence time, activity distributions and site coverage [10] by inclusion of one or more stable isotopic labels in a reactant species [11].

SSITKA has been used to evaluate the effect of different promoters, support modification and cobalt particle size [6, 12-19] on the type, concentration and reactivity of the surface intermediates. SSITKA can be particularly useful to identify the origin of the loss of activity and selectivity, because it yields independent information about the number of active sites and their intrinsic activity.

The goal of the thesis is to evaluate the intrinsic activity and localization of active sites in cobalt and iron based catalysts using a combination of transient kinetic methods such as SSITKA, extended physico-chemical characterization and catalytic tests under realistic conditions.

_____

The present manuscript is divided into six chapters. Chapter 1 presents a literature review on FT synthesis and SSITKA methodology. Chapter 2 introduces the methods for catalyst preparation and characterization. Special attention is paid to the SSITKA technique and to the experimental and modeling procedures. Chapter 3 presents the role of promoters for iron and cobalt catalysts as well the effect of the zeolites structure on the catalytic performance and surface kinetic parameters. Chapter 4 presents a synthesis procedure to obtain cobalt-zeolite composite materials using an extraction with a heteropoly acid. Chapter 5 describes the SSITKA evaluation of the deactivation mechanism during FTS with pure syngas and syngas containing nitrogen compounds. Additionally, Chapter 5 demonstrated the manner in which the regeneration procedure affects the FT reaction at molecular level and results of SSITKA kinetic modeling. Chapter 6 presents the general conclusions and perspectives of the thesis.

Major results of this thesis are published in the following articles:

Carvalho, A.; Ordomsky, V. V.; Luo, Y.; Muniz, A. R.; Marcilio, N. R.; Khodakov, A. Y., Elucidation of deactivation phenomena in cobalt catalyst for Fischer-Tropsch synthesis using SSITKA. *Journal of Catalysis*, 2016, *344*, 669-679.

Carvalho, A.; Marinova, M.; Batalha, N; Marcilio, N.R., Khodakov, A. Y; Ordomsky, V.V. Design of pure pore incorporated metal-zeolite composite for highly efficient synthesis of isomerized hydrocarbons by Fischer-Tropsch synthesis. *Catalysis Science & Technology*, 2017, *7*, 5019−5027.

Ordomsky, V. V.; Carvalho, A.; Legras, B.; Paul, S.; Virginie, M.; Sushkevich, V. L.; Khodakov, A. Y., Effects of co-feeding with nitrogen-containing compounds on the performance of supported cobalt and iron catalysts in Fischer–Tropsch synthesis. *Catalysis Today*, 2016, *275*, 84−93.

Cheng, K.; Subramanian, V.; Carvalho, A.; Ordomsky, V. V.; Wang, Y.; Khodakov, A. Y., The role of carbon pre-coating for the synthesis of highly efficient cobalt catalysts for Fischer–Tropsch synthesis. *Journal of Catalysis*, 2016, *337*, 260−271.

Ordomsky, V. V, Luo, Y, Gu, B, Carvalho, A., Chernavskii, P. A.; Cheng, K., Khodakov, A. Y. Soldering of iron catalysts for direct synthesis of light olefins from syngas under mild reaction conditions. *ACS Catalysis*, 2017, *7*, 6445−642.

References

1.   Dry, M. E., *Catalysis today* **2002**, *71* (3), 227-241.

2.   Iglesia, E., D., *Applied Catalysis A: General* **1997**, *161* (1), 59-78.

3.   Khodakov, A. Y.; Chu, W.; Fongarland, P., *Chemical Reviews* **2007**, *107* (5), 1692-1744.

4.   van Steen, E.; Claeys, M., F., *Chemical engineering & technology* **2008**, *31* (5), 655-666.

5.   Van Santen, R. A.; Ciobica, I. M.; Van Steen, E.; Ghouri, M. M., *Advances in catalysis* **2011**, *54*, 127.

6.   van de Loosdrecht, J.; Ciobîcă, I. M.; Gibson, P.; Govender, N. S.; Moodley, D. J.; Saib, A. M.; Weststrate, K.-J.; Niemantsverdriet, J. W., *ACS Catalysis* **2016**.

7.   Saib, A. M.; Moodley, D. J.; Ciobîcă, I. M.; Hauman, M. M.; Sigwebela, B. H.; Weststrate, C. J.; Niemantsverdriet, J. W.; van de Loosdrecht, J. *Catalysis Today* **2010**, *154* (3–4), 271-282.

8.   Happel, J., *Chem. Eng. Sci.* **1978**, *33*, 1567.

9.   Biloen, P., *J. Mol. Catal.* **1983**, *21*, 17.

10.   Yang, J.; Chen, D.; Holmen, A. *Catalysis Today* **2012**, *186* (1), 99-108.

11.   Shannon, S. L.; Goodwin, J. G., *Chemical Reviews* **1995**, *95* (3), 677-695.

12.   den Breejen, J. P.; Radstake, P. B.; Bezemer, G. L.; Bitter, J. H.; Frøseth, V.; Holmen, A.; Jong, K. P. d., *Journal of the American Chemical Society* **2009**, *131* (20), 7197-7203.

13.   Govender, N. S.; de Croon, M. H. J. M.; Schouten, J. C. *Applied Catalysis A: General* **2010**, *373* (1–2), 81-89.

14.   Lohitharn, N.; Goodwin Jr, J. G., *Journal of Catalysis* **2008**, *257* (1), 142-151.

15.   Jongsomjit, B.; Panpranot, J.; Goodwin, J. G., *J. Catal.* **2003**, *215*, 66.

16.   van Dijk, H. A. J.; Hoebink, J. H. B. J.; Schouten, J. C., *Chemical Engineering Science* **2001**, *56* (4), 1211-1219.

17.   Rothaemel, M.; Hanssen, K. F.; Blekkan, E. A.; Schanke, D.; Holmen, A., *Catalysis Today* **1997**, *38* (1), 79-84.

18.   Ha, v. D., The Fischer-Tropsch synthesis: a mechanistic study using transient isotopic tracing. **2001**.

19.   Efstathiou, A. M.; Gleaves, J. T.; Yablonsky, G. S.; Che, M.; Vedrine, J. C., *Characterization of Solid Materials and Heterogeneous Catalysts: From Structure to Surface Reactivity*. **2012**; p 1013.

Chapter 1. Literature review

1.1 Fischer Tropsch synthesis

Fischer Tropsch synthesis (FTS) is a chemical process used to convert syngas (mixture of carbon monoxide and hydrogen) in a mixture of long chain hydrocarbons and oxygenated species (Figure 1.1). Franz Fischer and Hans Tropsch discovered the process in 1922 employing an iron-based catalyst [1, 2]. Due to its fast technological development, FTS was already a commercial process in 1930.

Figure 1.1 Transformation of non-petroleum carbon resources into liquid fuels and chemicals via syngas. Reproduced from Zhang et al. [3].

The FTS process is interesting for both academic and commercial purposes. However, its economic importance has been oscillating during recent history (post II World War). Accordingly to Van Dijk [4], FTS importance depends on the following four criteria:

- o The world reserves of carbon-containing resources;
- o Geographic location of carbon reserves;
- o Demand for cleaner feedstock;
- o Demand for reduction of CO_2 emissions.

FTS technologies are named according to the used carbon feedstock, for example, the processes of Coal to-Liquids (CTL), Gas-to-Liquids (GTL) and Biomass-to-Liquids (BTL). This reference is recognized as XTL ("Anything-to-Liquids") processes [5].

FTS involves a complex system of reactions with a desired and undesired products formed (see list below). Commonly, the desired products are olefins, paraffins and alcohols (compounds with greater commercial value) and the undesired may be methane and coke [1].

Desired reaction:

Olefin: $\qquad nCO + 2nH_2 \rightarrow nH_2O + C_nH_{2n}$

Paraffin: $\qquad nCO + (2n+1)H_2 \rightarrow nH_2O + C_nH_{2n+2}$

Alcohols: $\qquad nCO + 2nH_2 \rightarrow C_nH_{2n+1}OH + (n-1)H_2O$

Undesired reaction [6, 7]:

Water Gas Shift Reaction (WGS): $\qquad CO + H_2O \rightarrow H_2 + CO_2$

Boudouard reaction (carbon deposition) : $\qquad 2CO \rightarrow C + CO_2$

Formation of metal carbides: $\qquad yC + xM \rightarrow M_xC_y$

Oxidation of metal: $\qquad xM + H_2O \rightarrow MO_x + H_2$
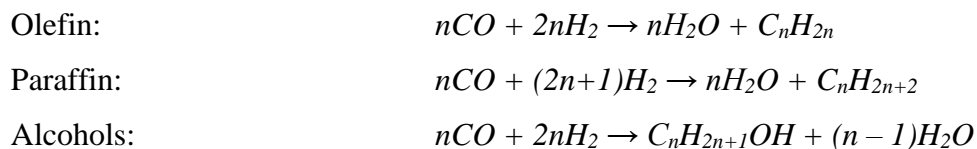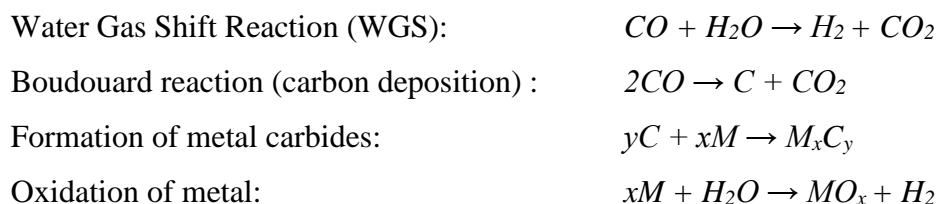
As showed above the FTS produces a wide-ranging distribution of hydrocarbons. The reaction selectivity is described typically using the Anderson–Schulz–Flory (ASF) distribution model [8]. In the ASF distribution, the molar fraction (M_n) of the hydrocarbon product with a carbon number of n preferably depends only on the chain-growth probability(α), which is a function of the rates of chain growth and chain termination. Equation 1 determines the ASF distribution model.

_____

$$M_n = (1 - \alpha) \cdot \alpha^{n-1} \hspace{4cm} (1)$$

FTS usually occurs at reaction conditions far from equilibrium [9]. Consequently, the product yields and selectivities are controlled by the reaction kinetics. The pressure applied are usually in the range of 15 to 20 bar. FT reaction is highly exothermic, with an average heat reaction of approximately -40 kcal/gmol [1]; consequently, efficient heat removal is required. The process temperature is the parameter responsible for the large spectrum of the FTS product distribution. For that reason, two fundamental FTS operation modes are defined. They are the lower temperature Fischer Tropsch (LTFT) and high temperature Fischer Tropsch (HTFT) processes.

LTFT is characterized by temperatures between 200 °C and 240 °C and proceeds in the slurry bubble column (SBCR) and fixed bed reactors in industrial scale. Cobalt and iron catalysts are applied in this technology. The goal of LTFT is production of the C_1 - C_{100} linear paraffins and light olefins with a H_2/CO ratio between 1.7 and 2.15 [10]. Accordingly to Dai et al. [11] and De la Osa et al. [12] LTFT is the most promising route for production of transportation fuels and chemical feedstocks from natural gas, coal and biomasses.

HTFT processes are carried out in the range of 300 to 350 °C, and are generally applied to produce gasoline/naphta, olefins and oxygenates [13]. HTFT uses iron based catalysts and is usually performed in fluidized bed reactors.

1.1.1 Fischer Tropsch catalysts

The Fischer Tropsch catalysts make use of transition metals from the group VIII (iron (Fe), cobalt (Co), nickel (Ni), ruthenium (Ru) and rhodium (Rh)) as the active phase. Concerning the chemical state, there is a consensus that metallic cobalt (Co^o) and metallic ruthenium (Ru^o) act as the active phases for CO hydrogenation. For iron based catalysts, the iron carbides are recognized as the active phase [3]. Further investigation is necessary to identify and to understand how the chemical states of each catalyst affect FT catalytic performance. In the next paragraphs, special attention is given for iron and cobalt based catalysts.

Cobalt based catalysts presents the highest reaction rate, highest selectivity to linear paraffins, in particular at higher CO conversion, and low water–gas shift (WGS) activity. They are usually applied to obtain waxes and middle distillates [14, 15, 16]. In terms of cobalt catalyst design for FTS, De La Osa et al. [17] and Vosoughi [18] listed the general crucial factors as follows:

- o The support material with appropriate physico-chemical and textural properties;
- o The method of catalyst preparation with the inclusion of the precursor type, loading, drying, calcination and reduction procedures;
- o Optimum operational conditions in favor of higher CO conversion and C_{5+} selectivity.

The activation of cobalt catalysts in hydrogen converts cobalt oxide phases to metallic Co. The Co° as the active phase may exist in two different crystalline forms, i.e. fcc (face centered cubic) and hcp (hexagonal close packing) phases [19]. For bulk Co, the hcp-phase is more stable at lower temperatures, but the fcc-phase becomes more stable when the size of Co particles becomes less than 20 nm [20]. Several studies have pointed out that the hcp-phase Co° is more active than the fcc-phase Co° in silica and alumina supported catalysts [19, 21, 22]. In addition, the gas composition applied on the catalytic reduction may influence the metallic cobalt phase obtained as well the catalyst support. For example, Elbashir et al. [23] have noticed in the used FT catalysts, the fcc-phase on silica support, while the hcp-phase was detected on alumina support.

Cobalt catalytic performance is significantly affected by adsorption of $CO + H_2$ reactants and intermediates by active sites [18, 24]. Additionally, an increase in the CO conversion is reported to be the responsible for the changes in the product selectivity, e.g. decreasing the methane selectivity with simultaneously increasing the C_5+ hydrocarbon selectivity [25]. Moreover, at typical FTS conditions, the CO_2 selectivity also increases with increasing CO conversion. This correlates with the higher WGS reaction rate at high water partial pressures.

Fe may be described as the most complicated active metal due to the coexistence of several iron phases in the course of FT reaction [26]. These iron phases are: ε-Fe_2C, ε'-$Fe_{2.2}C$, Fe_7C_3, χ-Fe_5C_2 and θ-Fe_3C carbides as well as metallic iron, FeO and Fe_3O_4. This

_____

occurs because the activation energy to form iron carbides is lower or similar compared with the activation energy of the CO hydrogenation. The metallic iron phase is not stable under FT reaction conditions, but still can be present in the catalyst even at long time on stream [3, 27]. The spatial distribution of the active carbide particles on the support material plays an important role on the catalytic performance [28]. For example, Zhang et al. [3] observed that χ-Fe$_5$C$_2$ is the active phase for Fe-based catalysts.

The product selectivity of Fe catalysts depends both on FT activity and water–gas-shift (WGS) activity due to the fact that iron active phase is active in WGS reaction [25]. In terms of catalyst promoters, it is known that the alkali metals are able to suppress the methane selectivity and increase the selectivity to the C$_{5+}$ hydrocarbons. The commercial iron catalyst is a multicomponent system. Potassium (K) is a recognized promoter to tune the product selectivity, resulting into an improvement of the selectivity to higher molecular weight hydrocarbons [29, 30, 31]. Another iron promoter with interesting results is the manganese (Mn) because it is capable to increase the CO conversion activity and decrease methane selectivity. Copper (Cu) may improve the iron reduction and carbidisation, while silica (SiO$_2$) and alumina (Al$_2$O$_3$) supports acts for a structural improvement [32].

Rh-based catalysts have been pointed out as the most efficient for synthesis of the C$_{2+}$ oxygenates [33-35]. Ni-based catalysts are typically used to obtain methane [36, 37]. For that reason, carbon monoxide hydrogenation with Ni catalysts have been suggested as a substitute process for synthesis of substitute natural gas (SNG). In addition, Ni is a relatively inexpensive metal [38]. Iron based catalysts are well recognized to exhibit both FTS and water-gas shift (WGS) reaction [25, 39].

The FT active catalytic species are generally supported on high surface area supports such as silica, alumina or zeolites. In the group of oxide supports, titania, alumina and silica are commonly used in FTS. In the case of zeolite supports, ZSM-5 [32], zeolite Y, zeolite L, and beta have been applied for synthesis of metal–zeolite FT catalysts. Zeolite is a material with elementary building units of SiO$_4$ and AlO$_4$ tetrahedra. Adjacent tetrahedra are linked at their corners via a common oxygen atom. This results in an inorganic macromolecule with a structurally distinct three dimensional framework [40].

Zeolites are well known catalysts applied in the petrochemical and fine chemical industries [41, 42] due to their tunable acidity. Zeolites are characterized by high surface area and unique microporous structure that help to well disperse the catalyst active phase and obtain the shape selectivity.

As about disadvantages, zeolites with high Si/Al ratio can exhibit high selectivity for undesired low molecular weight hydrocarbons due to their strong hydrocracking activities [43]. Furthermore, the high zeolite acidity may lead to the difficulties to reduce metal oxides at cation exchange sites and can increase catalytic deactivation rates.

Only cobalt and iron based catalysts are considered economically feasible for large scale production [2, 39, 44, 45, 46, 47] and have deserved special attention in the literature. Because of high price and rarity, ruthenium has been restricted for research purposes or used as a promoter for cobalt catalysts [36, 48]. Nickel produces a high quantity of methane.

1.1.2 Bifunctional catalysts and their application in FTS

Bifunctional catalysts present two different active phases that assure catalytic sites for diverse reaction steps. Thus, the reaction occurs in successive steps involving two types of sites: metallic sites presenting the main function to hydrogenate and to dehydrogenate and acidic sites with the main function to crack or to isomerize [49]. These two types of sites affect the rate of different chemical steps, which can alter reaction pathways and consequently modify product distribution. Besides, a bifunctional process may require the diffusional steps of the intermediate species.

A conventional example of process using a bifunctional catalyst is isomerization of n-hexane into methylpentanes using platinum-silica aluminate catalyst. While the hydrogenation and dehydrogenation occur on platinum, the isomerization takes place on the acid sites.

Different steps of the reaction in bifunctional catalysts are catalyzed by different types of sites. If these steps occurs in series, both types of sites must be in proximity one to another.

_____

An advantage of the combination of a metal with an acid catalyst is the possible enhancement of the catalytic performance. This is due to the solid acid catalysts itself which suffers from fast deactivation by coking [50]. As commented by Guisnet [51], bifunctional redox-acid catalysts can decrease coke formation. Therefore, no longer a regenerative system is necessary and a new method of synthesis of catalysts to obtain less sensitives material to coking can be sidestepped.

As commented in the above section, the zeolites supply acid sites to the catalyst. Zeolites present properties to be an "ideal" (highly active, stable and selective) acid catalyst due to their high number of acid sites and highly activity. The addition of a metal to the zeolite framework often guarantees a catalyst with high metal dispersion [50].

Pure acid zeolites are capable to crack and isomerize pentanes and hexanes [49]. The activity, stability and isomerization selectivity are usually increased if a hydrogenation phase is added to the zeolite. Therefore, the nature and reaction routes performed by both acid and hydrogenation sites are extremely important for the stability and selectivity of bifunctional zeolite catalysts.

It is important to comment that the isomerization to cracking rate ratio depends also on the operating conditions applied and not only of the type of zeolite. Comparing zeolites with different structures is not an easy task. Furthermore, the isomer distribution is markedly dependent on the conversion [49].

Several groups reported [52, 53, 54] that the hydrocracking of FT heavy wax produces fuels in the middle distillate range. The bifunctional catalysts have been also tested in FTS in order to combine hydrocracking and isomerization of long-chain hydrocarbons in a single reactor to restrict hydrocarbon distribution to a specific range.

The hybrid or composite catalysts for FTS contain an active metal component, such as Co, Fe and Ru for the growth of the primary straight chained hydrocarbons [55] and an acid zeolite catalyst for cracking and isomerization. These two types of sites are applied in FTS to obtain isoparaffins or diesel fuels (C_{10}–C_{20} hydrocarbons) from the direct syngas conversion.

Different process configurations have been selected for the use of bifunctional catalysts in FTS. For example, dual-bed configuration of the catalytic reactor with the FT

catalyst in the first layer and the zeolite or metal/zeolite in the second was tested by Zhao et al. [56] and Botes et al. [54]. Additionally, different method of catalyst preparation, such as mechanical mixing of FT catalysts with the zeolite [57, 58, 59] or the impregnation of the metal into the zeolite [52] have been studied. Below are some results from the literature concerning use of bifunctional catalysis in FTS.

Botes et al. [54] proposed use of HZSM-5 in FTS in order to obtain high quality gasoline obtained by the step of skeletal isomerisation and aromatisation over acidic zeolites. The high quality is linked to the fact that the branched and aromatics hydrocarbons formed presented a high-octane value. The authors commented that addition of HZSM-5 to the Fischer–Tropsch process also improved production of gasoline range products due to the cracking of longer chain hydrocarbons and oligomerization of light olefins.

Liu et al. [58] applied mechanical mixture of hybrid catalysts using cobalt supported on silica (Co/SiO$_2$) and palladium supported on beta zeolite (Pd/BEA). The catalyst was applied for the direct production of gasoline ranged isoparaffins from syngas. They have found an interesting result about the effect of the interface between the Co/SiO$_2$ and Pd/beta hybrids catalyst in the granual and powdery mixture. The granular hybrid catalyst showed lower CH$_4$ selectivity and much higher isoparaffin selectivity than the powdery hybrid catalyst due to hydrogen spillover.

The spillover was also observed by Tsubaki et al. [59] using a catalyst prepared from a physical mixture of three catalysts with different roles (Co/SiO$_2$, Pd/SiO$_2$ and ZSM-5) in order to produce directly isoparaffin from syngas conversion. FTS and the hydrocracking of hydrocarbons occur in the same reactor. The hybrid catalyst life was remarkably extended after inclusion of Pd in the catalyst. In addition, Pd was able to decrease the methane selectivity. Hydrogenation of olefins was performed by the FT active metal catalyst, while the zeolite was able to perform wax cracking.

Sarpini et al. [60] made use of the hierarchical-zeolite-supported cobalt catalyst, synthesized by impregnation method, in wax hydrocraking to shorter-chain hydrocarbons. The selectivity to the gasoline range of the C$_5$-C$_{11}$ fraction was increased. Bessell et al. [55] used impregnation method to synthesize a series of cobalt catalysts supported by zeolites (ZSM-5, ZSM-11, ZSM-12 and ZSM-34). The authors concluded that the activity was

_____

related to the channel size of the zeolite support. The 12 membered ringed ZSM-12 supported catalyst was the most active, followed by the two 10 membered ringed ZSM-5 and ZSM-11 supported catalysts, while the predominantly 8 membered ringed ZSM-34 supported catalyst was the least active.

An example of the use of core-shell catalyst in bifunctional FT process is the work by Yang et al. [57]. The one-step synthesis of light isoparaffins from syngas via Fischer–Tropsch synthesis (FT) was performed using two types of core-shell-like zeolite capsule catalysts. Both catalysts effectively improved the selectivity to light isoparaffins, simultaneously depressing formation of heavy hydrocarbons, presenting a better catalytic performance than the traditional hybrid catalyst prepared by physical mixing.

Another example involving of bifunctional catalysis is the syngas conversion to higher alcohols named as HAS. This reaction can be performed over bifunctional catalysts with one type of site to catalyze non-dissociative CO adsorption for CO insertion and alcohol formation, and with the other site to dissociate CO and to form surface alkyl species [61].

In terms of zeolite material, ZSM-5 has been demonstrating to be an adequate support to combine both FTS and hydrocracking. It is due to the fact that ZSM-5 presents a specific porous structure, ability to perform shape selectivity, high acidity and resistance to coking and stability under FTS conditions [47, 55, 62]. It is important to remember that the choice of the preparation method for bifunctional catalysts for the direct synthesis of isoparaffins from syngas would depend on the zeolite acidity and its porous structure.

1.1.3 Basic concepts of Fischer-Tropsch reaction mechanism

The FT reaction mechanism is a topic widely studied in virtue of the relatively complexity of the subject [63]. Different approaches have been proposed over years, such as the carbide mechanism, CO insertion mechanism, hydroxycarbene mechanism and oxygenate enol mechanism. The reaction mechanism can be divided in elementary steps [64] to aid its understanding, as follow:

1) CO and H_2 adsorption;

2) CO activation or chain initiation;

3) Chain propagation;

4) Chain termination.

Among the four steps, the first step of CO and H_2 adsorption occurs on the metal sites of the catalyst surface. The second step, named CO activation, is a matter of debate due to possibility of two types of dissociation: CO dissociation directly on the metal surface or hydrogen assisted CO dissociation [64, 65, 66]. These two CO activation pathways are shown in Figure 1.2, and lead namely to the carbide mechanism and to the CO insertion mechanism (both are going to be explained later).
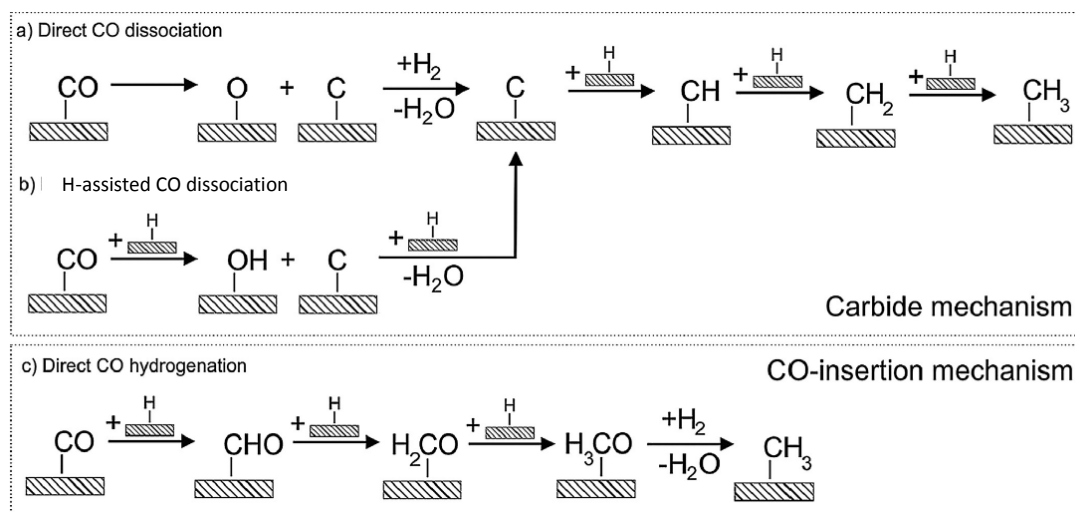
Figure 1.2 Examples of CO activation pathways: (a) direct CO dissociation (carbide mechanism); and (b) H-assisted CO dissociation (carbide mechanism); (c) CO hydrogenation (CO-insertion mechanism). Reproduced from Todic et al. [64].

The chain propagation and chain termination (steps 3 and 4) show that FTS proceeds through a stepwise addition of a monomeric intermediate.[65]. A description of each step is available in the literature [67, 68, 69].

Valero et al. [70] and Davis et al. [71] have pointed out the carbide mechanism and CO insertion mechanism as the most likely FT reaction pathway. Nevertheless, several

_____

alternative FT mechanisms have been proposed, making this topic still a subject of debates [72, 73].

The carbide mechanism, originally proposed by Fischer and Tropsch in 1926, suggests "polymerization of methylene groups" on the metal surface. Hence, the formation of hydrocarbon and oxygenate products includes metal carbide formation followed by its hydrogenation [71]. The carbide mechanisms involves one or two carbon pools on the surface that lead to formation of methane and higher hydrocarbons. In consequence, the reaction occurs on two types of active sites, one for CO dissociation and another for chain growth.

Another plausible pathway for the chain growth is the CO insertion [74]. In the initial step, CO is hydrogenated. Then, CO is inserted into the growing chain instead of CH_x as granted in the carbide mechanism.

1.2 Catalyst deactivation

Deactivation is the loss of the catalytic activity during the reaction. The catalyst deactivation causes loss of the active phase, recurrent startups and shutdowns of the reactor and replacement of the relatively expensive catalysts. Deactivation reduces the yield of valuable products and increases the operation costs [76]. Consequently, it has a great influence for both catalyst and reactor design. Deactivation is a complex problem, which involves occurrence of several intrinsic mechanisms [75].

The catalyst lifetime depends on several factors, i.e., reaction conditions, catalyst properties, feed purity, changes in reaction composition, among others. There is a wide variation in catalyst lifetimes among different processes, from 10^{-6} to 15 years [76]. In the case of methanation which typically make use of nickel supported catalysts, the lifetime of the catalyst varies from 5 to 10 years [76]. In the case of Fischer Tropsch synthesis, cobalt as metal phase is usually applied because presents high catalytic longevity as well high activity [1].

Heterogeneous catalysis deactivation phenomena can be classified as chemical, thermal and mechanical. Each class presents different intrinsic mechanisms, as briefly described in Table 1.1.

Table 1.1 Mechanisms of catalyst deactivation. Adapted from Argyle and Bartholomew [76].

Nature	Mechanism	Brief definition/description
Chemical	Poisoning	Strong chemisorption of species on catalytic sites which block sites for catalytic reaction
Mechanical	Fouling	Physical deposition of species from fluid phase onto the catalytic surface and in the catalyst pores
Thermal /chemical	Thermal degradation and Sintering	Thermally induced loss of catalytic surface area, support area and active phase-support reactions

A detailed description of chemical and mechanical deactivation phenomena is given in the review by Argyle and Bartholomew [76]. The next sub-section describes different deactivation mechanisms shown in Table 1.1.

1.2.1 Chemical deactivation

Poisoning is a deactivation phenomenon, which causes loss of activity due the presence of impurities in the feed stream. These impurities are able to block sites or to modify their catalytic performance. In addition to physically blocking of adsorption sites, adsorbed poisons may induce changes in the electronic or geometric structures of the surface [77]. The poisoning may be reversible or irreversible and it may be selective and non-selective as illustrated in Figure 1.3.

_____
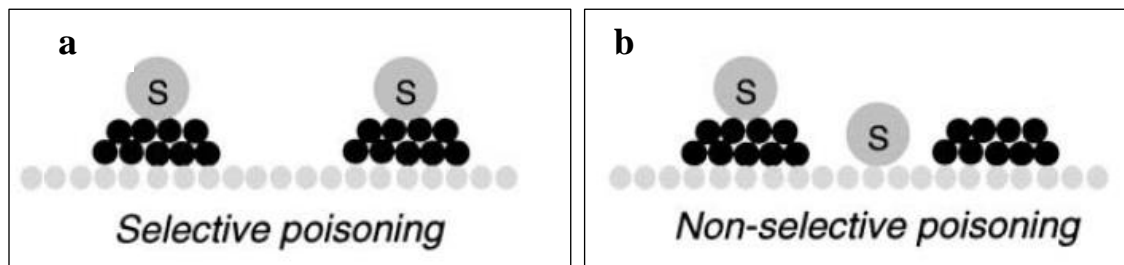
Figure 1.3 Two types of catalyst poisoning: selective to the active phase (a) and non-selective to the active phase (b). Black circles: active phase; gray circles: catalyst support Reproduced from Moulijn et al. [78].

Catalyst deactivation can be attributed to selective poisoning of the most active sites (see Figure 1.3a), which play the most important role in the catalytic reaction, while the total number of active sites can be only slightly reduced by the deactivation. Note that the molecules present in the feed streams are not the only responsible for poisoning of the metal active sites; the catalyst might also produce intermediates and products that act as lethal poisons for the active sites [78].

1.2.2 Thermal degradation

Thermal degradation of the catalysts usually occurs in the reactions conducted at high temperatures. The loss of activity may occur due to metal active phase and/or catalyst support modification with the following catalyst consequences [79]:

- loss of catalytic surface area due to crystallite growth of the catalytic phase;
- loss of support area due to the collapse of the support and catalyst surface area;
- chemical transformations of catalytic phases to non-catalytic phases.

The first two correspond to sintering. Sintering is often an irreversible process driven by loss of the surface energy due the crystallite growth. Generally occurs at reaction temperatures above the catalyst or support Tamman temperatures. A series of factors may influence the sintering rate on supported metals catalysts, from the catalyst material itself (type of metal and dispersion, presence of promoters, support surface area and its porosity and texture) to the operation conditions such as chemical composition of syngas,

___

conversion and gas space velocity [80]. It is known that an excessive heat provided by an exothermic reaction such as FTS may cause sintering, therefore this deactivation phenomena increases exponentially with the temperature of reaction. In addition, presence of impurities may also affect metal particle growth.

Bartholomew [79] has classified three main mechanisms of the metal crystallite growth as crystallite migration, atomic migration (or Ostwald ripening) and vapor transport. The third possible mechanism called vapor transport occurs only at very high reaction temperatures. The processes of crystallite and atomic migration are illustrated in Figure 1.4.
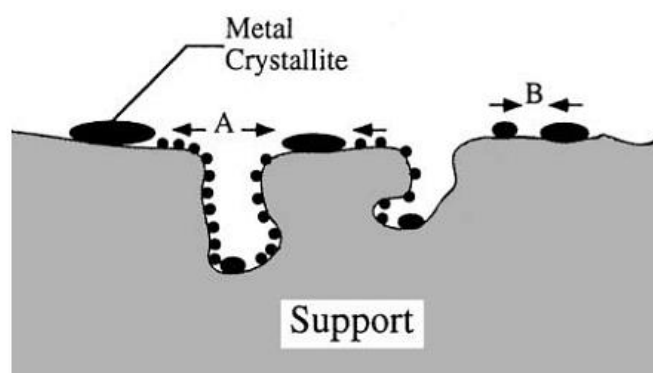
Figure 1.4 Two conceptual models for crystallite growth due sintering by (A) atomic migration or (B) crystallite migration. Reproduced from Bartholomew [79].

As described by Karaca et al. [21] and Bartholomew [79], the particle migration and coalescence involves migration of entire particles over the support and is followed by collision and coalescence. Atomic migration or ripening involves detachment of metal atoms from crystallites, migration of these atoms over the support surface and ultimately their capture by larger crystallites.

_____

1.2.3 Carbon fouling

This literature review is focused on the fouling phenomena. Fouling is the name attributed to the carbon and coke deposition, which are components capable to deactivate the catalyst by blockage of sites and/or support pores, as demonstrated in Figure 1.5.
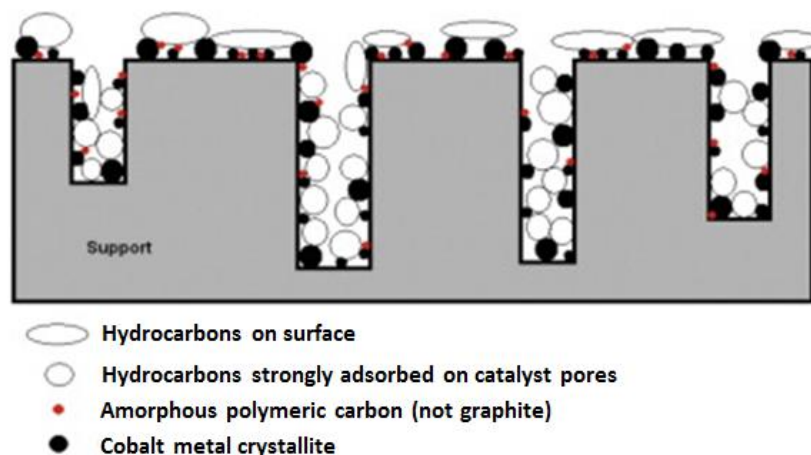
Figure 1.5 Example of surface and pore plugging of different carbon deposition on cobalt supported catalyst. Reproduced from Peña et al. [81].

According to Bartholomew [79] carbon is typically a product of CO disproportionation, while coke is produced by decomposition or condensation of hydrocarbons on catalyst surfaces and typically consists of polymerized heavy hydrocarbons.

Carbon and coke deposition exhibit a strong effect on the deactivation behavior. In the work by Menon [82], the precise location of the coke on catalyst surface was proposed, considering its nature, structure and morphology which has strongly influenced the deactivation behavior. All the catalytic reactions were classified as coke-sensitive or coke-insensitive [82]. A coke-sensitive reaction presents a negative effect of the coke on the activity at very low carbon content. The coke sensitive deactivation is a type of chemical deactivation and in many aspects is close to poisoning (see section 1.2.1). In the case of coke-insensitive reactions (e.g., methanation, Fischer–Tropsch synthesis, steam reforming

and catalytic reforming), the coke precursors only slightly affect the catalytic performance even at relatively high contents.

It is well known that most part of catalytic heterogeneous processes are carried out with metal particles dispersed on a support material. A wide range of supports may be used, and its heterogeneous structure can cause various interactions with the metal particles during reaction. For that reason, Bartholomew [79], described the possible effects of carbon or coke deposition on supported metal catalyst:

- carbon may strongly chemisorb as a monolayer or physically adsorb in multilayers. In both cases, the result is the blockage of reactants to the metal surface sites;
- the metal particle can be totally encapsulated by the carbon or coke;
- plugging micro- and/or mesopores of the support may block the reactant access to the metal particle sites.

1.3 Specific aspects of the deactivation of cobalt based Fischer–Tropsch catalysts

The FT reaction occurs under influence of several deactivation mechanisms. These mechanisms are strongly associated with the catalyst, reactor configuration and operation conditions. This section is dedicated to deactivation of cobalt based catalysts.

Cobalt catalyst deactivation is a major challenge in FTS [83]. In consequence, an improvement of catalyst stability is mandatory [75] to maintain the high hydrocarbon productivity. Cobalt catalysts deactivation might be caused by several mechanisms, such as sintering, metal oxidation, carbon deposition and carbidization. A series of results from the literature about sintering, carbon deposition and poisoning are discussed in the next paragraphs, as well as the cobalt activity behavior during deactivation.

_____

In the work by van de Loosdrecht et al. [84], several samples of cobalt supported on alumina were taken from a 100 bbl/d FT demonstration reactor operated at 230 °C, 20 bar, $H_2 + CO$ conversion of $50\% - 70\%$ and composition of $50-60$ vol % of H_2 and $30 - 40$ vol % of CO. Transmission electron microscopy (TEM) demonstrated a cobalt particle size increase from about 9 nm for the fresh catalyst to around 15 nm for the spent catalyst. The High-Angle Annular Dark Field (HAADF-TEM) clearly showed a rapid increase in the crystallite size during the first few days of FTS and after that, it levels off. This observation is also reported by Sadeqzadeh et al. [80] and Overret et al. [85].

Karaca et al. [21] concluded that cobalt sintering occurred already on the first hours of reaction (20 bar and 220 °C) for alumina-supported cobalt catalysts promoted with platinum. Consequently, a significant drop of the catalytic activity was observed. Kistamurthy et al. [86] applied TEM and X-ray spectroscopy (XPS) in a flat model catalyst of cobalt supported on silica before and after exposing the sample to FT conditions (20 bar, 230 °C, $H_2/CO = 2$) for 10 h. The authors concluded that temperature of 230 °C is too low for purely thermally induced loss of metal surface area. The most important conclusion was about the sintering mechanism. It was identified the dominance of Ostwald ripening in the flat model catalyst.

Deactivation study from a modeling point of view was examined in the work by Sadeqzadeh et al. [80]. The authors have been modeled a sintering mechanism for a FT slurry reactor using kinetic experimental parameters. A three-step sintering mechanism for cobalt-based catalysts including intermediate formation of an oxide layer on cobalt metal nanoparticles in presence of water was suggested. These results indicate that the sintering occurs mainly during the first hours of the reaction. Cobalt sintering proceeds faster when water is co-fed during the reaction.

Moodley et al. [87] reported about carbonaceous species observed on $CoPt/Al_2O_3$. The samples were taken from a slurry bubble column reactor operated over a period of 6 months at commercially FT conditions. Both Temperature Programmed Hydrogenation (TPH) and Temperature Programmed Oxidation (TPO) showed an increase in polymeric carbon with time on stream. Analysis of Energy-filtered transmission electron microscopy (EFTEM) and High Sensitivity-Low Energy Ion Scattering (HS-LEIS) demonstrated that

the polymeric carbon was located both on cobalt and alumina support. These results suggested the presence of an interaction between polymeric carbon and active phase, affecting the long-term deactivation of FT cobalt based catalysts. Table 1.2 shows the nature of carbon deposits reported in the literature.

Table 1.2 Carbon species observed by Moodley et al. [53] and literature.

Temperature of hydrogenolysis (°C)	Possible carbon species	References
250	Surface carbidic species (atomic carbon) Residual wax/hydrocarbons Bulk cobalt carbide	Lee et al. [88] Gruver et al. [89] Pankina et al. [90]
330	Residual wax (probably contained in small pores)	Gruver et al. [89]
445	Polymeric (amorphous) carbon on cobalt or the support	Lee et al. [88]

Peña et al. [91] also applied TPH with mass spectrometer (MS) and X-ray photoelectron spectroscopy (XPS), among others characterization techniques, to identify carbon species deposited on cobalt supported on alumina. FT activity was measured in a slurry type reactor at different FT operating conditions. Three types of carbon species were observed: residual hydrocarbons (probably wax), strongly adsorbed hydrocarbon fragments and amorphous polymeric carbon. Interestingly, graphene/graphite appears not to be produced even under low H_2/CO ratio feed condition.

Lee et al. [88] also have reported the formation of polymeric carbons on alumina-supported catalyst. It was suggested that hydrogenolysis of polymeric carbons occurred above 400 ºC. They observed that the carbon deposits significantly decreased both the

_____

activity and activation energy from 28-32 kcal/mol to 17-18 kcal/mol (117-134 kJ/mol to 71-75 kJ/mol).

Duncan et al. [92] and Pinard et al. [93] demonstrated negative effects of amorphous polymeric carbon on the catalytic activity due to physical blocking of the active sites. The authors reported that polymeric carbon in FTS could correspond to the polymerization of CH_x forming an alkyl group structure.

Nitrogen and sulfur compounds present in the syngas stream, mainly from coal and natural gas sources, are largely recognized as poisons for FTS catalysts [15, 94, 95]. Dry et al. [36], identified the minimum amount of sulfur (0.02 mg/m^3) content on syngas to avoid significant deactivation of iron and cobalt catalysts.

In the work by Visconti et al. [96], sulfur was fed within a wide range of concentrations (0-2000 ppm) to cobalt catalysts supported on alumina. A fixed bed reactor operating at 220 °C, 20 bar and H_2/CO ratio of 2 was applied. It was found that increasing sulfur amounts affected the catalyst reduction and also changed the product distribution. They observed a drop in wax formation and an increase in the selectivity to light products. However, the authors did not find any influence of the catalyst morphological characteristics on the deactivation rate.

The sulfur catalyst poisoning can be reduced by inclusion of alkali promoters. [97]. The catalyst was exposed to low (100 and 200 ppm) and high levels of sulfur (500 ppm). They have found that 500 ppm of sulfur led to a decrease of 80% in the reaction rate. The low-level of sulfur addition (100 ppm, 200 ppm) did not significantly influence the catalyst activity and selectivity. In presence of boron as promoter, the decrease in the reaction rate was less significant (only 35%).

In terms of activity, Van Berge et al. [14] demonstrated two regimes of deactivation for cobalt based catalysts applied in a FT plant, named "A" and "B". As demonstrated in Figure 1.6, syngas conversion decreased with time on stream, which suggests the FT deactivation behavior as a combination of several mechanisms. The first initial step (A) lasted for a few days and during this phase, the deactivation was considered reversible. The second long term regime (B) was associated to operations conditions and was considered irreversible [75].

_____
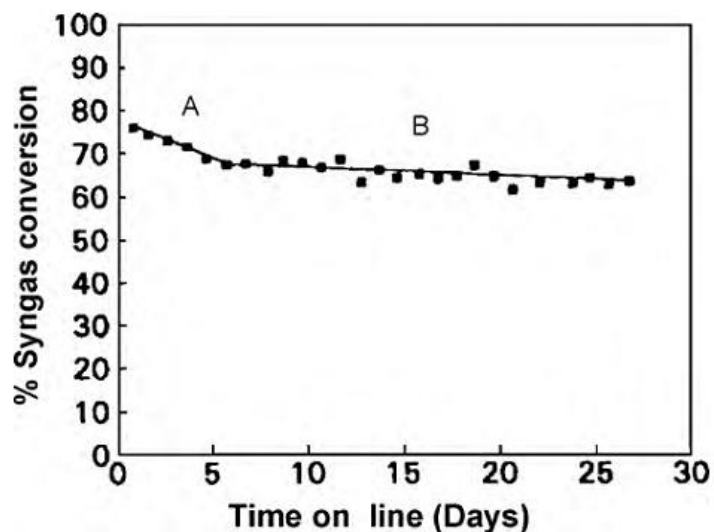
Figure 1.6 Deactivation regime for cobalt based catalyst. Synthesis conditions: 220 °C, 20 bar; commercial syngas feed: 50 vol% H_2, 25 vol% CO and 25 vol% inert; relative space velocity equal to 0.5. Reproduced from Van Berge et al. [14].

These studies show that catalytic deactivation is inevitable in cobalt FT process. However, several critical consequences of the deactivation may be avoided, postponed or even reversed with optimization of catalyst structure and operation conditions [98]. A way to reverse and minimize the effects of deactivation mechanisms is application of regeneration procedures. Next section is dedicated to discuss these procedures when they are applied to cobalt based catalysts.

1.4 Regeneration of cobalt based catalysts

This section presents a brief discussion about regeneration procedures and their application to FT cobalt catalysts reported in the literature. Regeneration is a widely studied topic in the patent literature in virtue of the necessity of improving the catalyst lifetime [98].

The lifetime of FT catalysts can be extended by regeneration and rejuvenation procedures [81, 84, 87, 99]. Regeneration of the catalyst can efficiently restore the activity and should be capable of removing poisons and coke from the surface, as well as to redisperse cobalt nanoparticles that have sintered. Diverse regeneration procedures of FT catalysts involve solvent washing, hydrogen treatment, steam treatment, and oxidative and reductive treatments [100]. Often the regeneration procedures include a combination of the above processes. In this section, only H_2 rejuvenation application is discussed, because this method of regeneration is applied in the present thesis.

Rejuvenation in hydrogen is one of the possible and most common ways to regenerate FT catalysts. The advantage of the reductive rejuvenation with hydrogen is that this treatment may be performed *in situ* in fixed bed, slurry or microreactors. The rejuvenation with hydrogen leads to the removal of most of carbon species and reversible poisons (e.g. nitrogen containing compounds) and possibly to the reduction of cobalt which might be partially oxidized in the presence of FT reacting medium (e.g. surface cobalt oxidation) [101]. Much smaller effect of treatment with hydrogen can be expected however on more refractory deposited atomic or polymeric carbon species [102].

As mentioned by Holmen and Rytter [98], some of the main industrial companies, major players in LTFT (Sasol, Exxon, Nippon Oil, ConocoPhillips, Syntroleum) have been applying regeneration procedures in slurry and fixed bed reactors, with cobalt supported on alumina and titania in presence of different promoters (platinum (Pt), rhenium (Re), ruthenium (Ru), manganese (Mn)).

Exxon company has patented [103] a FT process at 200 °C – 230 °C using a spent CoRu/titania catalysts. The H_2 rejuvenation was described as a successful method. It was also claimed that the promoter Ru helped the rejuvenation because of inhibition of carbon deposition.

The role of promoters has been discussed in different works. Morales [104] claimed that noble metals were capable to maintain "clean" the catalyst surface, avoiding catalyst deactivation and helping the regeneration procedure. Argawal et al. [105] applied CO hydrogenation using cobalt supported on alumina in an all-quartz internal-recycle reactor at temperatures between 200 °C and 400 °C from 0.1 to 20% CO in H_2 at atmospheric

_____

pressure. The authors observed cobalt carbide formation, which was caused by bulk carburization and growth of multilayer graphitic deposits. H_2 rejuvenation at 400 °C for 16 h was able to reactivate the catalyst by removing carbonaceous phases.

As pointed out in the previous paragraphs, hydrogen treatment has demonstrated its capacity of reducing carbonaceous phases from cobalt catalysts. Regeneration in hydrogen needs to be combined with other procedures, such as redox treatment and wax removal.

1.5 Steady-state isotopic-transient kinetic analysis (SSITKA)

Steady-state isotopic-transient kinetic analysis (SSITKA) is a technique applied to the kinetic study of heterogeneous catalytic reactions at molecular level. SSITKA determines surface kinetic parameters, such as the number of intermediates species (N_i), surface residence time (τ_i), SSITKA rate constant (R_{SSITKA}), site coverage and turnover frequency (TOF_{SSITKA}). It also provides valuable information about the catalyst surface species and it can be of great help in the identification of possible reaction mechanisms.

A general reversible heterogeneous catalytic reaction at steady-state is taken as example, where the reactant (R) is transformed into a product (P) through an adsorbed intermediate (X).

$$R \rightleftharpoons X \rightleftharpoons P$$

The inclusion of one or more stable isotopic labels in a reactant species (R) enables evaluation of parameters related to R, P, and X species under steady state condition. The experiment consists of an abrupt replacement of one of the reactants by its labeled isotopic counterpart (for example: ^{12}C to ^{13}C; H_2 to D_2 and ^{16}O to ^{18}O), while an inert tracer is abruptly removed from the feed. There is no change of the reaction intermediates present on the catalyst surface. Figure 1.7 illustrates a typical curve of the dynamic responses resulting of a SSITKA switch.

_____
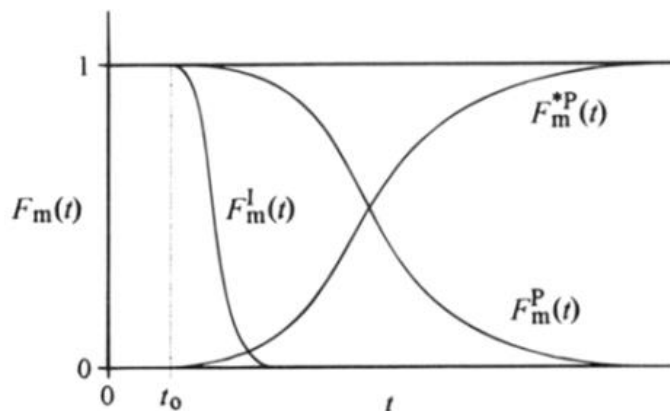
Figure 1.7 Typical normalized isotopic-transient responses in product species P following an isotopic switch in reactant, R - *R, which appears in the product as P - *P. An inert tracer, I, is simultaneously removed to determine the gas-phase holdup of the reactor. Reproduced from Shannon and Goodwin [106].

Figure 1.7 shows the transient responses of a differential-bed plug-flow reactor (PFR) following a step change in the isotopic labeling of reactant R to *R *labeled*, which subsequently appears in product as P to *P *labeled*. As explained by Shannon and Goodwin [106], the step-input response $(F^{*P}_m(t))$ is a statistical distribution representing the probability that an isotopic label remains adsorbed on the catalyst surface or appears in the effluent stream with time.

The nature of intermediates leading to the products may be diverse and the catalyst surface is composed by a system of interconnected pools, where each pool represents a homogeneous or well-mixed subsystem within the reaction pathway [106]. In the next section, the main measured SSITKA parameters are introduced.

1.5.1 SSITKA general parameters

SSITKA is a technique suitable to investigate the catalyst surface and reaction mechanisms at a near to molecular level under realistic and steady-state conditions. Surface residence time of reactants and products, and number of adsorbed reactant and intermediates leading to the products are identified as the fundamental SSITKA parameters. Moreover, the methodology may provide the coverage of surface intermediates, intrinsic turnover frequency (TOF), surface heterogeneity and/or reactivity distribution.

Surface residence time (τ_i) is a fundamental SSITKA parameter and its interpretation differs from reactants to products. For reactants, this parameter is related to the interaction between the gas phase and catalyst active sites. In the case of products, the value of τ_i represents the lifetime of intermediates. To properly interpret the surface residence time results, it is necessary to apply a correction regarding the chromatographic effect. This is required because the reactant may be adsorbed in the entire reaction system, not just in the reactor.

The chromatographic effect leads to a delay in the isotope composition in the gas phase as reported in the literature. According to Ledesma et al. [107], the chromatographic effects should be kept negligible in order to avoid its interference with the intrinsic kinetics. The effect can be neglected if the area between the response of the reactant and inert is less than 20% of the area between the response of the product and inert. A detailed explanation about the procedure used to obtain the surface residence time and chromatographic effect is given on the Chapter 2.

Another phenomenon required to interpret correctly the surface residence time is readsorption. According Shannon and Goodwin [106], it is difficult to avoid and to interpret the readsorption phenomena. The readsorption of products or intermediates on the catalyst surface builds up a delay on the products curve. Consequently, it affects negatively the activity and reaction rate. The effect is insignificant only if the product readsorbs on nonreactive sites.

_____

As commented above, readsorption creates a delay in the product response curves, which requires a suitable method for correction. The most common procedure consists in passing an inert gas in addition to reactants and products on the labeled or non-labeled lines. The inert gas curve is the fast one because there is non-adsorption of inert on catalyst surface. The area under the inert gas curve gives directly the value of its surface residence time.

The number of intermediate species (N_i) is the most general and accurate SSITKA parameter. It represents the amount of active intermediates (in terms of carbon atoms) on the surface that lead to the product. N_i is the actual number of reaction intermediates [108], providing a more accurate turnover frequency (TOF_{SSITKA}) compared to the TOF obtained from chemisorption and characterization techniques. It is one of the most important parameters due to its capacity to evaluate the role of promoters on different types of catalysts, the effect of catalyst aging, the identification of reaction mechanisms, among others.

TOF_{SSITKA} is another useful parameter that has been used to quantify the active intermediate reactivity. Literature presents different definitions of TOF_{SSITKA}. For example, Gao et al. [33] assumed TOF_{SSITKA} as the reciprocal of the surface residence time of intermediates leading to the product. Alternatively, Rohr et al. [109] Shannon and Goodwin [106] and Ledesma et al. [107], have defined it as reactivity for a pseudo first order reaction. According to Shannon and Goodwin [106], TOF_{SSITKA} is calculated as the ratio of surface coverage of the product (Φ) and its surface residence time (τ_i). The present work makes use of the latter TOF_{SSITKA} definition.

SSITKA also provides a value of rate constant (R_{SSITKA}) considering the number of intermediates leading to the products and reciprocal surface residence time of the same intermediates. Further explanation about how to obtain the parameters cited in this section is given on the Chapter 2.

1.5.2 SSITKA application

SSITKA has been used in several heterogeneous catalytic reactions [33, 110, 111, 112, 113]. Reactions and processes studied using this technique include:

o   Ammonia synthesis;
o   CO oxidation;
o   Phenol steam reforming;
o   Propene epoxidation;
o CH_4 oxidation;
o   Methanol decomposition/steam reforming;
o   Selective NO reduction;
o   Oxidative dehydrogenation;
o   Butane isomerization;
o   FTS.

SSITKA has brought information about reaction pathways, role of promoters and effects of the operating conditions on the coverage and number of intermediates, among others [107]. SSITKA has been used in Fischer-Tropsch synthesis to evaluate surface reaction parameters for various catalysts including iron, palladium (Pd), cobalt, rhodium and nickel. The next subsection presents examples of SSITKA use for investigation of FT processes.

1.5.2.1 Role of promoters

The role of promoters on catalyst performance has been investigated by SSITKA. Several promoters were studied, such as lanthanum (La), Pt, Ru, Re and also alkali (sodium (Na), potassium (K), lithium (Li)), manganese dioxide (MnO_2) and copper (Cu). The goal of the present section is to discuss the SSITKA results obtained for the promoted cobalt based catalysts.

Promoters may have an influence on the intrinsic activity, selectivity as well on the number of intermediates leading to the products [107]. Yang et al. [114] reported that rhenium promotion of Co catalysts led to a small increase in both number of intermediates and number of adsorbed CO molecules. However, no noticeable changes in the intrinsic site activity were found. The study suggests that Re might be able to slightly enhance CO adsorption, once the surface coverage of CO is about ten percent higher on the Re promoted sample. A SSITKA investigation by Schanke et al. [115] for cobalt supported on silica and alumina, revealed that an enhancement of CO hydrogenation rate occurred in the presence of Pt, due to the increase in both cobalt reducibility and dispersion of reduced cobalt particles.

In the case of alkali species (Na, K, Li), SSITKA studies have reported a decrease in the activity and number of intermediates, but an enhancement in the C_{5+} selectivity [116, 117]. Use of La and MnO_2 have also affected the number of intermediates and caused changes in the intrinsic activities [118, 119]. Promotion with Re also influences the site activity and number of reaction intermediates. However, according to Bertole et al. [120] the selectivity has not been altered by this promotion for cobalt catalysts supported on silica and titania. This observation is in agreement with other studies [121, 122]. Bertole et al. [120] also concluded that even the enhancement of cobalt reducibility by the promoter did not have any effect on the catalytic behavior.

The work by Enger et al. [110] investigated the effect of zinc (Zn) on cobalt catalysts supported on α and γ-alumina. The presence of Zn showed a loading-dependent and a negative influence under both SSITKA and FTS conditions. The promoter increased the surface residence time of active intermediates and decreased the CH_4 selectivity. Zn had no effect in all sites of cobalt catalysts due to the same amount of adsorbed CO in equilibrium with the gas phase.

The effect of catalyst support modification for FTS has been investigated by SSITKA, more specifically, to understand how the structure of supports affects the surface kinetic parameters. Moreover, the use of promoters in modified supports have gained attention.

In the study by Rane et al. [123] for cobalt supported on different alumina phases (ɣ, Φ, δ and α-Al$_2$O$_3$) a slightly change in the surface residence time of CO and CH$_x$ was detected. On the other hand, the number of intermediates was lower for ɣ and Φ-Al$_2$O$_3$ than for δ and α-Al$_2$O$_3$. The authors concluded that the active surface concentration of intermediates leading to products could be associated with the C$_{5+}$ selectivity observed at realistic FT conditions.

Kim Phan et al. [124] compared the macroporous structure of MPS-Al$_2$O$_3$ support with the conventional ɣ and α-alumina supports. The SSITKA investigations pointed out similar CH$_x$ residence times for all supports, suggesting an unchangeable intrinsic reaction rate for methane formation. In terms of CO surface residence time, the value for MPS-Al$_2$O$_3$ with Re as promoter was slightly higher compared to others supports. The amount of adsorbed CO was almost twice as high for the macro structure than that for the cobalt catalyst supported on α-Al$_2$O$_3$. Hence, MPS-Al$_2$O$_3$ seems to combine the advantages of ɣ and α-Al$_2$O$_3$ in terms of activity and selectivity.

Bertole et al. [120] studied unsupported and conventional supports (alumina, silica and titania) for cobalt based catalysts. In addition, modified supports with promoters (yttrium (Y), magnesium (Mg) and zinc oxide (ZnO)) were applied. Different support-modified catalysts revealed significantly lower site activity compared to those basic supported catalysts. The lowest site activity was measured with the unsupported cobalt catalyst. The authors commented that the same trend was observed for samples in presence of impurities that were difficult to eliminate during preparation, which could easily cause a loss of metal surface area.

The effect of adding zirconia (Zr) to the modified alumina support on cobalt catalysts has been investigated by Rohr et al. [109]. Zr was able to improve FTS activity. However, SSITKA results indicated that the intrinsic activity of cobalt was basically the same for the zirconia-modified and unmodified catalysts. Moreover, it was independent of the nature of the promoter. Similar results were obtained with a noble metal (Pt) promoted catalyst.

_____

The role of Zr on cobalt catalysts was also investigated by Jongsomjit [125]. The same trend for the intrinsic persisted even with an increase in the number of intermediates with Zr modification. The major impact of Zr is the increase in the concentration of active cobalt surface sites. Besides, the promoter presented ability to increase the cobalt reducibility.

1.5.2.2 Particle size

SSITKA technique has been successfully applied to understand the effect of catalyst particle size on the FTS. In the work by Den Breejen et al. [126] SSITKA was applied to investigate the origin of cobalt particle size effects. The authors claimed that the investigation was valid because the same trend of TOF and methane selectivity has been found at both FTS under conventional and SSITKA conditions for cobalt particle smaller than 6 nm. For carbon nanofiber supported cobalt catalysts, the cobalt particle range studied was between 2.6 nm and 16 nm at constant temperature (210 °C) and H_2/CO ratio feed equal to 10. The CH_x and CO residence times appeared independent of the size for cobalt particles larger than 6 nm. In addition, a lower TOF was observed, justified by the blockage of edge/corner sites and lower intrinsic activity at the small terraces.

Yang et al. [127] also investigated the effect of cobalt particle size by SSITKA using cobalt supported on alumina. The authors observed that the TOF remains constant as the particle increased from 4 nm to 15 nm, but an increase in the number of intermediates was noticed. In addition, the switches between hydrogen (H_2) and deuterium (D_2) were applied, helping to prove that the particle size did not change the kinetically relevant steps of the reaction.

Even though the literature cited above has showed that cobalt particle size might influence the activity and the yield of the samples, Iglesia et al. [121] and Borg et al. [128] commented that the effect of cobalt dispersion on the FTS performance is still not well understood for supported cobalt catalysts. The use of different supports could affect the real cobalt dispersion, causing a misinterpretation. For example, the use of carbon

nanofibers, which do not present interaction with active phase, may lead to different results compared to porous metal oxide supports (alumina, silica and titania). The metal oxide supported catalysts shows a varied interaction with the reactants, interfering differently with the active sites.

In the work by Tsai and Goodwin [108], the goal was to compare H_2 or CO chemisorption measurements with the adsorption study obtained by SSITKA under CO hydrogenation conditions. The chemisorption measurement provided metal particle size and metal dispersion. A comparative study of SSITKA (obtained after reaching steady-state reaction conditions) and static chemisorption results was carried out. It was found that SSITKA could be applied as a complementary technique to static chemisorption, XRD line broadening, and TEM for better characterizing metal dispersion (availability of surface metal atoms) and metal particle size.

1.5.2.3 Effect of operation conditions

SSITKA has been used to discern about influence of operation conditions on the kinetics. Frøset and Holmen [129] have found that neither CO partial pressure or space velocity influences the *in situ* CO adsorption on cobalt supported on ɣ-alumina with and without Re as promoter. At the reaction conditions, the intrinsic activity is slightly affected by space velocity, H_2/CO ratio (5, 10 and 15) and temperature (200 °C, 210 °C and 220 °C), while total pressure of 1.6 bar, 1.85 bar and 2.1 bar had only a negligible effect. The CH_4 and CO surface residence times were not affected by variation in total pressure. However, this variation has been slightly increased both TOF and CO reaction rate. A drop in methane selectivity was also observed.

Panpranot et al. [130] have studied the H_2 partial pressure effect on cobalt supported in two kinds of silica: amorphous and mesoporous MCM-41. The average CH_4 surface residence time consistently dropped with the increase in hydrogen partial pressure. The intrinsic site activity and concentration of surface intermediates for CO hydrogenation were strongly dependent on hydrogen partial pressure for both supports applied.

_____

Rohr et al. [109] noticed an unexpectedly increase in the surface coverage of reactive intermediates, for modified alumina supported on cobalt, at higher temperature applied (240 °C). This might occur due to the competition between reactive carbon-containing species and further species adsorption. The higher TOF (0.21 s^{-1}) was found at 240 °C and the lowest one (0.10 s^{-1}) at 210 °C. Nevertheless, TOF was found to be non-dependent on the pressure.

1.6 SSITKA modeling

This section presents methods usually applied for modeling SSITKA experiments. The use of such methodologies allows identifying and discriminating kinetic models among several proposed reaction pathways.

Different models were considered in the literature based on the continuous-stirred tank reactor (CSTR), plug-flow reactor (PFR) configurations [4, 107] or convolution/deconvolution techniques [107]. This section provides an introduction about mathematical techniques used to analyze SSITKA experimental data, focusing in the PFR approach, used in this thesis. A more complete description of mathematical methods used for analysis of SSITKA can be found in the review by Ledesma et al. [107].

The most common approach to mathematical analysis of SSITKA data comes from the approximation of the system as a transient plug flow reactor (PFR). The PFR modeling has been widely used to study SSITKA under methanation conditions. In a plug flow regime, all changes relative to the inlet signal are ascribed to chemical kinetics [131].

Accordingly to Ledesma et al. [107] the major benefit of PFR modeling compared to deconvolution and convolution methods is its ability to describe more complex processes compared to pseudo-first-order reactions. In addition, this model may take into account internal diffusion limitations, especially in microporous catalysts with fast heterogeneous reactions.

___

The PFR reactor model consists in a set of partial differential equations (PDE) corresponding to conservation of all species involved in the isotopic substitution, from both gas-phase and surface. This set of PDEs is solved using numerical methods, providing the concentration of each species as a function of time and axial position within the reactor. The general equations of the PFR model used to analyze SSITKA transient results will be presented and discussed in Chapter 2.

PFR modeling of SSITKA has been widely used to study the methanation reaction mechanism under Fischer–Tropsch conditions [4, 72, 107, 131, 132]. Diverse reaction pathways were proposed, as illustrated in Figure 1.8. The SSITKA modeling allows discriminating among distinct models, pointing out the most appropriate one to describe the experimental results. These models are based on the presence of two gas phase compounds (CO and CH_4) and on distinct surface components (CO adsorbed and C_α and C_β adsorbed intermediates species) [133, 134].
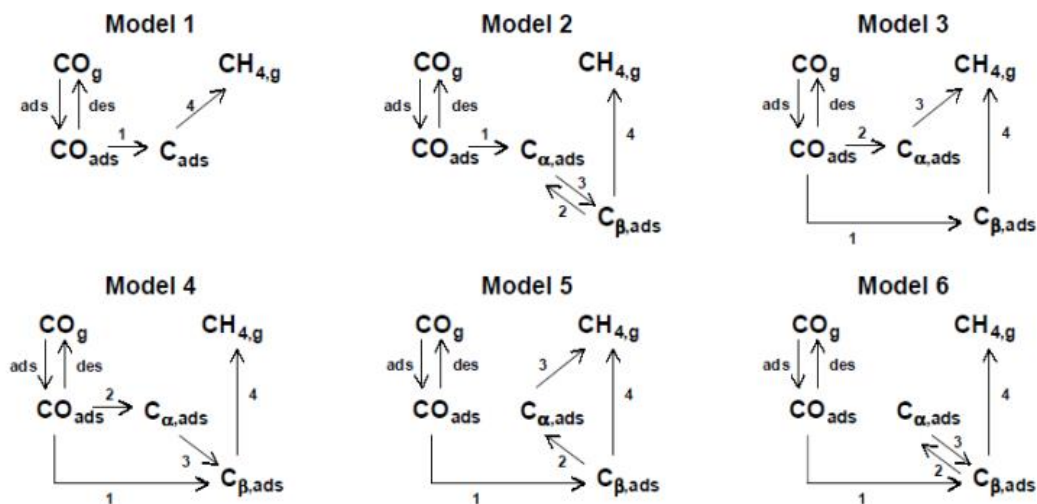
Figure 1.8 Possible reaction mechanisms for CH_4 formation from CO hydrogenation. Adapted from Van Dijk [4] and Ledesma et al. [107].

The models differ regarding the presence of one or two carbon pools and occurrence of parallel or competitive routes towards methane production in the case of two existing active pools. For example, Model 1 considers the existence of a single intermediate C species, while Models 2 to 6 considers two intermediate species, formed and consumed

through different routes. Models 2 and 6 consider the existence of buffer steps involving the intermediate species (reversible transformation of one intermediate into the other). The formation of hydrocarbons of higher molecular weight is not considered in the models presented; this approximation is valid when the reaction is carried out at lower pressures. Hence, the surface concentrations of $C_{\alpha,ads}$ and $C_{\beta,ads}$ are usually underestimated.

The six alternative mechanisms displayed in Figure 1.8 have been employed in the SSITKA modeling studies. For example, Govender et al. [131], observed for Fe based catalysts, that Models 3, 4 and 6 provided the best fits. An extension of the models to consider formation of higher hydrocarbon products by including C–C coupling reactions allowed further discrimination of models, resulting in two possible mechanisms, both characterized by the presence of two active pools of carbon intermediates (C_α and C_β) leading to methane formation.

The existence of two carbon pools was also observed in the SSITKA work by Van Dijk et al. [72] for cobalt promoted with Ru and supported on titania. It was concluded that two single C species were present on the catalyst surface, and both participated in methane and higher hydrocarbons formation. Accordingly to Yang et al. [132], these carbon pools correspond to CH_2O and CH_x, species associated to two reaction pathways for methane formation.

1.7 General conclusion

The literature presents a significant number of publications about FTS and FT catalysts. Cobalt and iron catalysts seem to optimal systems for synthesis respectively of middle distillates and light olefins. Selectivity and stability are currently the most important challenges in most of FT processes.

The research of different groups addresses design of bifunctional catalysts on the basis of cobalt and acid catalysts to improve the selectivity of FTS to the desired hydrocarbon fractions: usually gasoline and diesel type fuels. Co/zeolites catalysts have shown promising catalytic performance in this reaction. The effect of several important catalyst characteristics on the reaction performance need to be however elucidated and in

particularly the effect of the zeolite acidity and mesoporosity on the reaction rate and selectivity.

Iron catalysts are the catalysts of choice for synthesis of light C_2-C_4 olefins. The catalytic activity and in particular selectivity seems to be however insufficient for industrial implementation of this reaction. Promotion of iron catalysts opens interesting perspectives for the improvement of the yields of light olefins in this reaction. Both electronic and structural promoters are being used. However, very few information is available in literature about the effect of the promotion on the intrinsic activity of the active sites in iron catalysts.

Steady-state isotopic-transient kinetic analysis (SSITKA) is a powerful technique for the kinetic investigation of heterogeneous catalytic reactions at molecular level. It also provides valuable information about the catalyst surface species and it can be of great help in the identification of possible reaction mechanisms. Deactivation has been a major limitation for obtaining higher and enduring hydrocarbon productivity on supported cobalt catalysts. Catalyst deactivation leads to the decrease in the catalyst productivity, loss of active phase, recurrent halts of the reactor operation and replacement of relatively expensive cobalt catalysts. SSITKA can be particularly useful to identify the origin of the loss of activity and selectivity, because it yields independent information about the number of active sites and also allows measuring their intrinsic activity.

The goal of the thesis is to evaluate the intrinsic activity and localization of active sites in cobalt and iron catalysts using a combination of transient kinetic methods such as SSITKA, extended physico-chemical characterization and catalytic tests under quasi steady state conditions. The SSITKA experiments were performed to elucidate the role of promoters for iron and cobalt catalysts as well the effect of the zeolites structure on catalytic performance and surface kinetic parameters. A new procedure of catalyst preparation was developed to obtain a cobalt/zeolite composite catalyst. Moreover, the present thesis combines SSITKA with catalyst characterization to elucidate deactivation mechanisms and to understand the kinetic effect of a regeneration procedure. Additionally, the thesis exposes the SSITKA modeling to identify and to discriminate methanation reaction mechanisms.

_____

References

1.   Dalai, A. K.; Davis, B. H., *Applied Catalysis A: General* **2008,** *348* (1), 1-15.
2.   Schulz, H., *Applied Catalysis A: General* **1999,** *186* (1), 3-12.
3.   Zhang, Q.; Deng, W.; Wang, Y., *Journal of Energy Chemistry* **2013,** *22* (1), 27-38.
4.   Ha, v. D., The Fischer-Tropsch synthesis: a mechanistic study using transient isotopic tracing. **2001**.
5.   Botes, F. G.; Niemantsverdriet, J. W.; van de Loosdrecht, J., *Catalysis Today* **2013,** *215* (0), 112-120.
6.   Peña Zapata, D., Identification of deactivation mechanisms of cobalt Fischer-Tropsch catalysts in slurry reactor. **2013**.
7.   Tan, K. F.; Xu, J.; Chang, J.; Borgna, A.; Saeys, M., *Journal of Catalysis* **2010,** *274* (2), 121-129.
8.   Henrici-Olivé, G.; Olive, S., *Angewandte Chemie International Edition* **1976,** *15* (3), 136-141.
9.   Khodakov, A. Y.; Peregryn, B.; Lermontov, A. S.; Girardon, J. S.; Pietrzyk, S., *Catalysis Today* **2005,** *106* (1), 132-136.
10.   Khodakov, A. Y.; Chu, W.; Fongarland, P., *Chemical Reviews* **2007,** *107* (5), 1692-1744.
11.   Dai, X. P.; Liu, P. Z.; Shi, Y.; Xu, J.; Wei, W. S., *Chemical Engineering Science* **2014,** *105* (0), 1-11.
12.   de la Osa, A. R.; De Lucas, A.; Romero, A.; Valverde, J. L.; Sánchez, P., *Fuel* **2011,** *90* (5), 1935-1945.
13.   Fedou, S.; Caprani, E.; Douziech, D.; Boucher, S., *Petroleum technology quarterly* **2008,** *13* (3), 87-91.
14.   Van Berge, P. J.; Everson, R. C., *Studies in Surface Science and Catalysis* **1997,** *107*, 207-212.
15.   Ordomsky, V. V.; Carvalho, A.; Legras, B.; Paul, S.; Virginie, M.; Sushkevich, V. L.; Khodakov, A. Y., *Catalysis Today* **2016**.
16.   Espinoza, R. L.; Steynberg, A. P.; Jager, B.; Vosloo, A. C., *Applied Catalysis A: General* **1999,** *186* (1–2), 13-26.
17.   De la Osa, A. R.; De Lucas, A.; Romero, A.; Valverde, J. L.; Sánchez, P., *Catalysis today* **2011,** *176* (1), 298-302.
18.   Vosoughi, V.; Badoga, S.; Dalai, A. K.; Abatzoglou, N., *Fuel Processing Technology* **2017,** *162*, 55-65.
19.   Ducreux, O.; Rebours, B.; Lynch, J.; Roy-Auberger, M.; Bazin, D., *Oil & Gas Science and Technology-Revue de l'IFP* **2009,** *64* (1), 49-62.
20.   Kitakami, O.; Sato, H.; Shimada, Y.; Sato, F.; Tanaka, M., *Physical review B* **1997,** *56* (21), 13849.
21.   Karaca, H.; Safonova, O. V.; Chambrey, S.; Fongarland, P.; Roussel, P.; Griboval-Constant, A.; Lacroix, M.; Khodakov, A. Y., *Journal of Catalysis* **2011,** *277* (1), 14-26.
22.   Enache, D. I.; Rebours, B.; Roy-Auberger, M.; Revel, R., *Journal of Catalysis* **2002,** *205* (2), 346-353.
23.   Elbashir, N. O.; Dutta, P.; Manivannan, A.; Seehra, M. S.; Roberts, C. B., *Applied Catalysis A: General* **2005,** *285* (1), 169-180.
24.   Beaumont, S. K., *Physical Chemistry Chemical Physics* **2014,** *16* (11), 5034-5043.
25.   Yang, J.; Ma, W.; Chen, D.; Holmen, A.; Davis, B. H., *Applied Catalysis A: General* **2014,** *470* (0), 250-260.
26.   Sudsakorn, K.; Goodwin Jr, J. G.; Adeyiga, A. A., *Journal of Catalysis* **2003,** *213* (2), 204-210.

_____

27.   Luque, R.; de la Osa, A. R.; Campelo, J. M.; Romero, A. A.; Valverde, J. L.; Sanchez, P., *Energy & Environmental Science* **2012,** *5* (1), 5186-5202.
28.   Galvis, H. M. T.; Koeken, A. C. J.; Bitter, J. H.; Davidian, T.; Ruitenbeek, M.; Dugulan, A. I.; de Jong, K. P., *Catalysis today* **2013,** *215*, 95-102.
29.   Dry, M. E., *Catalysis today* **1990,** *6* (3), 183-206.
30.   Dry, M. E.; Oosthuizen, G. J., *Journal of Catalysis* **1968,** *11* (1), 18-24.
31.   Tau, L.-M.; Dabbagh, H. A.; Wilson, T. P.; Davis, B. H., *Applied catalysis* **1989,** *56* (1), 95-106.
32.   Lee, D. W.; Yoo, B. R., *Journal of Industrial and Engineering Chemistry* **2014,** *20* (6), 3947-3959.
33.   Gao, J.; Mo, X.; Goodwin, J. G., *Journal of Catalysis* **2010,** *275* (2), 211-217.
34.   Underwood, R. P.; Bell, A. T., *Applied catalysis* **1987,** *34*, 289-310.
35.   Ichikawa, M., *Journal of the Chemical Society, Chemical Communications* **1978,** (13), 566-567.
36.   Dry, M. E., *Catalysis today* **2002,** *71* (3), 227-241.
37.   Legras, B.; Ordomsky, V. V.; Dujardin, C.; Virginie, M.; Khodakov, A. Y., *ACS Catalysis* **2014,** *4* (8), 2785-2791.
38.   Díaz, J. A.; Akhavan, H.; Romero, A.; Garcia-Minguillan, A. M.; Romero, R.; Giroir-Fendler, A.; Valverde, J. L., *Fuel Processing Technology* **2014,** *128* (0), 417-424.
39.   Pour, A. N.; Shahri, S. M. K.; Zamani, Y.; Zamanian, A., *Journal of Natural Gas Chemistry* **2010,** *19* (2), 193-197.
40.   Weitkamp, J., *Solid State Ionics* **2000,** *131* (1), 175-188.
41.   Li, K.; Valla, J.; Garcia-Martinez, J., *ChemCatChem* **2014,** *6* (1), 46-66.
42.   Xing, C.; Yang, G.; Lu, P.; Shen, W.; Gai, X.; Tan, L.; Mao, J.; Wang, T.; Yang, R.; Tsubaki, N., *Microporous and Mesoporous Materials* **2016,** *233*, 62-69.
43.   Baranak, M.; Gürünlü, B.; Sarıoğlan, A.; Ataç, Ö.; Atakül, H., *Catalysis Today* **2013,** *207* (0), 57-64.
44.   Van Der Laan, G. P.; Beenackers, A., *Catalysis Reviews* **1999,** *41* (3-4), 255-318.
45.   Wang, Y.-N.; Ma, W.-P.; Lu, Y.-J.; Yang, J.; Xu, Y.-Y.; Xiang, H.-W.; Li, Y.-W.; Zhao, Y.-L.; Zhang, B.-J., *Fuel* **2003,** *82* (2), 195-213.
46.   Dry, M. E., *Journal of Molecular Catalysis* **1982,** *17* (2-3), 133-144.
47.   Dalil, M.; Sohrabi, M.; Royaee, S. J., *Journal of Industrial and Engineering Chemistry* **2012,** *18* (2), 690-696.
48.   Visconti, C. G.; Lietti, L.; Tronconi, E.; Forzatti, P.; Zennaro, R.; Rossini, S., *Catalysis Today* **2010,** *154* (3), 202-209.
49.   Satterfield, C. N., **1991**.
50.   Guisnet, M., *Catalysis today* **2013,** *218*, 123-134.
51.   Guisnet, M., *Imperial college press*: **2011**; Vol. Volume 9, pp 195-216.
52.   Subramanian, V.; Zholobenko, V. L.; Cheng, K.; Lancelot, C.; Heyte, S.; Thuriot, J.; Paul, S.; Ordomsky, V. V.; Khodakov, A. Y., *ChemCatChem* **2016,** *8* (2), 380-389.
53.   Xu, L. In *Don't rule out iron catalysts for Fischer-Tropsch synthesis*, 1998; p 179.
54.   Botes, F. G.; Böhringer, W., *Applied Catalysis A: General* **2004,** *267* (1), 217-225.
55.   Bessell, S., *Applied Catalysis A: General* **1995,** *126* (2), 235-244.
56.   Zhao, T.-S.; Chang, J.; Yoneyama, Y.; Tsubaki, N., *Industrial & engineering chemistry research* **2005,** *44* (4), 769-775.
57.   Yang, G.; Xing, C.; Hirohama, W.; Jin, Y.; Zeng, C.; Suehiro, Y.; Wang, T.; Yoneyama, Y.; Tsubaki, N., *Catalysis today* **2013,** *215*, 29-35.
58.   Liu, Z.-W.; Li, X.; Asami, K.; Fujimoto, K., *Catalysis Communications* **2005,** *6* (8), 503-506.
59.   Tsubaki, N.; Yoneyama, Y.; Michiki, K.; Fujimoto, K., *Catalysis Communications* **2003,** *4* (3), 108-111.

_____

60.   Sartipi, S.; Alberts, M.; Meijerink, M. J.; Keller, T. C.; Pérez-Ramírez, J.; Gascon, J.; Kapteijn, F., *ChemSusChem* **2013,** *6* (9), 1646-1650.

61.   Kang, X.; Zhenghong, B.; Xingzhen, Q.; Xinxing, W.; Zhong, L.; Kegong, F.; Minggui, L. I. N.; Yuhan, S. U. N., *Chinese journal of catalysis* **2013,** *34* (1), 116-129.

62.   Bae, J. W.; Park, S.-J.; Kang, S.-H.; Lee, Y.-J.; Jun, K.-W.; Rhee, Y.-W., *Journal of Industrial and Engineering Chemistry* **2009,** *15* (6), 798-802.

63.   Iglesia, E.; Reyes, S. C.; Madon, R. J.; Soled, S. L., *Advances in catalysis* **1993,** *39*, 221-302.

64.   Todic, B.; Ma, W.; Jacobs, G.; Davis, B. H.; Bukur, D. B., *Journal of Catalysis* **2014,** *311*, 325-338.

65.   Yang, J.; Qi, Y.; Zhu, J.; Zhu, Y.-A.; Chen, D.; Holmen, A., *Journal of Catalysis* **2013,** *308* (0), 37-49.

66.   Storsæter, S.; Chen, D.; Holmen, A., *Surface Science* **2006,** *600* (10), 2051-2063.

67.   Cheng, J.; Hu, P.; Ellis, P.; French, S.; Kelly, G.; Lok, C. M., *Journal of Catalysis* **2008,** *257* (1), 221-228.

68.   Ahón, V. R.; Costa Jr, E. F.; Monteagudo, J. E. P.; Fontes, C. E.; Biscaia Jr, E. C.; Lage, P. L. C., *Chemical Engineering Science* **2005,** *60* (3), 677-694.

69.   Mosayebi, A.; Haghtalab, A., *Chemical Engineering Journal* **2015,** *259* (0), 191-204.

70.   Valero, M. C.; Raybaud, P., *Catalysis letters* **2013,** *143* (1), 1-17.

71.   Davis, B. H., *Fuel Processing Technology* **2001,** *71* (1), 157-166.

72.   van Dijk, H. A. J.; Hoebink, J. H. B. J.; Schouten, J. C., *Chemical Engineering Science* **2001,** *56* (4), 1211-1219.

73.   Sage, V.; Burke, N., *Catalysis Today* **2011,** *178* (1), 137-141.

74.   Bhatelia, T.; Li, C. e.; Sun, Y.; Hazewinkel, P.; Burke, N.; Sage, V., *Fuel Processing Technology* **2014,** *125*, 277-289.

75.   Tsakoumis, N. E.; Rønning, M.; Borg, Ø.; Rytter, E.; Holmen, A., *Catalysis Today* **2010,** *154* (3–4), 162-182.

76.   Argyle, M. D.; Bartholomew, C. H., *Catalysts* **2015,** *5* (1), 145-269.

77.   Hegedus, L. L.; McCabe, R. W., *Studies in Surface Science and Catalysis* **1980,** *6*, 471-505.

78.   Moulijn, J. A.; Van Diepen, A. E.; Kapteijn, F., *Applied Catalysis A: General* **2001,** *212* (1), 3-16.

79.   Bartholomew, C. H., *Applied Catalysis A: General* **2001,** *212* (1), 17-60.

80.   Sadeqzadeh, M.; Chambrey, S.; Piché, S.; Fongarland, P.; Luck, F.; Curulla-Ferré, D.; Schweich, D.; Bousquet, J.; Khodakov, A. Y., *Catalysis Today* **2013,** *215* (0), 52-59.

81.   Pena, D.; Griboval-Constant, A.; Lecocq, V.; Diehl, F.; Khodakov, A. Y., *Catalysis today* **2013,** *215*, 43-51.

82.   Menon, P. G., *Journal of Molecular Catalysis* **1990,** *59* (2), 207-220.

83.   van de Loosdrecht, J.; Balzhinimaev, B.; Dalmon, J. A.; Niemantsverdriet, J. W.; Tsybulya, S. V.; Saib, A. M.; van Berge, P. J.; Visagie, J. L., *Catalysis Today* **2007,** *123* (1–4), 293-302.

84.   van de Loosdrecht, J.; Ciobîcă, I. M.; Gibson, P.; Govender, N. S.; Moodley, D. J.; Saib, A. M.; Weststrate, K.-J.; Niemantsverdriet, J. W., *ACS Catalysis* **2016**.

85.   Overett, M. J.; Breedt, B.; Du Plessis, E.; Erasmus, W.; Van De Loosdrecht, J., *Prepr. Pap. Am. Chem. Soc., Div. Pet. Chem* **2008,** *53*, 126.

86.   Kistamurthy, D.; Saib, A. M.; Moodley, D. J.; Niemantsverdriet, J. W.; Weststrate, C. J., *Journal of Catalysis* **2015,** *328*, 123-129.

87.   Moodley, D. J.; van de Loosdrecht, J.; Saib, A. M.; Overett, M. J.; Datye, A. K.; Niemantsverdriet, J. W., *Applied Catalysis A: General* **2009,** *354* (1–2), 102-110.

88.   Lee, D.-K.; Lee, J.-H.; Ihm, S.-K., *Applied Catalysis* **1988,** *36*, 199-207.

89.   Gruver, V.; Young, R.; Engman, J.; Robota, H. J., *Preprints-American Chemical Society. Division of Petroleum Chemistry* **2005,** *50* (2), 164-166.

90.   Pankina, G. V.; Chernavskii, P. A.; Lermontov, A. S.; Lunin, V. V., *Petroleum Chemistry* **2002,** *42* (4), 217-220.

_____

91.   Peña, D.; Griboval-Constant, A.; Diehl, F.; Lecocq, V.; Khodakov, A. Y., *ChemCatChem* **2013,** *5* (3), 728-731.

92.   Duncan, T. M.; Winslow, P.; Bell, A. T., *Journal of Catalysis* **1985,** *93* (1), 1-22.

93.   Pinard, L.; Bichon, P.; Popov, A.; Lemberton, J. L.; Canaff, C.; Mauge, F.; Bazin, P.; Aguiar, E. F. S.; Magnoux, P., *Applied Catalysis A: General* **2011,** *406* (1), 73-80.

94.   Stenger Jr, H. G.; Satterfield, C. N., *Industrial & Engineering Chemistry Process Design and Development* **1985,** *24* (2), 415-420.

95.   Bartholomew, C. H.; Bowman, R. M., *Applied Catalysis* **1985,** *15* (1), 59-67.

96.   Visconti, C. G.; Lietti, L.; Forzatti, P.; Zennaro, R., *Applied Catalysis A: General* **2007,** *330*, 49-56.

97.   Li, J.; Coville, N. J., *Applied Catalysis A: General* **2001,** *208* (1), 177-184.

98.   Rytter, E.; Holmen, A., *Catalysts* **2015,** *5* (2), 478-499.

99.   Karaca, H.; Hong, J.; Fongarland, P.; Roussel, P.; Griboval-Constant, A.; Lacroix, M.; Hortmann, K.; Safonova, O. V.; Khodakov, A. Y., *Chemical Communications* **2010,** *46* (5), 788-790.

100.   Saib, A. M.; Gauché, J. L.; Weststrate, C. J.; Gibson, P.; Boshoff, J. H.; Moodley, D. J., *Industrial & Engineering Chemistry Research* **2013,** *53* (5), 1816-1824.

101.   Lancelot, C.; Ordomsky, V. V.; Stéphan, O.; Sadeqzadeh, M.; Karaca, H. l.; Lacroix, M.; Curulla-Ferré, D.; Luck, F.; Fongarland, P.; Griboval-Constant, A., *ACS Catalysis* **2014,** *4* (12), 4510-4515.

102.   Happel, J., *Chem. Eng. Sci.* **1978,** *33*, 1567.

103.   Iglesia, E.; Soled, S. L.; Fiato, R. A., Cobalt-ruthenium catalysts for Fischer-Tropsch synthesis. Google Patents: 1989.

104.   Morales, F.; Weckhuysen, B. M., *Catalysis* **2006,** *19* (1).

105.   Agrawal, P. K.; Katzer, J. R.; Manogue, W. H., *Journal of Catalysis* **1981,** *69* (2), 312-326.

106.   Shannon, S. L.; Goodwin, J. G., *Chemical Reviews* **1995,** *95* (3), 677-695.

107.   Ledesma, C.; Yang, J.; Chen, D.; Holmen, A., *ACS Catalysis* **2014,** *4* (12), 4527-4547.

108.   Tsai, Y.-T.; Goodwin Jr, J. G., *Journal of Catalysis* **2011,** *281* (1), 128-136.

109.   Rohr, F.; Lindvåg, O. A.; Holmen, A.; Blekkan, E. A., *Catalysis Today* **2000,** *58* (4), 247-254.

110.   Enger, B. C.; Frøseth, V.; Yang, J.; Rytter, E.; Holmen, A., *Journal of Catalysis* **2013,** *297* (0), 187-192.

111.   Kang, H. C.; Weinberg, W. H., *Chemical reviews* **1995,** *95* (3), 667-676.

112.   Mirodatos, C., *Catalysis Today* **1991,** *9* (1-2), 83-95.

113.   Kao, J.-Y.; Piet-Lahanier, H.; Walter, E.; Happel, J., *Journal of Catalysis* **1992,** *133* (2), 383-396.

114.   Yang, J.; Chen, D.; Holmen, A., *Catalysis Today* **2012,** *186* (1), 99-108.

115.   Schanke, D.; Vada, S.; Blekkan, E. A.; Hilmen, A. M.; Hoff, A.; Holmen, A., *Journal of Catalysis* **1995,** *156* (1), 85-95.

116.   Patanou, E.; Lillebø, A. H.; Yang, J.; Chen, D.; Holmen, A.; Blekkan, E. A., *Industrial & Engineering Chemistry Research* **2013,** *53* (5), 1787-1793.

117.   Lillebø, A. H.; Patanou, E.; Yang, J.; Blekkan, E. A.; Holmen, A., *Catalysis today* **2013,** *215*, 60-66.

118.   Haddad, G. J.; Chen, B.; Goodwin Jr, J. G., *Journal of Catalysis* **1996,** *161* (1), 274-281.

119.   Vada, S.; Kazi, A. M.; Bedu-Addo, F. K.; Chen, B.; Goodwin, J. G., *Studies in Surface Science and Catalysis* **1994,** *81*, 443-448.

120.   Bertole, C. J.; Mims, C. A.; Kiss, G., *Journal of Catalysis* **2004,** *221* (1), 191-203.

121.   Iglesia, E., *Applied Catalysis A: General* **1997,** *161* (1), 59-78.

122.   Oukaci, R.; Singleton, A. H.; Goodwin, J. G., *Applied Catalysis A: General* **1999,** *186* (1), 129-144.

123.   Rane, S.; Borg, Ø.; Yang, J.; Rytter, E.; Holmen, A., *Applied Catalysis A: General* **2010,** *388* (1–2), 160-167.

_____

124.   Phan, X. K.; Yang, J.; Bakhtiary-Davijnay, H.; Myrstad, R.; Venvik, H. J.; Holmen, A., *Catalysis letters* **2011,** *141* (12), 1739-1745.
125.   Jongsomjit, B.; Panpranot, J.; Goodwin, J. G., *J. Catal.* **2003,** *215*, 66.
126.   den Breejen, J. P.; Radstake, P. B.; Bezemer, G. L.; Bitter, J. H.; Frøseth, V.; Holmen, A.; Jong, K. P. d., *Journal of the American Chemical Society* **2009,** *131* (20), 7197-7203.
127.   Yang, J.; Tveten, E. Z.; Chen, D.; Holmen, A., *Langmuir* **2010,** *26* (21), 16558-16567.
128.   Borg, Ø.; Dietzel, P. D. C.; Spjelkavik, A. I.; Tveten, E. Z.; Walmsley, J. C.; Diplas, S.; Eri, S.; Holmen, A.; Rytter, E., *Journal of Catalysis* **2008,** *259* (2), 161-164.
129.   Frøseth, V.; Holmen, A., *Topics in Catalysis* **2007,** *45* (1), 45.
130.   Panpranot, J.; Goodwin, J. G.; Sayari, A., *Journal of Catalysis* **2002,** *211* (2), 530-539.
131.   Govender, N. S.; Botes, F. G.; de Croon, M. H. J. M.; Schouten, J. C., *Journal of Catalysis* **2008,** *260* (2), 254-261.
132.   Qi, Y.; Yang, J.; Duan, X.; Zhu, Y.-A.; Chen, D.; Holmen, A., *Catalysis Science & Technology* **2014,** *4* (10), 3534-3543.
133.   Happel, J.; Walter, E.; Lecourtier, Y., *Industrial & Engineering Chemistry Fundamentals* **1986,** *25* (4), 704-712.
134.   Otarod, M.; Happel, J.; Soong, Y.; Walter, E.; Pronzato, L., *Appl. Catal., A* **1997,** *151*, 97.

Chapter 2. Catalysts, Experimental Methods and Modeling

2.1 Catalyst preparation

2.1.1 Cobalt based catalysts

Cobalt catalysts supported on silica with and without platinum as promoter (15% and 20% Co; 0.1% Pt in wt.) were prepared by incipient wetness impregnation of commercial amorphous silica (CARIACT Q-10, Fuji Silysia) with aqueous solutions of cobalt nitrate ($Co(NO_3)_2 \cdot 6H_2O$) and tetramine platinum nitrate ($Pt(NH_3)_4(NO_3)_2$). The catalysts were dried for 1 h at 100 °C and calcined at 450 ℃ in air flow of 10 mL/min for 7 h.

The cobalt catalysts supported on zeolites (ZSM-5, BEA, MOR) have been synthesized by incipient wetness impregnation of relevant zeolites with Co nitrate in the mixture with tetramine platinum nitrate. The ZSM-5, MOR and BEA zeolites with the Si/Al ratio of 13, 8 and 9 have been provided by Zeolyst. The content of Co and Pt has been respectively 20 and 0.1 wt. The catalysts were dried for 1 h at 100 °C and calcined at 450 ℃ in air flow of 10 mL/min for 7 h.

The alumina supported catalyst containing 25 wt.% cobalt was prepared using the two-step impregnation. In case of Pt-promoted samples, an additional incipient wetness impregnation of Co/Al_2O_3 with aqueous solutions of hydrogen hexachloroplatinate (H_2PtCl_6), (Sigma–Aldrich) was carried out. The platinum content was 0.1 wt.% in the

final catalysts. After impregnation and drying, the cobalt catalysts were calcined in airflow at 400 °C for 6 h with a 1 °C/min temperature ramping.

2.1.2 Cobalt extraction from the outer surface of zeolites with a heteropoly acid

Cobalt catalysts supported on zeolites ZSM-5, BEA, MOR synthesized by incipient wetness impregnation as described in the above section were treated with a Keggin-type tungstophosphoric acid $H_3PW_{12}O_{40}$ (HPW). The large acid molecules of HPW (diameter = 1.2 nm) are not able to enter the pores of the zeolites. The HPW treatment was performed to selectively remove cobalt from the zeolite outer surface and non-incorporated in the pores of the zeolite. The following experimental procedure was applied:

1) 0.25 g of the catalysts was mixed mechanically to 10 g of HPW ($H_3W_{12}O_{40}$) and to small amount of water (5 mL) to obtain slurry;
2) The catalysts were heated up to 90 ℃ with a ramp rate of 2 ℃/min;
3) The catalysts were washed by distilled water while its separation by filtration.

These three steps were repeated 5 times with subsequent calcination of the catalysts at 450 ℃ in air during 7 h.

2.1.3 Iron based catalysts

Commercial amorphous silica (CARIACT Q-10, Fuji Silysia) was used as a catalytic support. The Fe/SiO_2, $FeBi/SiO_2$ and $FePb/SiO_2$ catalysts were prepared by incipient wetness impregnation of support with aqueous solutions of hydrous iron nitrate ($Fe(NO_3)_3 \cdot 9H_2O$), bismuth nitrate ($Bi(NO_3)_3 \cdot 5H_2O$) or lead nitrate ($Pb(NO_3)_2$).

The concentrations of the impregnating solutions were calculated to obtain 10 wt. % iron in the final catalysts with the molar ratio of Fe to promoter 100 to 2. After the impregnation, the catalysts were dried overnight in an oven at 100 °C. Then, the samples were calcined in air at 400 °C for 6 h with 1 °C/min temperature ramping.

_____

2.2 Catalyst characterization

2.2.1 Transmission Electron Microscopy (TEM)

The Transmission Electron Microscopy (TEM) is an efficient tool to study a catalyst structure with spatial resolution. The technique presents the same basic principles as the light microscope, however, the source is an electron beam. TEM analysis enables to get a good spatial resolution due to the use of electrons with a low wavelength (less than 1Å). Therefore, the sample is submitted to an electron beam of high energy (200 keV). By the interaction with the specimen, both backscattered and secondary electrons are reflected giving information about the sample morphology [1]. The difference from the scanning electron microscopy (SEM) is that the TEM technique makes use of transmitted electrons to take information about the internal structure of the sample and to generate the images.

In the present thesis, TEM observations were performed on a Tecnai instrument, equipped with a LaB_6 crystal, operating at 200 kV. Prior to the analysis, the samples were dispersed by ultrasound in an ethanol solution for 5 min, and a drop of solution was deposited onto a carbon membrane supported on a 300 mesh-copper grid. The metal particle histograms were obtained using more than 150 detected cobalt particles from the TEM images. Software Gatan Digital Microgap was utilized to treat the TEM images.

2.2.2 Temperature Programmed Hydrogenation (TPH) combined with Mass Spectrometry (TPH-MS)

Temperature-programmed hydrogenation (TPH) consists of monitoring of specific chemical reactions involving a carrier gas while temperature is rising with a linear rate. Temperature Programmed Hydrogenation with the analysis of desorbing products by Mass Spectrometry (TPH-MS) was carried using an AutoChem II 2920 V3 0.2 Micromeritics apparatus with 80 mg of samples exposed to FTS after different times on stream. The heating rate was of 5 °C/min from room temperature to 1000 °C under flow of 3 vol. % H_2/Ar. The hydrogenation of carbon species: $C_{ads} + 2H_2 \rightarrow CH_4$ (m/e = 15, instead of 16

to avoid interference from ionized oxygen coming from water vapor) was monitored using a Balzers Omnistar mass spectrometer. The m/z = 28 fragment was used to identify the presence of desorbing C_xH_y hydrocarbons.

2.2.3 X-ray diffraction (XRD)

The ex situ X-ray diffraction (XRD) patterns of the calcined catalyst were recorded by a Bruker AXS D8 Advance diffractometer. The data were recorded in the 2θ range from 10 to 90° with a 0.02 ° step size and a 2 s step time from a source of Cu (Kα) radiation (λ = 1.54 nm).

The crystallite phases were determined by comparing the experimental diffraction patterns with those from the standard powder XRD files (JCPDS) published by the International Center for Diffraction Data. The average crystallite size of cobalt oxide was calculated according to Scherrer's equation [2] at the maximum of the width at half height (FWMH) for the more intense peaks. Software EVA was used to the data treatment. The following equation was applied to obtain the cobalt metallic crystallite size from the size of cobalt oxide crystallites.

$$dCo^0(nm) = 0.75 * dCo_3O_4 \qquad (1)$$

The dispersion was calculated from average metal particles sizes, assuming spherical, uniform particles with the site density of 14.6 atoms/nm², by use of the following formula:

$$D(\%) = \frac{96}{dCo^0} \qquad (2)$$

2.2.4 Inductively coupled plasma - optical emission spectrometry (ICP-OES)

The ICP-OES is an analytical technique used for quantitative, semi-quantitative or qualitative determination of elements constituting the catalysts. The ICP-EOS determines elements at trace level. The catalyst is dissolved using acid or base digestion procedures.

_____

In the present thesis, the samples of cobalt supported on zeolites were digested in the aqua regia (mixture of hydrochloric acid and nitric acid).

The applied ICP-OES – Agilent equipment in the Plateform Realcat includes a source of emission (argon) surrounded by a copper coil connected to a radio frequency (RF) generator, a concentric nebulizer, optics (diffracting grating and polychromator), a coupled charged detector (CCD) and an autosampler with 3 racks of 60 positions each and an automatic arm to collect samples.

2.2.5 Determination of surface area by the Brunauer–Emmett–Teller method (BET)

BET analysis provides specific surface by nitrogen multilayer adsorption measured as a function of relative pressure of the adsorbed nitrogen. The technique encompasses external area and pore area evaluations to determine the total specific surface. The shape of the isotherm hysteresis provides information about the porosity of the material.

The BET surface area, pore volume and average pore diameter were determined by N_2 low temperature adsorption using a Micromeritics ASAP 2000 automated system. The samples were degassed under vacuum at <10 μm Hg in the Micromeritics ASAP 2000 at 300 °C for 4 h prior to N_2 physisorption. The total pore volume (TPV) was calculated from the amount of vapor adsorbed at a relative pressure close to unity assuming that the pores are filled with the condensate in liquid state. The catalyst external surface area and micropore volume were calculated using the de Boer t-plot method.

2.3 SSITKA set up

The schema of the experimental SSITKA is shown in Figure 2.1. On the feed section, the SSITKA system presents two independent feed lines. The first line is dedicated to unlabeled compounds and tracer (CO, H_2, He and Ne), the second one to the isotopic compound (^{13}CO), H_2 and He. The Brooks mass flow controllers (MFC) for each component were used. The total flow rate of these two feed streams was identical during the switch. Ne was used in a small rate (0.5 mL/min) as the tracer to measure the gas-phase

hold up for the reaction system. Pressure transducers are used to adjust the same pressure drop for both lines.
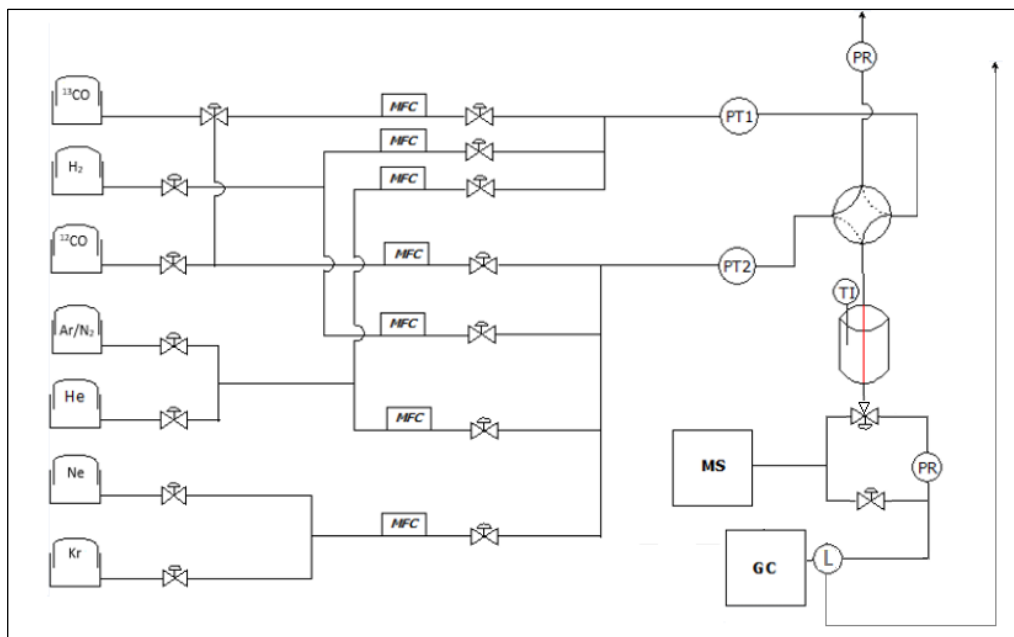
Figure 2.1 Schematic representation of the SSITKA set-up. (MFC = flow controller; PT = pressure transducer; PR = Manual pressure regulator; TI = temperature indicator; MS = mass spectrometer; GC = gas chromatograph; L = GC loop).

The reaction section is composed of the following items:

- o Two-position Valco four-way;
- o Fixed bed reaction fixed bed reactor ($di_n = 2$ mm);
- o Pressure transducers;
- o Manual pressure regulator of the vent line (can be changed for the automatic pressure regulator);
- o Device to switch the Valco valve (actuator);
- o Temperature controller.

Carbon monoxide hydrogenation was performed in a fixed bed reactor (diameter of 2 mm) at atmospheric pressure. The reactor was heated by an electric resistance. The axial catalyst bed temperature was monitored with a movable thermocouple located in the center

of the reactor. For all experiments, before loading into the reactor, the catalyst was pressed into wafers, crushed and sieved to obtain the particle size range of 50 μm −150 μm.

The carbon monoxide conversion and reaction selectivities were determined by analyzing the reaction effluents with a Shimadzu 2014 gas-chromatograph equipped with a CP-PoraPLOT and a CTR-1 column, as well as flame ionization detector (FID) and thermal conductivity detector (TCD). Nitrogen was used as an internal standard for calculating carbon monoxide conversion (see further details in the next section).

The isotopic switches were realized using a two-position four-way Valco valve and monitored with a QMG 432 Omnistar mass spectrometer. The gaseous sample was transferred from the outlet of the reactor to the mass-spectrometer via a silica capillary. To prevent condensation of water and hydrocarbons, the capillary was heated to 150 °C.

2.4 Calculation of conversion and selectivities

The CO conversion was based on the molar flow of carbon monoxide entering ($F_{CO\ in}$) and leaving the reactor ($F_{CO\ out}$) as demonstrated on Equation 3.

$$X_{CO} = \frac{F_{CO\ in} - F_{CO\ out}}{F_{CO\ in}} * 100 \qquad (3)$$

TCD determines the CO, CO_2, N_2 and CH_4 concentrations on the gas flow. Then, the outlet flow of each species was obtained on the basis of the response factor acquired by the GC calibration. Therefore, the methane and carbon dioxide selectivities were calculated by Equation 4 and Equation 5, respectively.

$$S_{CH_4} = \frac{F_{CH_4\ out}}{F_{CO\ in} - F_{CO\ out}} * 100 \qquad (4)$$

$$S_{CO_2} = \frac{F_{CO_2\ out}}{F_{CO\ in} - F_{CO\ out}} * 100 \qquad (5)$$

Using FID, the carbon counting device, the molar flow of each hydrocarbon from C_2 to C_4 was calculated on carbon basis. Equation 6 was applied to determine the selectivity to each saturated and unsaturated hydrocarbon.

$$S_{C_i} = \frac{F_{C_i\ out}}{F_{CO\ in} - F_{CO\ out}} * 100 \qquad (i = C_2 - C_4) \tag{6}$$

2.5 Experimental procedure

2.5.1 Transient isotopic study of iron based catalysts

The following experimental procedure was used for the iron catalyst: 100 mg of FeBi/SiO$_2$ were mixed with the same amount of SiC as inert. The reduction was done using a heating ramp of 3 °C/min to reach 350 °C. The catalyst was submitted to the CO flow of 2 mL/min during 12 h. Then, the sample was cooled down to 25 °C using the same temperature ramp. At ambient temperature, the switches of ^{12}CO to ^{13}CO were applied. These measurements were only used to evaluate the CO adsorption on iron catalysts. Note that no chemical reaction occurs at room temperature.

To study the kinetic parameters under reaction conditions Fe/SiO$_2$ and FeBi/SiO$_2$ were activated using CO flow of 2 mL/min during 12 h with a heating ramp of 3 °C/min.

Afterwards, the catalyst was cooled down with the same temperature ramp and submitted to the following reaction conditions: temperature of 350 °C, ambient pressure, GHSV equal to 8 400 mL/g h and ratio H$_2$/CO of 2. After 17 h on stream, the SSITKA ^{12}CO to ^{13}CO switches were performed.

The WGS activity evaluation for iron promoted and non-promoted catalysts was carried out by the following procedure:

1) Activation by carbidization in CO to obtain the iron carbide phase. The conditions were the following: temperature 350 °C, heating rate 3 °C/min, CO flow of 2 mL/min during 12 h.

_____

2) After 12 h, cooling down to 300 °C. Use of 2 mL/min of N_2 to purge. Heating ramp of 3 °C/min.

3) At 300°C with 2 mL/min of N_2, start H_2O addition with the rate of 0.3 mL/min during 10 min. The signals of H_2 and CH_4 were observed by mass spectrometer (MS).

        <u>Reaction at this step</u>:

        $Fe + H_2O \rightarrow FeO + H_2$

        $M + H_2O \rightarrow MeO + H_2$
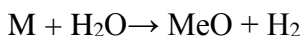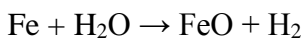
4) Stop the water exposure after 10 min and purge with N_2 (2 mL/min). Wait the MS signal stabilization of H_2 and CH_4.

5) CO exposure in the following conditions: temperature of 300 °C and CO flow of 5 mL/min. The CO_2 production was observed by mass spectrometer (MS).

        <u>Reactions at this step:</u>

        $FeO + 3CO \rightarrow FeC + 2CO_2$

        $M\text{-}O + CO \rightarrow M + CO_2$
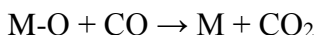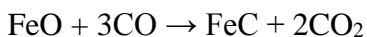
2.5.2 Effect of platinum promotion on the intrinsic activity of cobalt catalyst during CO hydrogenation

The reduction of the Co/SiO_2 and $CoPt/SiO_2$ catalysts was realized at 400°C in hydrogen flow of 8 cm^3/min for 2 h with a 5 °C/min heating rate. To study the SSITKA surface kinetic parameters under CO hydrogenation conditions (250 °C, syngas at different ratio feed of H_2/CO of 2 and 5 with 45 mg of catalyst mixed with 90 mg of SiC), the switches from $^{12}CO/H_2/He/Ne$ to $^{13}CO/H_2/He$ were executed using a four-port Valco valve.

2.5.3 Influence of the support structure over the catalytic performance and SSITKA parameters

In all experiments, 40 mg of catalyst was mixed with 80 mg of SiC. The samples were loaded into a millimetric fixed bed reactor and reduced in pure H_2 flow of 8 cm^3/min

for 2 h at 400 °C with a 5 °C/min heating rate. In the CO adsorption study, after reduction, the sample were cooled down in the same rate ramp to 100 ℃ and switches from $^{12}CO/He/Ne$ to $^{13}CO/He$ were applied to determine the total number of active sites.

To evaluate both the effect of support structure and hydrogen partial pressure, the samples were submitted to the reaction temperature equal to 250 ℃ and at different ratios of H_2/CO (2, 5 and 10), corresponding to the gas hourly space velocities (GHSV) of 13 500 mL/g h, 18 000 mL/g h and 23 850 mL/g h, respectively. Then, after 3 h of reaction, the switches from $^{12}CO/H_2/He/Ne$ to $^{13}CO/H_2/He$ were applied.

2.5.4 High throughput catalytic tests of the cobalt-zeolite composites

The catalytic performance of the synthetized cobalt-zeolite composite was evaluated using the REALCAT platform in a Flowrence high-throughput unit (Avantium®) equipped with 16 parallel milli-fixed-bed reactors (d = 2 mm) with a plug-flow hydrodynamics. The operating conditions of the carbon monoxide hydrogenation are displayed as follow:

- o Total pressure of 20 bar;
- o Temperature of 250 °C;
- o Molar ratio H_2/CO equal to 2;
- o GHSV at 1.7-5 L/g·h;
- o Catalyst loading of 50 mg per reactor.

Prior to the catalytic tests, all the samples were activated in a flow of H_2 at atmospheric pressure during 10 h at 400 °C. During the activation step, the temperature ramp was 3 °C/min. After the activation, the catalysts were cooled down to 180 °C and a flow of premixed syngas was gradually introduced to the catalysts. When the pressure attained 20 bar, the temperature was slowly increased to 250 °C.

_____

Figure 2.2 Flowrence (Avantium) unit in the RealCat high throughput platform.

The gaseous reaction products were analyzed by on-line gas chromatography. Analysis of permanent gases was performed using a Molecular Sieve column and a thermal conductivity detector. Carbon dioxide and C_1-C_4 hydrocarbons were separated in a PPQ column and analyzed by a thermoconductivity detector.

The C_5-C_{12} hydrocarbons were analyzed using a CP-Sil5 column and a flame-ionization detector. High-molecular-weight products were collected at atmospheric pressure in vials heated at 60 °C. The carbon monoxide contained 5% of helium, which was used as an internal standard for calculating carbon monoxide conversion. The reaction rates were defined as the number of moles of CO converted per hour per gram of catalyst (mol/g h). The product selectivity (S) was reported on carbon basis.

2.6 SSITKA methodology

SSITKA involves isotopic labelling, and detection of the labelled product species to measure parameters like surface residence times, surface coverage and concentrations of adsorbed reaction intermediates.

The maintenance of isobaric, same flow rates and isothermal reaction conditions during the switch guarantees the operation at the quasi steady-state conditions. Figure 2.3 shows a typical SSITKA response with normalized curves ($NR_i(t)$) for CO, CH$_4$ (both labeled – ^{13}C and non labeled – ^{12}C) with Ne as the inert.
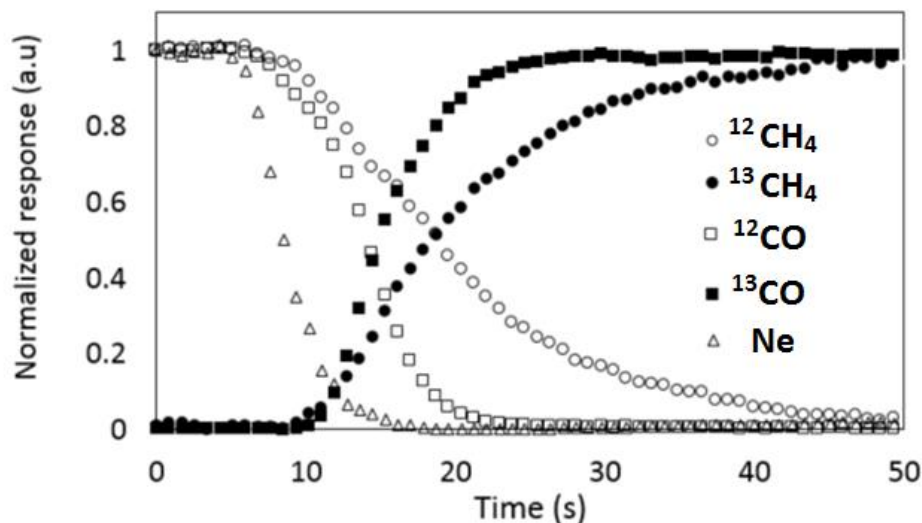
Figure 2.3 Normalized concentrations during switches from ^{12}CO/H$_2$/He/Ne to ^{13}CO/H$_2$/He on CoPt/SiO$_2$ for CO hydrogenation reaction.

Because the reactor operates under isothermal and isobaric conditions for each gas component, the catalytic surface does not suffer any chemical changes during the isotopic switch, and mechanistic studies can be carried out efficiently. The surface residence time is determined by the area under the normalized curve.

$$\tau_i = \int_0^\infty NR_i(t)dt \qquad (i = \text{Ne, CH}_4, \text{CO}) \tag{7}$$

where NR_i is the normalized response of reactants and reactive intermediates.

The difference in area computed for a particular specie (i) with the area measured for the inert tracer (Ne in this work) gives the average surface reaction residence time (τ_i). The chromatographic effect must be taken into account, because the gaseous compounds might adsorb not only on the active sites but also throughout the whole reactor system. The chromatographic effects should be kept small in order to avoid interference with the

_____

intrinsic kinetics. The required correction is showed in Eq. 8 for reactant and Eq. 9 for product:

$$\tau_{CO,corrected} = \tau_{CO,measured} - \tau_{Ne} \tag{8}$$

$$\tau_{CHx,corrected} = \tau_{CHx,measured} - 0.5 \cdot \tau_{CO,corrected} \tag{9}$$

The number of intermediates (N_i), also called the number of adsorbed species, is calculated from the mean surface residence time and molar outlet flow of species ($F_{i,out}$) and mass of catalyst (W).

$$N_i = \frac{F_{i,out}}{W} \cdot \tau_i \tag{10}$$

The surface coverage of precursors leading to methane and CO are calculated on basis of the number of adsorbed species and total number of active sites (N_S), often determined by H_2 chemisorption.

$$\theta_i = \frac{N_i}{N_S} \qquad (i = CH_4, CO) \tag{11}$$

2.7   Kinetic modeling

The application of kinetic modeling in SSITKA allows obtaining additional information about surface reaction mechanisms and rate constants, beyond the surface residence time and concentration of intermediates. This technique was applied to identify plausible surface reaction mechanisms for FT reaction in cobalt catalyst, based on the results obtained in the experiments described in the previous sections.

The SSITKA experiment was modeled as a transient isothermal/isobaric PFR using the approach described by Ledesma et al. [3] imposing a sudden switch on $^{13}CO/^{12}CO$ in the feed stream at t = 0. The model predicts the composition (in the gas phase and surface) along the axial direction of reactor as a function of time C_i (z,t) for a given set of operating conditions and kinetic parameters. The data generated in the SSITKA experiments (transient curves for the concentration of CO and CH₄ in the outlet stream and CO

conversion) can be used to estimate the kinetic parameters according to different proposed mechanisms, as discussed later in this section. The model was implemented in the software EMSO [4], which integrates modeling, simulation and parameter estimation in a single environment. The following assumptions were made in the formulation of the model:

- Reactor as a plug-flow-reactor without radial and axial dispersion;

- Absence of internal and external temperature gradients in a catalyst pellet;

- No mass transfer limitations;

- Absence of kinetic isotope effects;

- Isothermal and isobaric operation of the reactor;

- Constant total molar flow rate;

- Reversible molecular sorption of CO;

- Existence of one or two reactive intermediates towards methane formation.

The concentrations of the relevant species are then computed as functions of time and normalized axial position ($0 \leq x \leq 1$), by solving the set of equations formed by the conservation equations for gaseous ($X = CO_{(g)}$, $CH_{4(g)}$) and adsorbed species ($Y = CO_{ads}$, C_{ads}, $C_{\alpha,ads}$, $C_{\beta,ads}$), which are written as follows:

$$\frac{\partial C_X}{\partial t} + \frac{1}{\tau}\frac{\partial C_X}{\partial x} = \frac{\rho_b}{\varepsilon_b}R_{w,X} \tag{12}$$

$$\frac{\partial L_Y}{\partial t} = R_{w,Y} \tag{13}$$

where:

C_X = gas phase concentration (mol/m^{3}gas)

L_Y = surface concentration (mol/kg$_{cat}$)

R_w = reaction rate of different species (mol/kg$_{cat}$ s)

t = time (s)

ρ_b = density of catalyst bed (kg$_{cat}$/m^{3}bed)

ε_b = catalyst bed porosity (m^{3}gas/m^{3}bed) calculated from:

_____

$$\varepsilon_b = 1 - \frac{1}{V_R} \left(\frac{W_{cat}}{\rho_{cat}} (1 - \varepsilon_{cat}) + \frac{W_{SiC}}{\rho_{SiC}} \right) \tag{14}$$

τ is the surface residence time (s) calculated from:

$$\tau = \frac{\varepsilon_b \cdot V_R}{F_{V,total}} \tag{15}$$

where:

V_R = total volume of the reactor (m³)

$F_V, total$ = total flow rate (m³/s)

The R_w term is dependent on the reaction mechanism used among the six models presented in Figure 1.8 from Chapter 1. The initial conditions to run the simulation using EMSO software is the normalized concentration of CO$_{(g)}$ equal to 1 and in relation to carbon species intermediates (C$_{ads}$, C$_{\alpha,ads}$, C$_{\beta,ads}$) is equal to zero. An example of the full set of equations for one of the mechanisms (M1 from Figure 1.8) is given below; the analogous models are formulated according the other proposed mechanisms.

Gaseous phase species:

$$\frac{\partial C_{CO(g)}}{\partial t} + \frac{1}{\tau} \frac{\partial C_{CO(g)}}{\partial x} = \frac{\rho_b}{\varepsilon_b} \left(k_{des} C_{CO_{ads}} - k_{ads} C_{CO_g} \right) \tag{16}$$

$$\frac{\partial C_{CH_4}}{\partial t} + \frac{1}{\tau} \frac{\partial C_{CH_4}}{\partial x} = \frac{\rho_b}{\varepsilon_b} \left(k_4 C_{C_{ads}} \right) \tag{17}$$

Intermediate and adsorbed species:

$$\frac{\partial C_{CO_{ads}}}{\partial t} = k_{ads} C_{CO(g)} - k_{des} C_{CO_{ads}} - k_1 C_{CO_{ads}} \tag{18}$$

$$\frac{\partial C_{C_{ads}}}{\partial t} = k_1 C_{CO_{ads}} - k_4 C_{C_{ads}} \tag{19}$$

The set of PDE equations was solved numerically using the method of lines. The spatial derivatives are discretized using backward finite-differences, using a mesh with 100 points along the axial direction enough to provide mesh-independent solutions, as verified

in a preliminary convergence study. The resulting set of ordinary differential equations is solved using an implicit ODE solver with automatic control of time step as implemented in the software EMSO.

The kinetic parameters (k_{ads}, k_{des}, k_1, k_2, k_3 and k_4) for each model (M1 to M6) were estimated by minimizing the deviation between experimental data, namely the normalized transient curves of ^{12}CO and $^{12}CH_4$ and CO conversion obtained in SSITKA experiments, and corresponding model predictions according to the least-squares method as implemented in the EMSO software. The parameter estimation package implemented in the EMSO was used in this procedure; this package makes use of the model implemented and provides estimates of the selected parameters and results of a statistical analysis of the estimation.

References

1.   Niemantsverdriet, J. W., *Spectroscopy in catalysis*. John Wiley & Sons: 2007.

2.   Scherrer, P., Göttinger Nachrichten Math. *Phys* **1918,** *2*, 98-100.

3.   Ledesma, C.; Yang, J.; Chen, D.; Holmen, A., *ACS Catalysis* **2014,** *4* (12), 4527-4547.

4.   Soares, R. d. P.; Secchi, A. R., EMSO: A new environment for modelling, simulation and optimisation. In *Computer Aided Chemical Engineering*, Elsevier: 2003; Vol. Volume 14, pp 947-952.

Chapter 3. Promoter and support influence on the intrinsic catalytic activity of iron and cobalt FT catalysts

3.1 Introduction

Promoters and supports have influence on the catalytic performance and catalyst structure of iron and cobalt based catalysts. In FTS the noble metals such as ruthenium (Ru), rhenium (Re), platinum (Pt) and palladium (Pd) are usually applied as promoters for cobalt catalysts in an effort to improve the catalyst reducibility, FT activity and/or modify the product selectivity.

Iron based catalysts has been demonstrated ability to produce directly light olefin from syngas operating in High Temperature Fischer-Tropsch synthesis (HTFT) [1, 2]. Moreover, iron FT catalysts can be efficient in the water gas shift reaction (WGS) in comparison with cobalt FT catalysts. The WGS leads to a lesser amount of water and increases hydrogen content in the reacting medium and thus, can be used to control the ratio of H_2 to CO during the reaction.

Several promoters for iron based catalysts have been widely applied in order to improve the FT reaction rate, iron dispersion and extent of iron carbidization. As commented in Chapter 1, alkali promoters change significantly the catalytic performance and catalyst structure. As an example, the K promoter improves selectivity towards the C_{5+} hydrocarbons, while Mg can enhance iron dispersion and also tune the product distribution to light hydrocarbons [3]. Application of bismuth (Bi) as promoter for iron catalyst is interesting due to the fact that the melting temperature point of the Bi metal (327 °C) is lower than the temperature applied in the FT reaction (350 °C). This leads to the pseudo-

liquid state of promoters at the reaction conditions, their migration and close contact between iron and promoter.

Cobalt based catalysts are the catalyst of choice for the Low Temperature Fischer-Tropsch synthesis (LTFT) which produces middle distillates and waxes. Use of noble metals as promoters leads to a significant increase in FT catalytic activity [4] in both slurry and fixed bed reactors [5, 6, 7]. Higher cost of noble metals makes however, challenging their application at industrial scale. For that reason, knowledge about the interaction of promoter and the catalyst active phase can be helpful.

Pt as a promoter for cobalt FT catalysts supported on alumina and silica has been demonstrated a strong effect on the FT reaction rate [8, 9]. Pt can influence catalyst properties e.g. modifies cobalt reducibility [10] by decreasing the activation energy to form the cobalt metallic phase [8]. On the other hand, a higher content of Pt (> 0.1 wt. %) may be responsible for both higher methane selectivity and a decrease in the selectivity to higher hydrocarbons. Higher Pt content in cobalt catalysts also significantly increases their cost.

The knowledge of the influence of catalyst support on FT catalyst is extremely important, once the support may significantly alter FT performance due to metal–support interactions, support acidity, porosity and mass transfer limitations [11, 12]. A wide range of supports materials can be used. Silica, alumina and titania are commonly commercial oxide supports for cobalt catalysts [13, 14, 15]. Even presenting a relatively weak interaction with cobalt, the silica support may cause formation of cobalt-silica mixed compounds, which can affect the FTS activity.

The high acidity and stability of zeolite materials can be used to control the FT selectivity. It was shown that the zeolite could perform hydrocarbon cracking and isomerization under the conditions of FTS [16, 17].

SSITKA provides information concerning kinetic surface parameters due to specific characteristic of support materials. Rane et al. [18] found different concentrations of CO and CH_x intermediates on the cobalt catalysts supported by γ, Φ-, δ- and α-Al_2O_3. The effect of the support on the SSITKA kinetic parameter was also observed by Kim Phan et al. [19] for cobalt catalysts supported on conventional and macroporous MPS alumina. The number of intermediates leading to methane (N_{CH4}) of cobalt supported on MPS-Al_2O_3

was higher (7.0 µmol/g) than that for $Co/\alpha\text{-}Al_2O_3$ (4.1 µmol/g). The Re promotion led to the increase in the number of CH_x intermediates to 11.3 µmol/g. This trend is correlated with the reaction rate constant, which was higher for cobalt Re-promoted supported on $MPS\text{-}Al_2O_3$. This is in agreement with earlier results of Frøseth et al. [20] and Hanssen et al. [21] who observed an increase in overall activity and in the concentration of active surface intermediates on promotion with Pt and Re.

The improvement in the catalytic activity for iron and cobalt based catalysts depends on several factors, such as type of catalytic support, metal promoter and reaction conditions. The aim of this chapter is to apply the kinetic transient techniques such as SSITKA to study the elementary steps of CO hydrogenation for iron and cobalt FT catalysts. The first part of this chapter has as the goal to evaluate the effects of bismuth (Bi) and lead (Pb) promotion on the catalytic performance of silica supported iron catalysts. After that, the effects of Pt promotion on the cobalt catalysts supported by the ZSM-5, MOR and BEA zeolites are investigated at different FT reaction conditions.

3.2 Results and discussion

3.2.1 SSITKA study of CO adsorption on the bismuth promoted iron catalyst

Prior to CO adsorption, the iron Bi-promoted catalyst was reduced using heating ramp of 3 °C/min, CO flow of 2 mL/min during 12 h at 350 °C. The determination of the total number of sites for iron based catalysts using CO adsorption by SSITKA switches was performed at different temperatures (350 °C, 100 °C and at room temperature). The gas composition during adsorption was 1 mL/min of CO with 0.5 mL/min of inert Ne.

Figure 3.1 shows the transient curve of ^{12}CO and inert gas during the CO adsorption for the Bi-promoted iron catalyst at 25 °C. Similar shape of the transient curves of CO was also obtained in all temperatures tested.
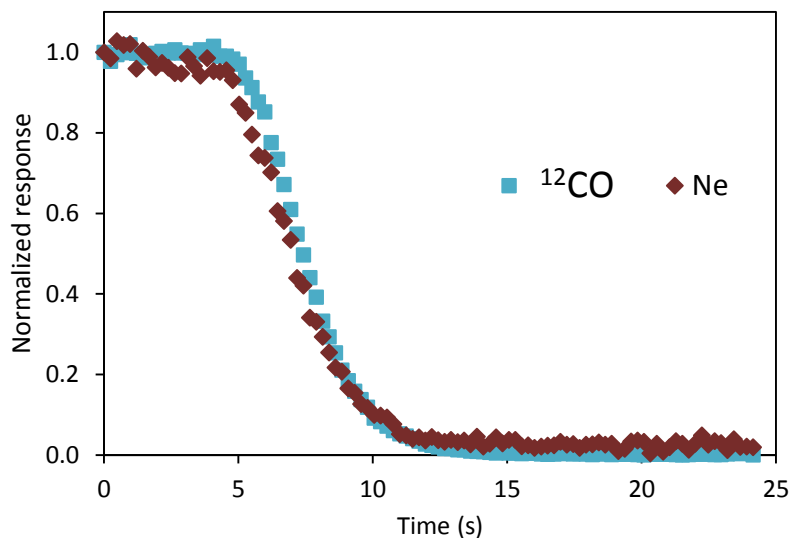
Figure 3.1 Transient curve of ^{12}CO and Ne during CO adsorption of silica supported iron catalyst at 25 °C.

The transient curves (Figure 3.1) clearly show that both CO adsorption and desorption are very fast processes on iron catalysts. The same overlapping of the transient response of CO with the inert gas was observed by Govender et al. [22] for iron catalyst promoted with K. The authors concluded that an accurate measure of CO chemisorption has to be performed for the iron based catalysts at low temperatures (−80 °C).

Recent DFT report [23] showed that differently to cobalt catalysts, direct carbon monoxide dissociation proceeds much easier on iron catalysts compared to the hydrogen assisted process. Carbon monoxide direct dissociation results in the formation of surface carbide and chemisorbed oxygen species followed by oxygen removal via their reaction either with hydrogen or carbon monoxide. Under FT reaction conditions, the chemisorbed carbon can be then hydrogenated to the CH_x monomer which is involved in the FT surface polymerization. It can be expected that the rate of these different elementary steps can be affected differently by the promoting elements. The next section displays the catalytic results obtained for the iron Bi and Pb promoted catalyst.

3.2.2 Catalytic performance and SSITKA analysis for iron Bi and Pb-promoted catalysts during CO hydrogenation

Methane, light C_2-C_4 olefins, light C_2-C_4 paraffins, C_5-C_{10} hydrocarbons, carbon dioxide and water were the principal products of carbon monoxide hydrogenation under the studied operating conditions. The catalysts were tested under a wide range of reaction pressures (1-20 bar). FT activity (FTY) increased 5 to 10 times on the promotion (Table 3.1). Interestingly, Fe catalysts promoted by the soldering metals were active even at low pressures, while no activity was observed over Fe/SiO_2.

Table 3.1 Catalytic performance of iron non-promoted and Bi and Pb-promoted catalyst at feed ratio $H_2/CO = 1$ after 60 h of reaction.

Catalyst	Reaction conditions			Activity		
	T (ºC)	P (bar)	GHSV (L/g h)	FTY 10^{-4} (mol/g_{Fe} s)	X_{CO} (%)	S_{CO_2} (%)
Fe/SiO$_2$	350	10	1.5	0.3	32	43
	350	10	3.4	0.4	16	35
	350	10	4.5	0.4	13	34
FeBi/SiO$_2$	350	10	1.4	1.8	21	42
	350	10	6.7	2.4	58	47
	350	10	3.4	1.8	75	49
	350	1	3.4	0.4	17	48
FePb/SiO$_2$	350	10	3.4	1.3	60	45
	350	1	3.4	1.2	55	45
	250	5	3.4	0.1	6	10

Figure 3.2 shows carbon monoxide conversion obtained on these catalysts at iso-GHSV but at different total pressures. As expected for the reference silica supported iron catalyst, carbon monoxide conversion strongly decreased with the decrease in total pressure. There was already no conversion at 5 bar which means that the unpromoted iron catalyst cannot be used for FTS at low pressure.
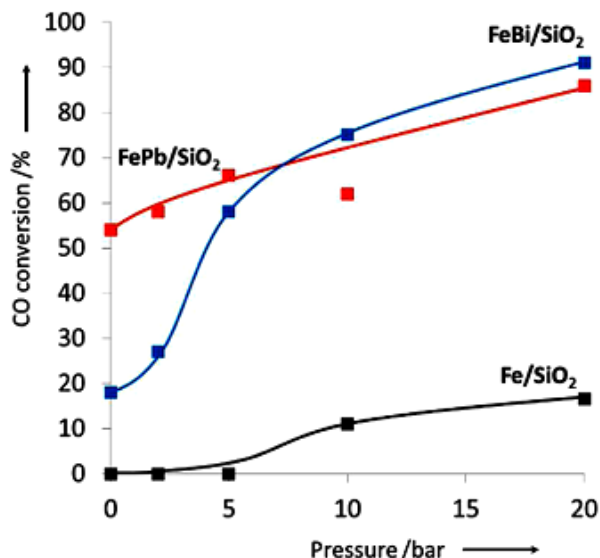
Figure 3.2 Carbon monoxide conversion on iron catalysts as a function of the reaction total pressure. Reaction conditions: T = 350 ºC, H_2/CO = 1, GHSV = 3.4 L/g h. The data were obtained by increasing pressure in the row 0 – 2 – 5 – 10 – 20 bar.

Surprisingly, the Bi- and Pb-promoted catalysts demonstrated significant activity even at atmospheric pressure. This is also indicative of significant modifications in the reaction kinetics and possibly mechanism of FTS. Note that the FTY observed over the Bi- and Pb-promoted Fe/SiO$_2$ (FTY 2.8·10^{-4} mol/g$_{Fe}$ s) catalysts was comparable with the most active iron catalytic systems known so far [2, 24, 25, 26] (FTY, Table 3.1). In the presence of the promoters, FTS might be performed at much milder conditions and even at atmospheric pressure (Table 3.1, Figure 3.2).
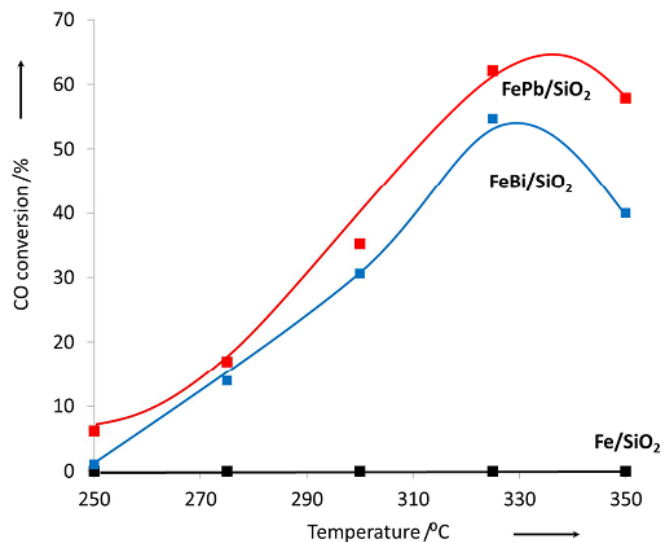
Figure 3.3 Effect of the type of promoter on the CO conversion at different temperatures. Reaction conditions: $P = 5$ bar, $H_2/CO = 1$, GHSV $= 3.4$ L/g h.

The promoted catalysts demonstrate continuous increase in the catalytic activity during the reaction. This is most probably due to optimization of active sites (Figure 3.4). Note that the unpromoted Fe/SiO_2 deactivates under the same conditions.
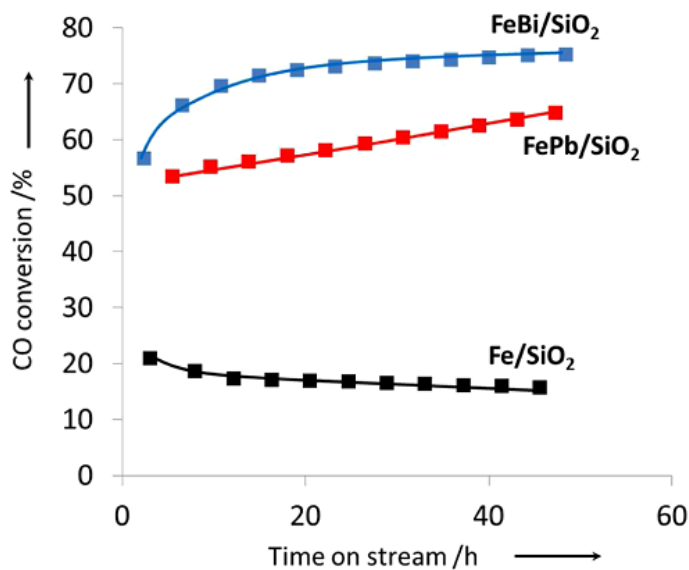
Figure 3.4 Effect of the type of promoter on the CO conversion as a function of time. Reaction conditions: $P = 10$ bar, $H_2/CO = 1$, GHSV $= 3.4$ L/g h.

69

The selectivity data for the Bi promoted iron catalyst and Fe/SiO$_2$ measured as a function of carbon monoxide conversion are summarized in Figures 3.5, 3.6 and 3.7.
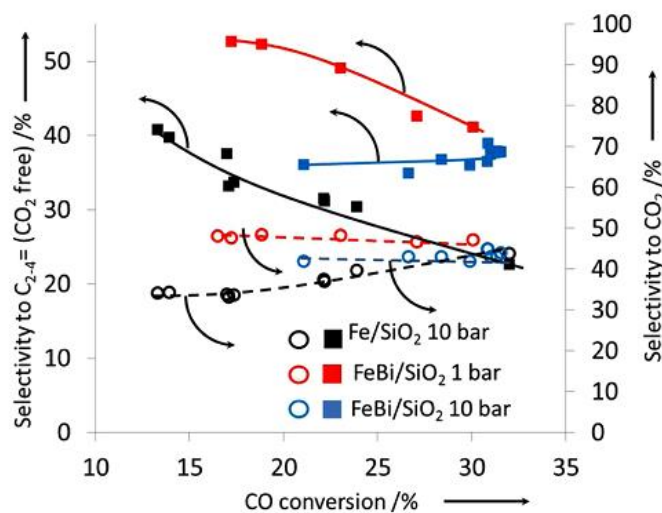
Figure 3.5 Effect of Bi promoter on the selectivity versus CO conversion. Reaction conditions: T= 350 °C, H$_2$/CO = 1, P = 1 and 10 bar for FeBi/SiO$_2$ and Fe/SiO$_2$, respectively, GHSV = 1.5−27 L/g h.

Similar catalytic performance has been observed for the lead promoted catalysts (see Table 3.2). The reactions occurring during FTS over iron catalysts are displayed below:

$$nCO + 2nH_2 = C_nH_{2n} + nH_2O \tag{1}$$

$$CO + H_2O = CO_2 + H_2 \tag{2}$$

$$2nCO + nH_2 = C_nH_{2n} + nCO_2 \tag{3}$$
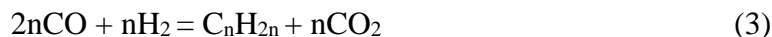
For the Fe/SiO$_2$ catalyst, carbon dioxide selectivity increases with carbon monoxide conversion moving to the stoichiometric value of 50% (Figure 3.5, Eq. 3). This is consistent with the hypothesis that carbon dioxide can be produced by WGS which is secondary reaction of FTS (Eq. 2). Note however that over the Bi and Pb-promoted catalysts, high carbon dioxide selectivity is observed even at very low carbon monoxide conversion levels (Figure 3.5, Table 3.2). This suggests that on these catalysts, the primary route of carbon

dioxide formation might take place together with the secondary reaction occurring through reaction of carbon monoxide with the water produced by WGS.
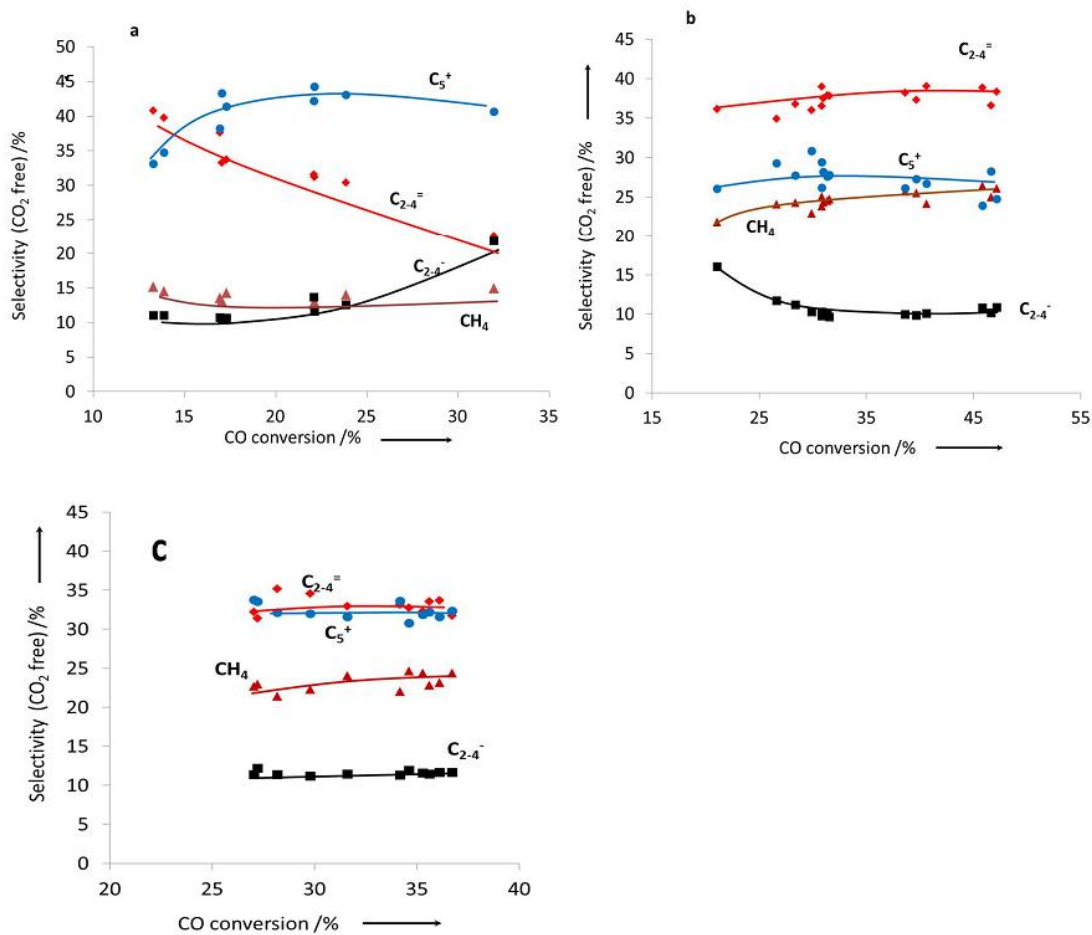
Figure 3.6 Selectivity to hydrocarbons versus CO conversion over Fe/SiO$_2$ (a), FeBi/SiO$_2$ (b) and FePb/SiO$_2$ (c) catalyst. Reaction conditions: P = 10 bar, H$_2$/CO = 1, GHSV = 1.5-27 L/g h.
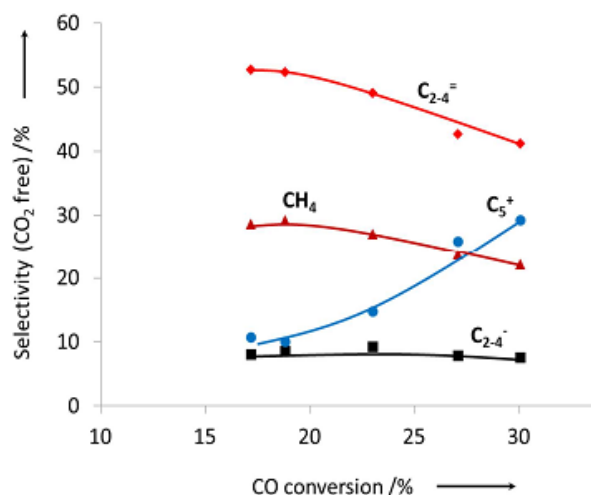
Figure 3.7 Selectivity to hydrocarbons versus CO conversion over the FeBi/SiO$_2$ catalyst. Reaction conditions: P = 1 bar, H$_2$/CO = 1, GHSV = 1.5-7.5 L/g h, T = 350 ºC.

Note also that the selectivity to light olefins decreases with an increase in CO conversion over Fe/SiO$_2$ catalyst which is probably due to secondary hydrogenation of olefins to alkanes [27] (Table 3.2, Figure 3.5). The presence of promoters stabilizes selectivity to light olefins close to 35% at high conversions at 10 bar with suppression of the secondary transformation of olefins (Figure 3.6). This effect is similar to those observed in the presence of alkali promoters.

Table 3.2 Product distribution of iron unpromoted and Bi and Pb-promoted catalyst at feed ratio H$_2$/CO = 1 after 60 h of reaction.

| Catalyst | Reaction conditions | | | Selectivity | | | | |
| | | | | Product distribution (%C$_{at}$, CO$_2$ free) | | | | |
	T (ºC)	P (bar)	GHSV (L/g h)	S$_{CH4}$ (%)	S$_{C2\text{-}C4}^=$ (%)	S$_{C2\text{-}C4}^-$ (%)	S$_{C5+}$ (%)	α
Fe/SiO$_2$	350	10	1.5	15	22	22	40	0.5
	350	10	3.4	14	33	10	43	0.48
	350	10	4.5	15	41	11	33	0.48
FeBi/SiO$_2$	350	10	1.4	27	36	16	21	0.46
	350	10	6.7	24	32	17	27	0.47
	350	10	3.4	24	26	21	29	0.48
	350	1	3.4	29	53	8	10	0.35
FePb/SiO$_2$	350	10	3.4	20	31	11	38	0.48
	350	1	3.4	22	32	12	34	0.39
	250	5	3.4	15	26	9	50	0.54

Differently to alkali promotion, the Bi and Pb-promoted catalysts exhibit lower selectivity to the long chain hydrocarbons. High selectivity to long chain hydrocarbons limits the selectivity to light olefins over alkali-promoted catalysts. At lower reaction pressures (1 bar), the selectivity to light olefins can be further increased by about 20% reaching 53% at the conversions of 17% which corresponds to the best published reports [25, 28, 29**Erro! Indicador não definido.**] (Table 3.1, Figures 3.5 and 3.7).

Importantly, the increase in the selectivity to light olefins at lower reaction pressure coincides with the decrease in the selectivity to the C_{5+} hydrocarbons (Figure 3.7). This seems to be due to the gradual decrease in the chain growth probability (α) with the pressure decrease (Figure 3.8). The Anderson-Schulz-Flory distribution predicts maximum selectivities to the C_2-C_4 hydrocarbons about 50% at α between 0.3 and 0.6 [30]. The pressure decrease from 10 to 1 bar leads to the decrease in α from 0.5 to 0.35 which is favorable for higher olefin selectivity.
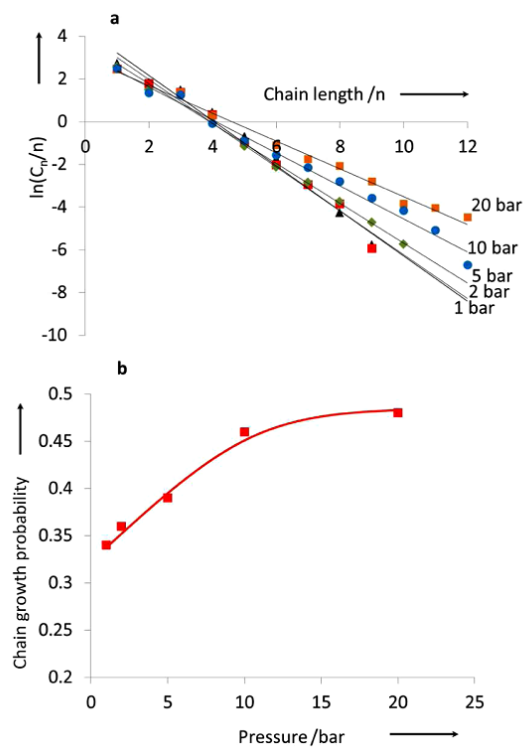
Figure 3.8 (a) ASF plots and (b) chain growth probabilities over FeBi/SiO$_2$ catalyst at different pressures. Reaction conditions: P = 1−20 bar, H$_2$/CO = 1, GHSV = 1.5−3.4 L/g h, T = 350 °C. The conversion was about 30%.

It is interesting to note that increase in the CO conversion at atmospheric pressure leads to the gradual decrease in the selectivity to light olefins (Figure 3.5 and Figure 3.7) in comparison with a more stable selectivity to olefins as a function of conversion at higher pressure. The chain growth probability does not change significantly in the case. The possible explanation of this effect could be reinsertion of light olefins in the growing chains at higher CO conversion at low pressure leading to decrease in the selectivity to light olefins and increase in the selectivity to C_{5+} hydrocarbons.

Thus, use of soldering metal promoters makes it possible to produce light olefins over iron catalysts with high yield and selectivity. Note that the selectivity gain is more pronounced at lower reaction pressure.

3.2.3 Mechanism of the promotion of iron catalysts with Bi and Pb

Previous reports suggest [2, 24, 31, 32, 33] that FT reaction on iron catalysts occurs over iron carbides. FT reaction rate on the iron catalysts could be therefore a function of the number and intrinsic reactivity (turnover frequency) of iron carbide surface sites [34]. The concentration of iron carbide surface sites is a function of iron carbide dispersion and extent of carbidization.

Investigation of the calcined catalysts by XRD (Figure 3.9) did not reveal any effect of the promoters on the dispersion of supported hematite iron oxide. The size of iron oxide particles was always between 15 and 17 nm and was not much affected by the promoters.
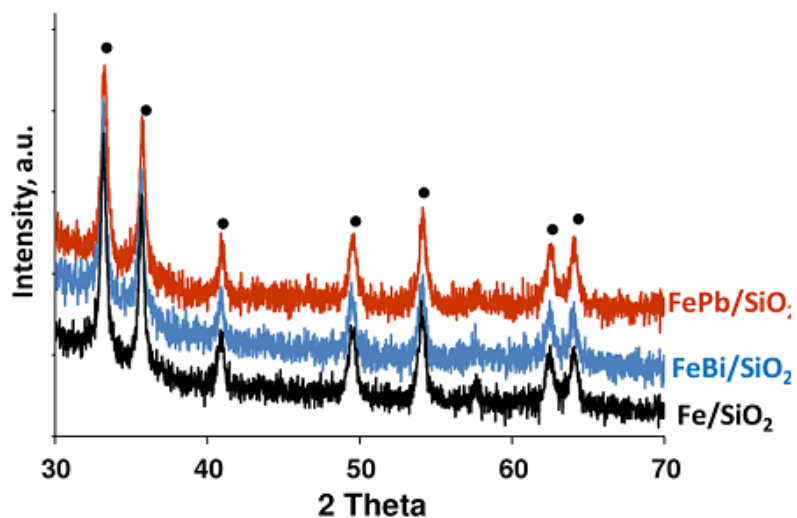
Figure 3.9 XRD patterns of the catalysts after calcination.

Figure 3.10 displays XRD patterns of the unpromoted and Bi and Pb-promoted iron catalysts after the FT reaction tests. Very broad XRD peaks attributed to iron carbide phase has been detected. Again, the width of the iron carbide XRD peaks has not also much affected by the promotion. The sizes of iron carbide nanoparticles according to XRD were in the range from 4 to 6 nm. This suggests that iron carbide dispersion is also not affected by the promotion with soldering metals.
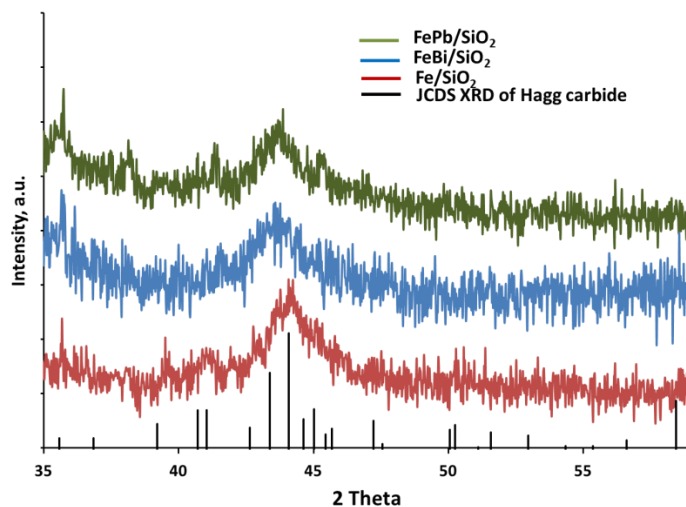
Figure 3.10 XRD patterns of the catalysts after FT reaction.

The in-situ magnetic method (Figure 3.11) did not either reveal any effect of the promoters on the extent of carbidization and chemical composition of iron carbide phases. Prior to the magnetic measurements, the catalysts were treated in CO at 350 °C using the procedure similar to that used for catalyst activation.

Catalyst magnetization was zero at temperatures higher than the Curie temperature of Hagg iron carbide. Magnetite has the Curie temperature at 585 °C and (if present in the catalysts) must be detected by the magnetic method. Thus, the observed zero magnetization at temperature higher than 250 °C suggests complete iron carbidization and thus, extremely low concentration of magnetite in the activated catalysts. In addition, catalyst magnetization at room temperature in the catalysts carbidized in CO at 350 °C was the same for unpromoted and promoted catalysts. This is indicative of the same concentration of iron carbide. The Curie temperature (205-220 °C) measured in both unpromoted and promoted catalysts corresponded to the Hägg iron carbide (χ-Fe_5C_2).
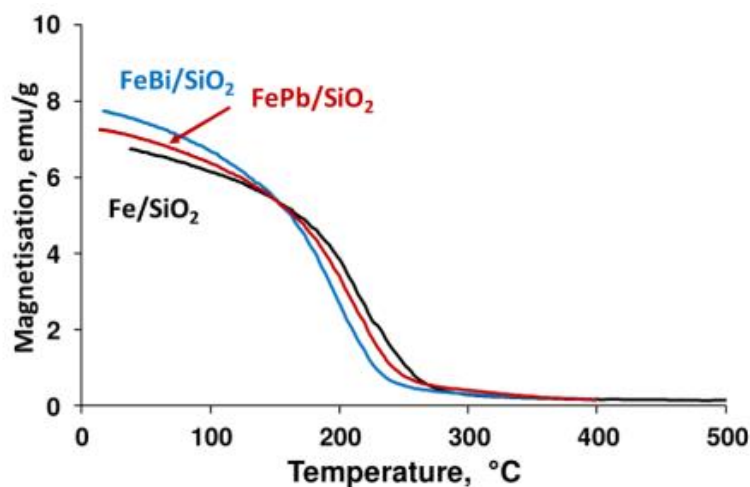
Figure 3.11 Catalyst magnetization during cooling down after CO treatment at 350 ℃.

The catalytic phenomena over the Bi- and Pb-promoted catalysts cannot be therefore attributed to the changes in the iron carbide dispersion, amount and composition. Thus, the performance of the promoted catalysts seems to be affected not by variation of the number of active sites but by the modification of their intrinsic activity (turnover frequency).

The reactivity of iron carbide in the promoted and unpromoted catalysts has been characterized by hydrogenation at the reaction conditions. Our earlier study [35] indicated that the catalysts with higher rate of iron carbide hydrogenation exhibited high activity in FTS. The comparable hydrogenation profiles were observed with unpromoted and promoted catalysts. The results suggest no significant difference in the concentration and reactivity of the iron carbide species in the unpromoted and promoted catalysts in the presence of hydrogen (Figure 3.12).
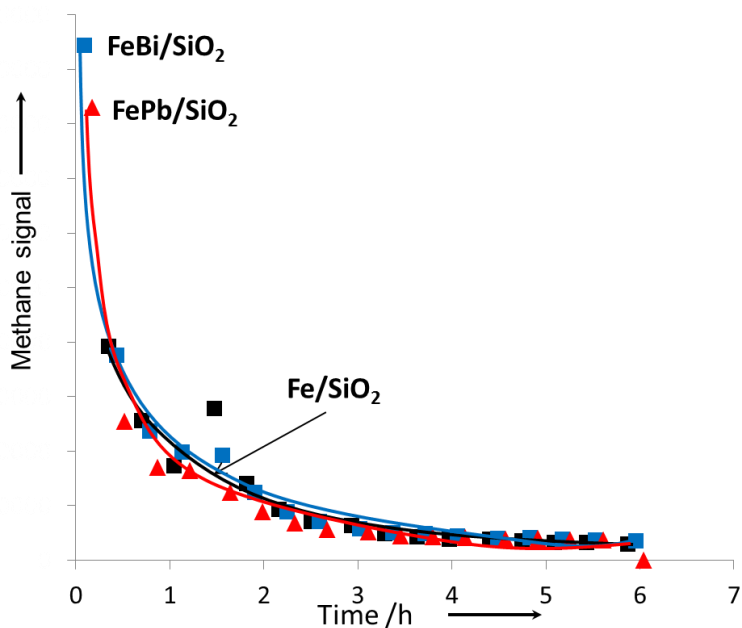
Figure 3.12 Methane formation rate in static hydrogenation of carbidized Fe/SiO$_2$, FePb/SiO$_2$ and FeBi/SiO$_2$.

The observed strong effects of the Bi and Pb promoters on the catalytic performance of Fe catalysts might be due to the intimate contact between Fe and promoter. It is expected that low melting point of soldering metals can lead to their higher mobility. In order to prove it, we have prepared mechanical mixtures of Fe/SiO$_2$ with either Bi/SiO$_2$ or Pb/SiO$_2$ and performed catalytic tests (Table 3.1, Figure 3.13).
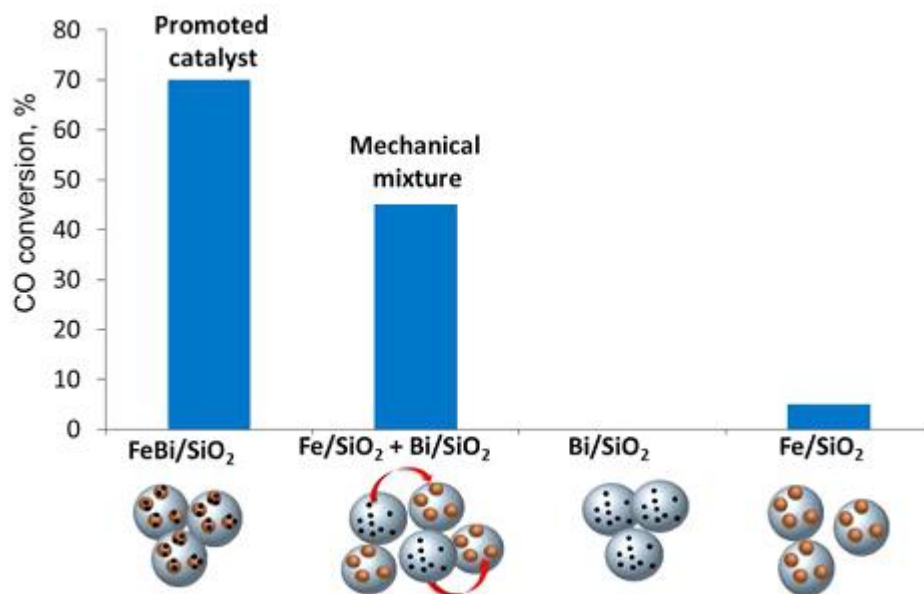
Figure 3.13 Conversion of CO over FeBi/SiO$_2$, Bi/SiO$_2$, Fe/SiO$_2$, and mechanical mixture Fe/SiO$_2$ + Bi/SiO$_2$. Reaction conditions: H$_2$/CO = 1, P = 10 bar, T = 350 °C, GHSV = 3.4 L/g h, TOS = 100 h.

CO conversion over mechanical mixtures was much higher than over the unpromoted Fe/SiO$_2$ and comparable with the conversion over the co-impregnated promoted catalysts. This is indicative of substantial migration of the promoters during the reaction. The conducted TEM-EDX confirms this assumption (Figure 3.14).
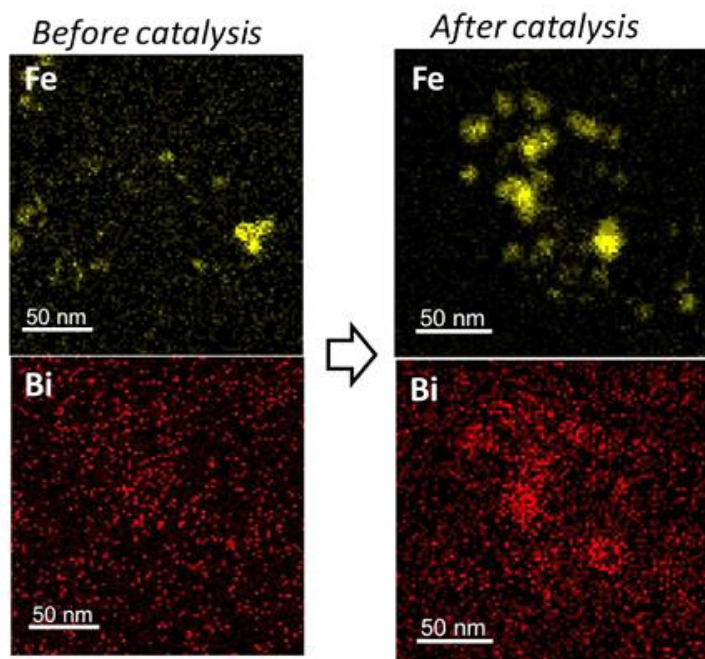
Figure 3.14 TEM-EDX images for Fe and Bi before after catalysis for the mechanical mixture Fe/SiO$_2$ + Bi/SiO$_2$ (see Figure 3.13).

In the mechanically mixed sample, TEM-EDX detected both Fe nanoparticles in the range of 10-40 nm and Bi particles which were much smaller because of lower metal content. Note that in the initial mechanical mixtures, Bi was uniformly distributed with the same density in all parts of the image (Figure 3.14). After conducting FTS, the EDX maps clearly show preferential Bi localization in a close proximity of iron carbide nanoparticles (Figure 3.14).

The significant increase in the density of Bi in the interface with Fe nanoparticles might be explained by migration of Bi under the reaction conditions and their interaction with iron. This high mobility might result in sintering of the promoter in long-term test. However, several days of experiment leads only to the increase in the activity (Figure 3.4) most probably due to activation of Fe sites by interaction with promoter. Thus, longer experiments are necessary to clarify further behavior of promoter during the catalysis.

FTS is a multistage catalytic reaction. Previous reports suggest that FTS over iron catalysts may proceed with the Mars-Van Kravelen sequence [36, 37]. One of the initial steps of FTS on iron catalysts is carbon monoxide dissociative adsorption. Carbon

monoxide dissociation over iron catalysts can be either direct or hydrogen-assisted. Recent DFT report [23] showed that differently to cobalt catalysts, direct carbon monoxide dissociation proceeds much more easily on iron catalysts compared to the hydrogen assisted process.

Carbon monoxide direct dissociation results in formation of surface carbide and chemisorbed oxygen species followed by oxygen removal via its reaction either with hydrogen or carbon monoxide. Chemisorbed carbon can be then hydrogenated to CH_x monomer, which then can be involved in the FT surface polymerization. It can be expected that the rate of these different elementary steps can be affected differently by the promoting elements. First, the rate of carbon monoxide adsorption and dissociation on the unpromoted and Bi- and Pb-promoted iron catalysts in the presence of syngas and at the reaction temperature (350 °C) was evaluated using SSITKA [38, 39, 40]. During the switches from $^{12}CO/H_2/Ne$ to $^{13}CO/H_2$, the ^{12}CO carbon monoxide response curves were indistinguishable from the transient response of the inert gas (Figure 3.15). This suggests that the rates of carbon monoxide adsorption and desorption are very fast on both unprompted and promoted iron catalysts.

Importantly, no molecular adsorption of carbon monoxide was observed on iron carbide under the reaction conditions. This also suggests that the only type of CO dissociative adsorption on iron catalysts can be dissociative.
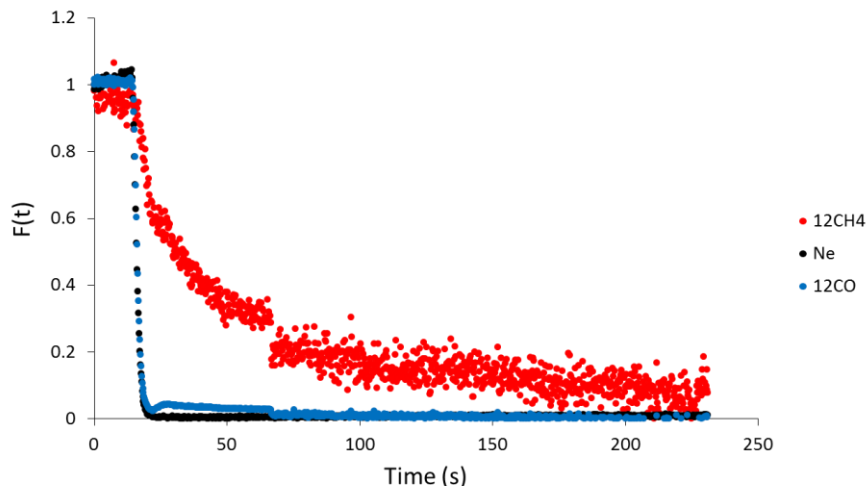
Figure 3.15 SSITKA results over FeBi/SiO$_2$. Reaction conditions: P = 1 bar, H$_2$/CO = 2, GHSV = 8.4 L/g h, T = 350 °C.

The rates of oxygen removal produced on CO dissociation on the Bi-, Pb-promoted and unpromoted iron catalysts were evaluated by the reaction with carbon monoxide. The unpromoted and Bi- and Pb-promoted catalysts were first carbidized in carbon monoxide under typical conditions used for the catalyst activation. Then the catalysts were exposed to water to generate oxygen species on the catalyst surface. During the contact of the catalyst with water, hydrogen formation has been observed (Figure 3.16).
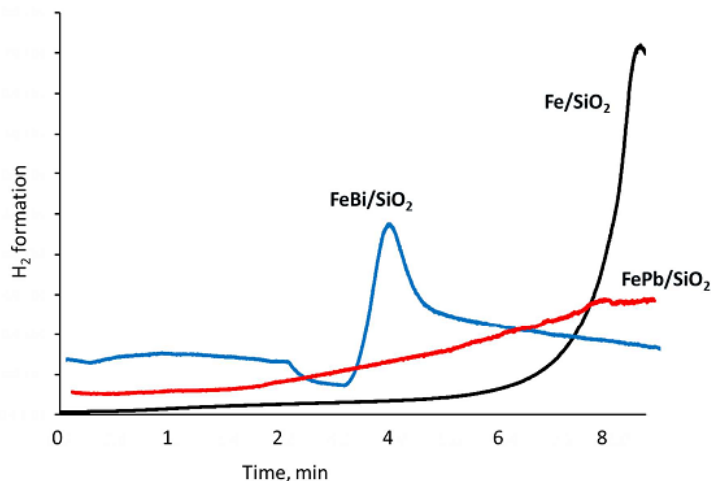
Figure 3.16 Rate of hydrogen production after exposure of the activated silica supported iron catalysts to water vapours. Reaction conditions: P = 1 bar, H$_2$O flow 0.3 mL/h, T = 350 °C.

Hydrogen formation probably comes from the oxidation of iron carbide with water. Interestingly, hydrogen production rate and oxidation of iron carbide in the unpromoted catalyst were slow. At the same time, over the promoted catalysts intensive and rapid hydrogen formation has been observed at lower reaction time.

After this treatment, the catalysts were again exposed to carbon monoxide to evaluate the reactivity of the generated oxygen species in the presence of carbon monoxide. Carbon dioxide production rates from CO after partial oxidation of carbide surface in water are displayed in Figure 3.17.
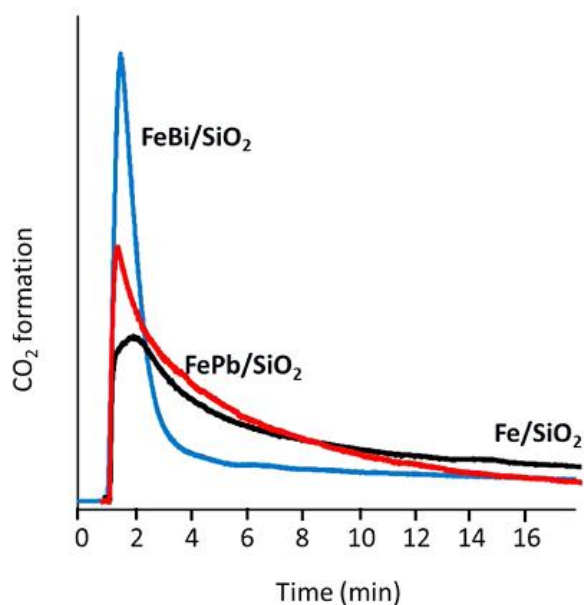
Figure 3.17 Rate of carbon dioxide production after exposure of the activated silica supported iron catalysts pretreated with water to CO at 300 °C.

Interestingly, the rates of carbon dioxide production were much higher over the Pb– and in particular Bi-promoted catalysts compared to the unpromoted counterpart. The trend was similar to the hydrogen rate formation during catalyst oxidation by water. This suggests that the rates of oxygen scavenging and its removal via its reaction with carbon monoxide are significantly enhanced in the presence of promoters. It is relevant to the enhancement of the diffusion of the oxygen formed on iron carbide during CO dissociation to the promoting atoms (Bi or Pb) situated in a close proximity. Oxygen migration to the promoters leads to their partial oxidation.

Oxygen species will be then removed much more easily from the promoter by CO than those located on the surface of iron carbide. The observed trend is consistent with electrochemical potentials of iron ($Fe^{2+} + 2e- \rightleftharpoons Fe(s)$ -0.44V), bismuth ($Bi^{3+} + 3e- \rightleftharpoons Bi(s)$ +0.308 V) and lead ($Pb^{2+} + 2e- \rightleftharpoons Pb(s)$ −0.126 V). Oxygen removal by reaction with CO leading to the reduction of the promoter will be thermodynamically favored on Bi and Pb compared to Fe.

This suggestion is also consistent with the XPS characterization data. The Pb-promoted and unpromoted iron catalysts were activated in carbon monoxide and exposed to syngas in the pretreatment chamber of XPS spectrometer. For XPS analysis, the catalyst was transferred without exposure to air from the pretreatment chamber to XPS analysis chamber (Figure 3.18).
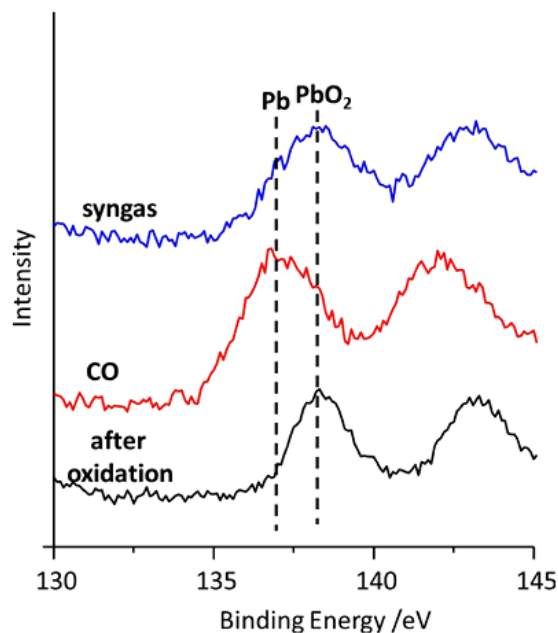
Figure 3.18 Pb 4f XPS spectra of the FePb/SiO$_2$ catalyst after calcination and exposure to carbon monoxide and syngas.

Note that before the reaction, Pb was in the oxidized state. In the catalyst activated in carbon monoxide, Pb was mostly observed in the metallic state. This suggests that the catalyst treatment with carbon monoxide results in the removal of all oxygen atoms from the promoter and its reduction to the metallic state. Interestingly, noticeable modifications

of the XPS spectra of lead were observed after the exposure of the activated catalyst to syngas.

The presence of syngas resulted in lead oxidation. This is consistent with the hypothesis about scavenging of oxygen atoms formed on carbon monoxide dissociation on iron carbide by the promoter, followed by the removal of oxygen species from the promoter with carbon monoxide. This suggestion agrees with high CO_2 selectivity at low carbon monoxide conversion observed on the promoted catalysts indicating that CO_2 is a primary reaction product over the Bi- and Pb-promoted catalysts.

3.2.4 Pt-promoter effect on the kinetic parameters for cobalt catalyst during FTS

This section presents catalytic performance and SSITKA analysis for the cobalt Pt-promoted and non-promoted during FTS. Figure 3.19(a,b) shows CO conversion as a function of time on stream of non-promoted and Pt-promoted cobalt catalysts for H_2/CO ratio feed of 2 and 5. The Pt-promoted catalyst presented better catalytic performance, since the CO conversions are higher during whole time at feed ratio of H_2/CO equal to 2 (see Figure 3.19a). Similar behavior was noticed by Jacobs et al. [6] using Pt and Ru on the alumina, titania and silica supported catalysts.

For the non-promoted catalyst at H_2/CO ratio feed of 2, CO conversion slightly decreased at the first hour of reaction. Considering the whole time on stream (around 13 h), the non-promoted catalyst lost 50% of the CO conversion, contrasting with the 30% of reduction for the Pt-promoted cobalt catalyst. Increasing hydrogen partial pressure from 0.29 bar to 0.58 bar improved catalyst stability for both samples. In fact, the promoted Pt catalyst became completely stable during 14 hours of reaction. The non-promoted had a slightly decrease in CO conversion from 15% to 11%.
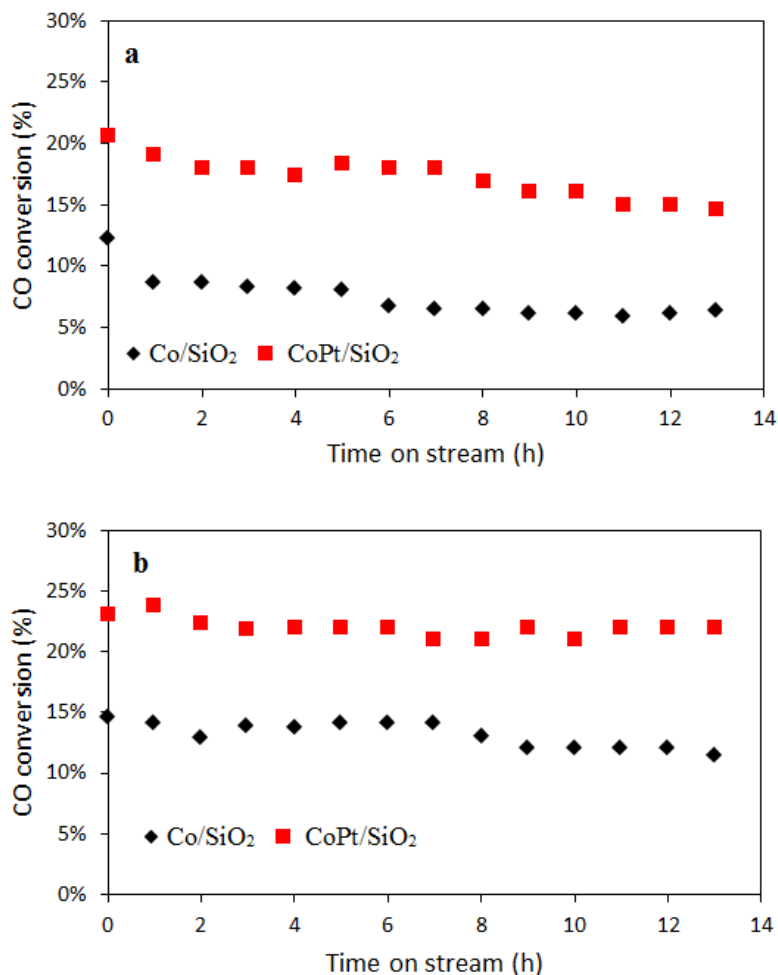
Figure 3.19 CO conversion in function of time on stream for non-promoted and promoted cobalt catalysts at (a) Ratio H_2/CO 2 and (b) Ratio H_2/CO 5. Reaction conditions: 250 °C, GHSV = 12 000 mL/g h and 16 000 mL/g h.

The literature points out that the presence of noble metal has the ability to restrict formation of cobalt support mixed oxides during FTS [4, 41]. The promoter effect over catalyst stability is also associated to the type of support applied.

85

Table 3.3 Catalytic performance for promoted Pt and unpromoted cobalt catalysts. Reaction conditions: T = 250 °C, GHSV = 12 000 mL/g h and 16 000 mL/g h.

Catalyst	Ratio feed H_2/CO	XCO (%)	SCH_4 (%)	Rate (μmol/g s)	R_{SSITKA} (μmol/g s)
Co/SiO$_2$	2	6	86	1.1	0.9
	5	11	92	1.9	1.8
CoPt/SiO$_2$	2	15	85	2.5	2.1
	5	21	93	3.6	3.3

The increase of the H_2/CO feed ratio influenced the catalyst activity for both cobalt catalysts. This may be correlated to the reaction condition applied, due to the influence of Pt over FT reaction rate be more noticeable at atmospheric pressure [9, 42]. Note that the rate constant determined by GC analysis at conventional steady state conditions presents similar values with the rate constant in the SSITKA experiments. As showed in Table 3.3, methane is the major product of the reaction under these conditions for both catalysts, with methane selectivity higher than 80%.

Table 3.4 shows the surface residence time and number of active sites measured by SSITKA.

Table 3.4 Total number of active sites by CO adsorption and SSITKA data for CO hydrogenation under different ratio feed of H_2/CO in the presence of promoter (Pt) and without promoter.

Catalyst	Ratio H_2/CO	τ_{CO} (s)	τ_{CH4} (s)	N_{CO} (μmol/g)	N_{CH4} (μmol/g)	TOF_{SSITKA} (s^{-1})
Co/SiO$_2$	2	2.3	19	38	17	0.018
	5	2.0	13	31	24	0.036
CoPt/SiO$_2$	2	2.8	17	39	35	0.029
	5	1.8	11.5	23	38	0.047

Cobalt Pt-promoted catalysts present larger amount of intermediates leading to methane in comparison with the non-promoted samples. Such result is interesting, once SSITKA studies has demonstrated that higher coverage of N_{CH4} intermediates could lead to a high chain growth probability, which causes an increase in the selectivity toward the C_{5+} hydrocarbons and a decrease in the selectivity to methane [43, 44].

The higher number of intermediates combined with a slightly fast lifetime of intermediates in the promoted cobalt catalyst are responsible for 2 times higher TOF_{SSITKA} for the Pt-promoted catalyst compared to the unpromoted counterpart. Hence, it is possible to conclude that addition of the Pt-promoter results in a significant increase in the activity.

Table 3.4 also demonstrates the effect of the H_2/CO feed ratio. In this case, the lifetime of intermediates leading to methane are shorter due to higher number of available hydrogen species and faster hydrogenation during the reaction.

3.2.5 Effect of cobalt supports on the total number of active sites

All catalysts were submitted before CO adsorption to reduction in hydrogen flow of 8 mL/min at 400 °C in temperature ramp of 5 °C/min. The reduction temperature of the cobalt supported on the zeolites was also determined in the work by Subramanian et al.

[16] by temperature-programmed reduction with hydrogen (H_2-TPR). There was a single group of peaks around 350-400 °C assigned to the reduction of cobalt oxide species to metallic phases.

In terms of zeolite surface area and pore volume, Subramanian et al. [16] observed that after the impregnation of about 20 wt. % of Co, a decrease in zeolite BEA was around 50%, followed by MOR (around 20%) and ZSM-5 (10%). The surface area and pore volume of Co/ZSM-5 decreases only slightly after impregnation relative to the parent zeolite.

The 3D pore structure of BEA (0.76×0.64 nm) is more open than that of MOR (0.65×0.7 nm; 1 D) and ZSM-5 (approximately 0.55 nm; 3D). A more significant decrease in the BET surface area and micropore volume of BEA compared to that of ZSM-5 and MOR could be assigned, therefore, to a much easier diffusion of Co species into the BEA zeolite pores during the impregnation. This would result in a higher Co fraction in the BEA pores.

The SSITKA switch from ^{12}CO/He/Ne to ^{13}CO/He was realized to determine the total number of active sites in the catalysts with 20% of cobalt and 0.1% of Pt supported on silica and on ZSM-5, MOR and BEA zeolites. As shown in the Table 3.5, the CO surface residence time (τ_{CO}) for cobalt supported on silica was 5.2 s contrasting with an average residence time of 3.5 s for the cobalt supported on all zeolites. This proves stronger interplay between the gas phase and cobalt nanoparticles on silica support. The concentration of reversibly adsorbed carbon monoxide (N_{CO}) on cobalt supported on silica is higher than that for cobalt supported on the zeolites.

Table 3.5 Catalysts characterization and SSITKA CO adsorption data (switches between $^{12}CO/He/Ne$ and $^{13}CO/He$).

Catalyst	Co size (nm)[a]	τ_{CO} (s)	N_{CO}[b] (μmol/g)	N_{CO}[c] in H_2 presence (μmol/g)
CoPt/SiO$_2$	17.3	5.2	90	90
CoPt/ZSM-5	26.4	3.0	49.6	-
CoPt/BEA	16.2	2.9	51.1	53
CoPt/MOR	27.5	3.5	60.2	-

[a] Co = 0.75 · dCobalt oxide (nm). Determined by XRD analysis.
[b] Amount of CO adsorbed at 100 °C, evaluated from SSITKA.
[c] Amount of CO adsorbed at 100 °C in presence of hydrogen ($H_2/CO = 10$), evaluated from SSITKA.

The phenomena described in the previous paragraph are related to the catalyst support porosity, since cobalt catalyst supported on silica presents large total pore volume (0.85 cm^3/g). The total pore volume of cobalt supported on BEA, ZSM-5 and MOR is 0.18 cm^3/g, 0.16 cm^3/g and 0.21 cm^3/g, respectively [16].

The switch during the CO adsorption in presence of hydrogen (from $^{12}CO/H_2/He/Ne$ to $^{13}CO/H_2/He$) was done for the silica and BEA supported cobalt catalysts (see Table 3.5). The concentration of reversibly adsorbed carbon monoxide (N_{CO}) of both samples in the presence of hydrogen shows that in the adsorption conditions applied (T = 100 °C) there is non-competition between H_2 and CO for active sites. Hence, CO is a dominating specie on the surface of the amorphous silica and on the BEA zeolite, which is in agreement with Frøseth et al. [20], for cobalt supported on alumina, TiO$_2$ with and without Re as promoter. However, Enger et al. [45] noticed different trend for cobalt supported on different modified aluminas with and without promoters such as Zn, Re, Ni and Mg. The authors have found that the co-adsorption of CO with H_2 prior to the reaction

showed an apparent competitive H_2-CO adsorption which resulted in a lower CO saturation coverage than with only CO feed.

A different value of reversibly adsorbed carbon monoxide (N_{CO}) is a consequence of the interaction between cobalt nanoparticles and support. As commented by Yang et al. [46] and Zhang et al. [47], this can be related to the surface reconstruction caused by CO adsorption and/or an electronic effect induced by supports.

3.2.6 Influence of the zeolite support on the intrinsic kinetic parameters of cobalt catalyst during FTS

This section presents both catalytic activity and SSITKA study for conventional silica FT support as well for the cobalt catalysts supported on the ZSM-5, MOR and BEA zeolites. All cobalt based catalysts were reduced in hydrogen flow of 8 mL/min at 400 °C. Afterwards, the samples were cooled down to the reaction temperature of 250 °C. At ambient pressure and after 3 h of reaction, SSITKA measurements were done on all cobalt based catalysts under different feed H_2/CO ratios (2, 5 and 10) corresponding to hydrogen partial pressure of 0.29 bar, 0.58 bar and 0.83 bar, respectively.

Carbon monoxide conversion and methane selectivity measured at quasi-steady state reaction conditions as a function of the H_2/CO feed ratio for each catalyst are displayed in Figure 3.20 and Table 3.6. Methane was the major product for all samples under applied conditions. At the H_2/CO feed ratio of 2, higher carbon monoxide conversion was observed using MOR as support, followed by SiO_2, BEA and ZSM-5 zeolites. However, increasing the hydrogen partial pressure in the feed strongly affects CO conversion on silica supported catalyst, making the CO conversion the same as on Co/MOR at H_2/CO ratio feed of 5. Approximately 50% of CO conversion was obtained for silica supported cobalt catalyst at ratio H_2/CO of 10.
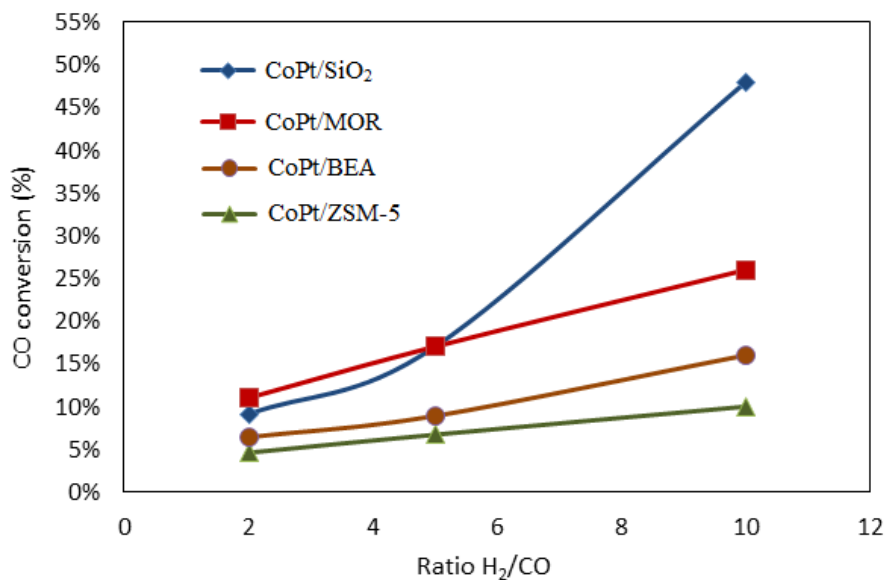
Figure 3.20 CO conversion in function of ratio feed H_2/CO for cobalt supported on silica, BEA, MOR and ZSM-5. Reaction condition: P ambient, 250 °C, GHSV = 13 500 mL/g h, 18 000 mL/g h and 23 850 mL/g h.

Among the zeolites, in the range of hydrogen partial pressure, the CO conversion was higher for the cobalt catalysts supported on MOR, followed by BEA and ZSM-5. The ZSM-5 supported cobalt catalyst presented the smallest FT reaction rate (see Table 3.6).

Table 3.6 shows the SSITKA data for each catalyst as functions of the H_2/CO feed ratio. In the case of zeolite supports, the CO residence time (τ_{CO}) slightly decreases or even remains constant as a function of H_2 partial pressure.

Table 3.6 GC analysis and SSITKA results under different feed ratio of H_2/CO. Reaction condition: P ambient, 250 °C, GHSV = 13 500 mL/g h, 18 000 mL/g h and 23 850 mL/g h.

Catalyst	H_2/CO	XCO	SCH_4	FT rate 10^{-6} (mol/g_{cat} s)	τ_{CO} (s)	τ_{CH4} (s)
CoPt/SiO$_2$	2	9.1%	67%	1.6	4.9	18.8
	5	17%	75%	2.9	3.4	17.5
	10	48%	60%	-	-	-
CoPt/MOR	2	11%	78%	1.9	3.1	16.9
	5	17%	82%	3.0	2.5	12
	10	26%	78%	4.0	2.9	12.1
CoPt/ZSM-5	2	4.6%	71%	0.8	2.0	19.0
	5	6.7%	87%	1.1	2.0	16.6
	10	10%	90%	1.6	2.4	12.4
CoPt/BEA	2	6.4%	82%	1.1	2.7	17.3
	5	8.9%	87%	1.5	2.5	13.9
	10	16%	75%	2.5	2.3	12.1

Figure 3.21 shows the transient curves of CH_4 surface residence time for each catalyst at H_2/CO ratio feed of 2, 5 and 10. The transient curves helps to understand the influence of H_2 to CO feed ratio on the catalytic activity behavior, once faster CH_4 intermediates were found at higher partial pressure of hydrogen. Frøseth et al. [48] found that increasing H_2/CO ratio affects slightly the surface residence time of intermediates (τ_{CH4}). On the other hand, Panpranot et al. [49] observed for amorphous and mesoporous silica, a consistently drop of τ_{CH4} with increasing hydrogen partial pressure. The authors also concluded that the intrinsic site activity and concentration of surface intermediates for CO hydrogenation were strongly dependent on the hydrogen partial pressure for both supports applied.
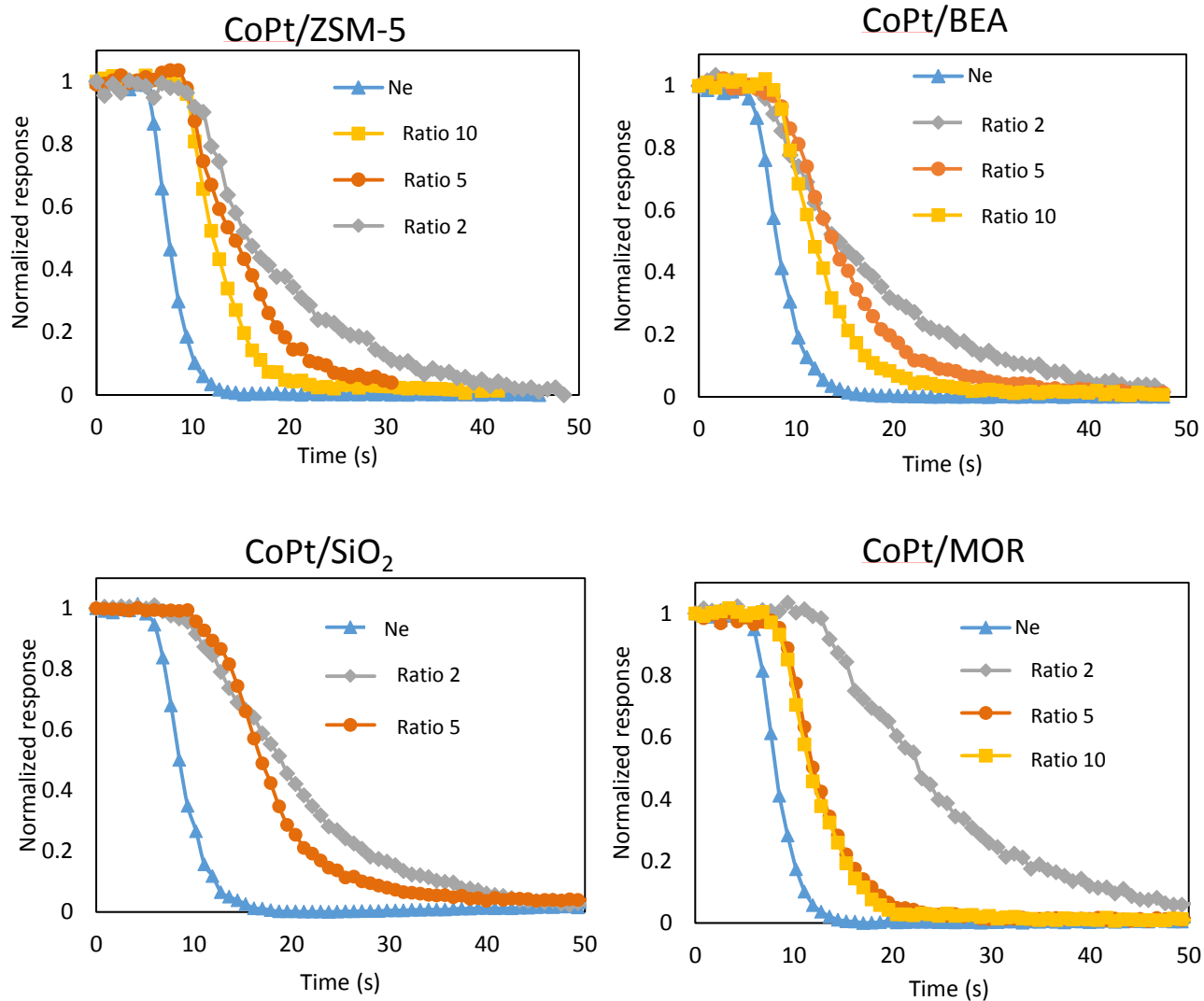
Figure 3.21 Transient curves of inert (Ne) and intermediates leading to CH_4 from the switch of $^{12}CO/H_2/He/Ne$ to $^{13}CO/H_2/He$ in function of ratio feed of H_2/CO (2, 5 and 10). Reaction condition: P ambient, 250 °C, GHSV =13 500 mL/g h, 18 000 mL/g h and 23 850 mL/g h.

The influence of the H_2/CO feed ratio for each sample on the SSITKA rate constant (R_{SSITKA}), number of total sites (N_{total}), including the adsorbed carbon monoxide (N_{CO}) and concentration of CH_4 intermediates (N_{CH4}) is demonstrated in Figure 3.22(a,b).
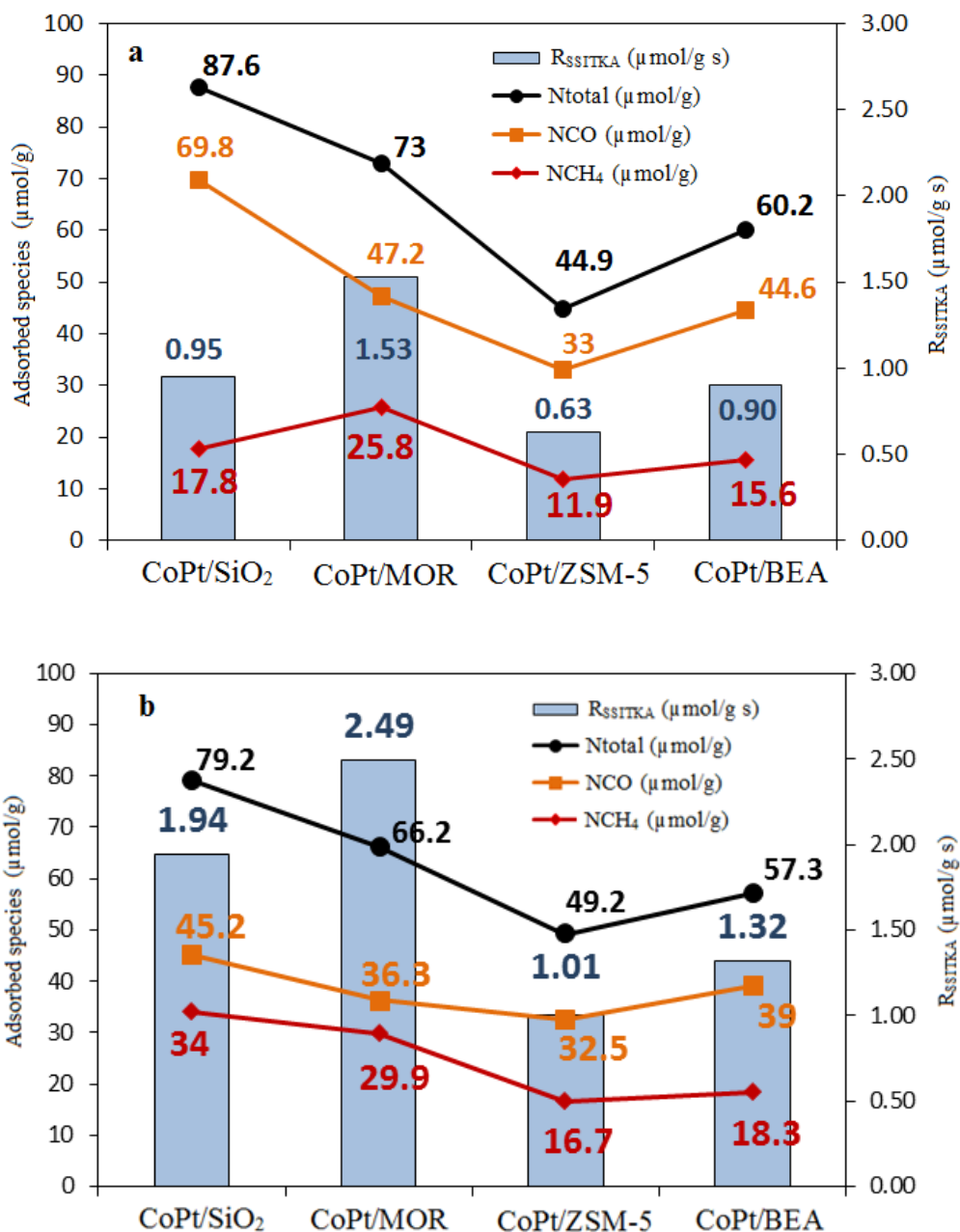
Figure 3.22 Total number of sites ($N_{total} = N_{CO} + N_{CH4}$), number of CO sites (NCO), number of CH$_4$ sites (N_{CH4}) and SSITKA rate constant in ratio feed of H$_2$/CO equal to 2 (a) and 5 (b). Reaction condition: P ambient, 250 °C, GHSV = 13 500 mL/g h, 18 000 mL/g h and 23 850 mL/g h.

The number of molecularly adsorbed carbon monoxide molecules (N_{CO}) decreases with increasing the H$_2$/CO ratio for the cobalt catalysts supported on SiO$_2$, BEA and MOR. This probably occurred due to higher CO conversion (see Table 3.6), unavoidable site

competition between CO and H_2 and irregular distribution of cobalt nanoparticles. For the cobalt catalyst supported on ZSM-5 (microporous structure), N_{CO} value remained constant (33 µmol/g for ratio 2; 32.5 µmol/g for ratio 5 and 33.6 µmol/g for ratio 10) demonstrating in association with the τ_{CO} that CO adsorbs faster for the ZSM-5 support.

Higher amount of CH_x intermediates giving methane on their hydrogenation was observed on the CoPt/MOR catalyst while higher concentration of reversibly adsorbed carbon monoxide molecules (N_{CO}) was detected on CoPt/SiO_2. Interestingly, for cobalt catalyst supported on ZSM-5, N_{CO} and N_{CH4} are smallest between all samples. The MOR demonstrated the highest N_{CH4} among zeolites [50].

Previous DFT modeling results [51] suggest that cobalt molecular adsorption occurs on cobalt terraces, while carbon monoxide dissociation may involve sites and edges in cobalt nanoparticles. Our results suggest that higher cobalt dispersion and in particular higher concentration of the CH_x hydrogenation sites are favorable for higher FT reaction rate. This can possibly explain higher FT reaction rates observed over the catalyst supported by the MOR compared to amorphous silica (Figure 3.23). It can be expected that the zeolite contains more defected cobalt particles compared to silica. The fraction of defects increases with the partial penetration of cobalt nanoparticles in the pores of the MOR and BEA zeolites.
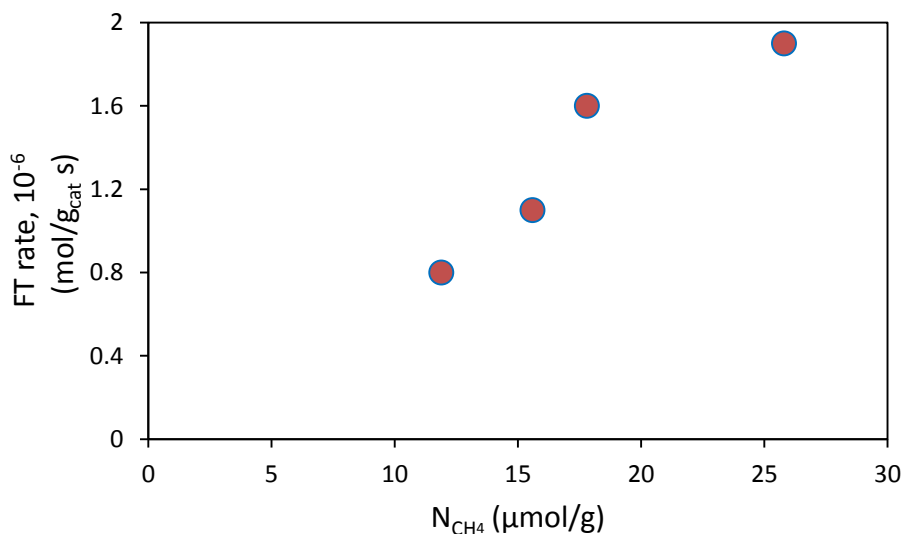
Figure 3.23 Correlation between FT reaction rates measured from steady state experiments and concentration of CH_4 intermediates evaluated from SSITKA.

The trend obtained in this work in relation to N_{CO}, N_{CH4} and R_{SSITKA} for the zeolite supports is consistent with their distinct porous structure. According to the characterization analysis of Subramanian et al. [16], an increase in the size of the zeolite pore causes an increase in the amount of cobalt located inside of the pores. Since the channel diameters of BEA and MOR are larger than for ZSM-5, this leads to the fact that the pores of ZSM-5 present a smaller amount of cobalt available for the reaction, affecting negatively the CO conversion and SSITKA kinetic parameters such N_{CH4} and N_{CO}. Previous report [18, 44] established a correlation between the number of intermediates leading to methane with the pore size of the catalysts. SSITKA experiments demonstrated larger number of CH_x intermediates in the catalysts with medium pore size relative to the catalysts with smaller pore size.

Images of transmission electron microscopy (TEM) presented on Figure 3.24 demonstrate rather different distribution of cobalt nanoparticles in silica and zeolites. For example, in cobalt catalyst supported on ZSM-5, the polycrystalline zeolite particles are covered by large agglomerates of cobalt nanoparticles with sizes between 100–200 nm. Therefore, there is preferential cobalt localization on the external surface of ZSM-5. The TEM images of cobalt catalyst supported on MOR demonstrated a significantly higher incorporation of cobalt nanoparticles in the zeolite crystallites. Even though, some fraction of cobalt nanoparticles was also observed on the surface of the zeolite crystals. TEM images of cobalt catalyst on BEA displayed cobalt inside of zeolite crystals.

CoPt/SiO$_2$ **CoPt/ZSM-5**

CoPt/MOR   **CoPt/BEA**
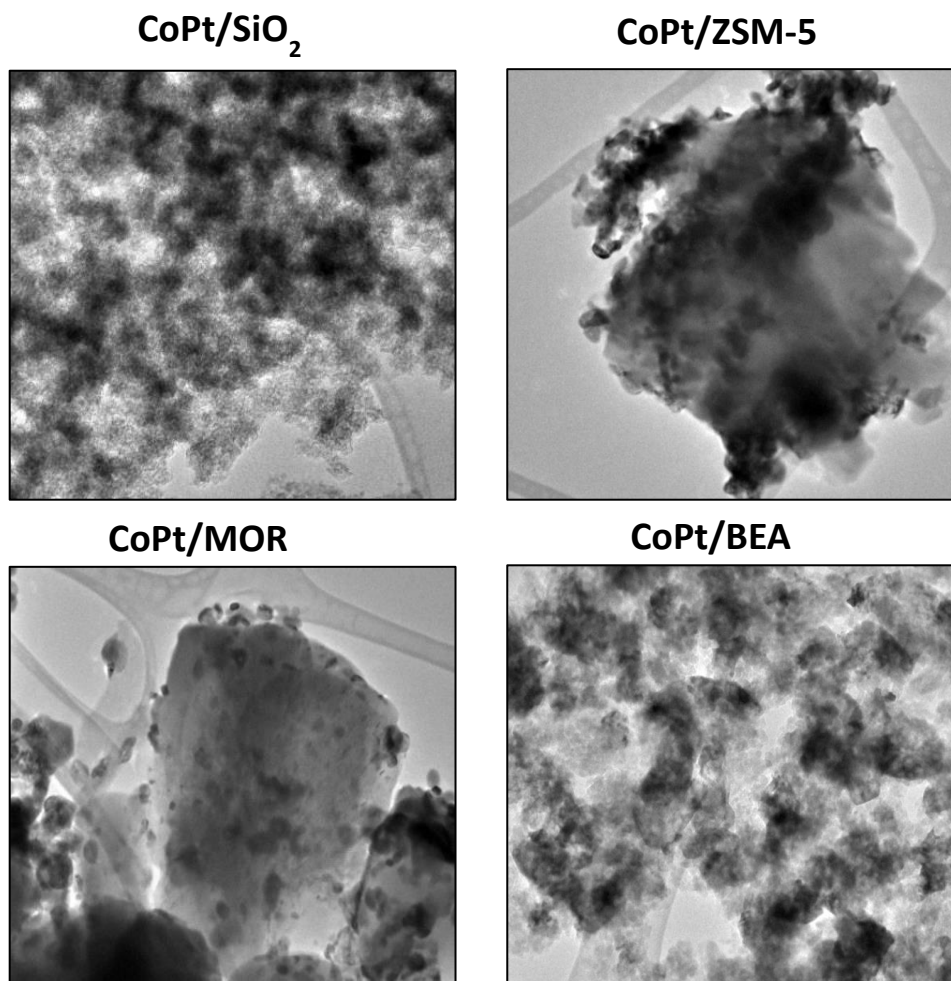
Figure 3.24 TEM image of cobalt based catalysts.

The low activity of cobalt catalyst supported on ZSM-5 was attributed to the preferential localization of cobalt on the outer surface of the zeolite and low concentration of active sites because of poor cobalt dispersion. The long lifetime of the CH$_x$ intermediates (τ_{CH4}) also contributed for the lower activity of CoPt/ZSM-5 zeolite. A more homogeneous distribution of cobalt in the CoPt/MOR and CoPt/BEA catalysts results in higher FT reaction rate. Importantly, a higher FT reaction rate measured at the quasi steady state conditions coincides with a higher fraction of CH$_x$ intermediates (see Figure 3.23) and not to the higher concentration of molecularly adsorbed carbon monoxide molecules (N$_{CO}$).

This is consistent with previous reports [52] and indicates that CH_x hydrogenation can be a kinetically relevant step under these conditions.

Subramanian et al. [16], using the same samples for FTS under realistic conditions (high pressure) also observed that catalytic performance was affected strongly by the zeolite used. CoPt/MOR and Co/PtSiO$_2$ showed the highest CO conversion at low and high pressures among all catalysts studied.

Cobalt catalysts supported on silica and on zeolites have shown different selectivity for the C_{12+} hydrocarbons in comparison with the short-chain $C_5 - C_{12}$ paraffins at realistic FTS conditions [16]. The Co/MOR catalyst demonstrated a significantly lower activity in the isomerization of short-chain hydrocarbons probably due to the partial blocking of stronger acid sites by cobalt species in the 1D channels of the MOR pores. In the case of ZSM-5, as already commented and indicated by the SSITKA data, cobalt is located largely on the external surface of the zeolite crystals. Therefore, FTS occurs on the zeolite external surface and that only short-chain hydrocarbons can diffuse and isomerize effectively inside the pores of ZSM-5 zeolite. Because of stronger acidity compared to other zeolites, Co/ZSM-5 exhibited a higher activity towards the isomerization of $C_5 - C_{12}$ hydrocarbons. The trend was different for larger molecules where isomerization activity was a function of hydrocarbon diffusion in the zeolite pores.

N_{CH4}, that is the measure of the concentration of intermediates able to form hydrocarbons, seems to correlate to the product selectivity at high pressure FTS. For example, the number of the CH_x intermediates is higher for Co/MOR and Co/SiO$_2$, followed by Co/BEA and then by Co/ZSM-5. In terms of selectivity, the Co/ZSM-5 presented the lowest C_{12+} selectivity [16], behind Co/SiO$_2$ and Co/MOR with highest values and Co/BEA in the intermediate scale of such comparison.

3.3 Conclusions

A very strong promoting effect of iron catalysts with soldering metals (Bi, Pb) was uncovered in high temperature FTS. The FT rate and light olefin selectivity increase by 5-10 times and up to 60% respectively, compared to the unpromoted catalyst. The Bi- and

Pb-promoted catalysts also provide an opportunity to selectively produce light olefins from syngas with high yields at atmospheric pressure. A combination of transient kinetic methods and catalyst characterization has provided important information about the observed catalytic phenomena. Noticeable migration of Bi and Pb was observed during the catalytic activation and reaction. It was found that the Bi and Pb promoters are localized in a close proximity to the iron carbide nanoparticles and can facilitate CO dissociation by O removal, which results in modification of Bi and Pb oxidation state. TEM-EDX mapping clearly showed migration the Bi and Pb and preferential localization (decoration) of iron carbide species by the promoter in the catalysts exposed to FT reaction conditions. These results provide efficient strategy for the design of extremely active and selective catalysts for direct synthesis of light olefins from syngas and elucidates the role on the promoters in this reaction.

SSITKA has provided important information about the number of active sites and their intrinsic activity for cobalt catalysts supported on silica and zeolites. Under CO hydrogenation conditions, the total number of sites was higher for cobalt supported on silica compared to the zeolites. The rise of hydrogen partial pressure resulted in a decline of surface residence time of CH_4 and an increase in the concentration of surface intermediates giving methane on hydrogenation (N_{CH4}). The FT reaction rate correlated with the N_{CH4} concentration.

References

1. Galvis, H. M. T.; Koeken, A. C. J.; Bitter, J. H.; Davidian, T.; Ruitenbeek, M.; Dugulan, A. I.; de Jong, K. P., *Catalysis today* **2013,** *215*, 95-102.
2. Davis, B. H., *Industrial & Engineering Chemistry Research* **2007,** *46* (26), 8938-8945.
3. Lohitharn, N.; Goodwin Jr, J. G., *Journal of Catalysis* **2008,** *260* (1), 7-16.
4. Diehl, F.; Khodakov, A. Y., *Oil & Gas Science and Technology-Revue de l'IFP* **2009,** *64* (1), 11-24.
5. Storsæter, S.; Borg, Ø.; Blekkan, E. A.; Holmen, A., *Journal of Catalysis* **2005,** *231* (2), 405-419.
6. Jacobs, G.; Das, T. K.; Zhang, Y.; Li, J.; Racoillet, G.; Davis, B. H., *Applied Catalysis A: General* **2002,** *233* (1), 263-281.
7. Tsubaki, N.; Sun, S.; Fujimoto, K., *Journal of Catalysis* **2001,** *199* (2), 236-246.
8. Chu, W.; Chernavskii, P. A.; Gengembre, L.; Pankina, G. A.; Fongarland, P.; Khodakov, A. Y., *Journal of Catalysis* **2007,** *252* (2), 215-230.
9. Schanke, D.; Vada, S.; Blekkan, E. A.; Hilmen, A. M.; Hoff, A.; Holmen, A., *Journal of Catalysis* **1995,** *156* (1), 85-95.
10. Batley, G. E.; Ekstrom, A.; Johnson, D. A., *Journal of Catalysis* **1974,** *34* (3), 368-375.
11. Surisetty, V. R.; Dalai, A. K.; Kozinski, J., *Industrial & Engineering Chemistry Research* **2010,** *49* (15), 6956-6963.
12. Gardezi, S. A.; Landrigan, L.; Joseph, B.; Wolan, J. T., *Industrial & Engineering Chemistry Research* **2011,** *51* (4), 1703-1712.
13. Fu, T.; Li, Z., *Chemical Engineering Science* **2015,** *135*, 3-20.
14. Bai, S.; Huang, C.; Lv, J.; Li, Z., *Catalysis Communications* **2012,** *22*, 24-27.
15. Dinse, A.; Aigner, M.; Ulbrich, M.; Johnson, G. R.; Bell, A. T., *Journal of catalysis* **2012,** *288*, 104-114.
16. Subramanian, V.; Zholobenko, V. L.; Cheng, K.; Lancelot, C.; Heyte, S.; Thuriot, J.; Paul, S.; Ordomsky, V. V.; Khodakov, A. Y., *ChemCatChem* **2016,** *8* (2), 380-389.
17. Kang, J.; Cheng, K.; Zhang, L.; Zhang, Q.; Ding, J.; Hua, W.; Lou, Y.; Zhai, Q.; Wang, Y., *Angewandte Chemie* **2011,** *123* (22), 5306-5309.
18. Rane, S.; Borg, Ø.; Yang, J.; Rytter, E.; Holmen, A., *Applied Catalysis A: General* **2010,** *388* (1–2), 160-167.
19. Phan, X. K.; Yang, J.; Bakhtiary-Davijnay, H.; Myrstad, R.; Venvik, H. J.; Holmen, A., *Catalysis letters* **2011,** *141* (12), 1739-1745.
20. Frøseth, V.; Storsæter, S.; Borg, Ø.; Blekkan, E. A.; Rønning, M.; Holmen, A., *Applied Catalysis A: General* **2005,** *289* (1), 10-15.
21. Hanssen, K. F.; Blekkan, E. A.; Schanke, D.; Holmen, A.; Froment, G. F.; Waugh, K. C., *Stud. Surf. Sci. Catal.* **1997,** *109*, 193.
22. Govender, N. S.; Botes, F. G.; de Croon, M. H. J. M.; Schouten, J. C., *Journal of Catalysis* **2008,** *260* (2), 254-261.
23. Pham, T. H.; Duan, X.; Qian, G.; Zhou, X.; Chen, D., *The Journal of Physical Chemistry C* **2014,** *118* (19), 10170-10176.
24. Torres Galvis, H. M.; de Jong, K. P., *ACS catalysis* **2013,** *3* (9), 2130-2149.
25. Xie, J.; Torres Galvis, H. M.; Koeken, A. C. J.; Kirilin, A.; Dugulan, A. I.; Ruitenbeek, M.; de Jong, K. P., *ACS catalysis* **2016,** *6* (6), 4017-4024.
26. Cheng, Y.; Lin, J.; Xu, K.; Wang, H.; Yao, X.; Pei, Y.; Yan, S.; Qiao, M.; Zong, B., *ACS Catalysis* **2015,** *6* (1), 389-399.
27. Yang, J.; Ma, W.; Chen, D.; Holmen, A.; Davis, B. H., *Applied Catalysis A: General* **2014,** *470* (0), 250-260.

28.   Bukur, D. B.; Mukesh, D.; Patel, S. A., *Industrial & engineering chemistry research* **1990,** *29* (2), 194-204.

29.   Post, M. F. M.; Van't Hoog, A. C.; Minderhoud, J. K.; Sie, S. T., *AIChE Journal* **1989,** *35* (7), 1107-1114.

30.   Nowicki, L.; Ledakowicz, S.; Bukur, D. B., *Chemical engineering science* **2001,** *56* (3), 1175-1180.

31.   Dictor, R. A.; Bell, A. T., *Journal of Catalysis* **1986,** *97* (1), 121-136.

32.   Pansanga, K.; Lohitharn, N.; Chien, A. C. Y.; Lotero, E.; Panpranot, J.; Praserthdam, P.; Goodwin, J. G., *Applied Catalysis A: General* **2007,** *332* (1), 130-137.

33.   Galvis, H. M. T.; Bitter, J. H.; Khare, C. B.; Ruitenbeek, M.; Dugulan, A. I.; de Jong, K. P., *Science* **2012,** *335* (6070), 835-838.

34.   Yang, J.; Ma, W.; Chen, D.; Holmen, A.; Davis, B. H., *Applied Catalysis A: General* **2014,** *470*, 250-260.

35.   Ordomsky, V. V.; Legras, B.; Cheng, K.; Paul, S.; Khodakov, A. Y., *Catalysis Science & Technology* **2015,** *5* (3), 1433-1437.

36.   Gracia, J. M.; Prinsloo, F. F.; Niemantsverdriet, J. W., *Catalysis letters* **2009,** *133* (3-4), 257.

37.   Ozbek, M. O.; Niemantsverdriet, J. W. H., *Journal of Catalysis* **2014,** *317*, 158-166.

38.   Legras, B.; Ordomsky, V. V.; Dujardin, C.; Virginie, M.; Khodakov, A. Y., *ACS Catalysis* **2014,** *4* (8), 2785-2791.

39.   Carvalho, A.; Ordomsky, V. V.; Luo, Y.; Marinova, M.; Muniz, A. R.; Marcilio, N. R.; Khodakov, A. Y., *Journal of Catalysis* **2016,** *344*, 669-679.

40.   Ordomsky, V. V.; Luo, Y.; Gu, B.; Carvalho, A.; Chernavskii, P. A.; Cheng, K.; Khodakov, A. Y., *ACS Catalysis* **2017**.

41.   Jongsomjit, B.; Panpranot, J.; Goodwin, J. G., *Journal of Catalysis* **2001,** *204* (1), 98-109.

42.   Kogelbauer, A.; Goodwin Jr, J. G.; Oukaci, R., *Journal of Catalysis* **1996,** *160* (1), 125-133.

43.   den Breejen, J. P.; Frey, A. M.; Yang, J.; Holmen, A.; van Schooneveld, M. M.; de Groot, F. M. F.; Stephan, O.; Bitter, J. H.; de Jong, K. P., *Topics in catalysis* **2011,** *54* (13-15), 768.

44.   Ledesma, C.; Yang, J.; Chen, D.; Holmen, A., *ACS Catalysis* **2014,** *4* (12), 4527-4547.

45.   Enger, B. C.; Frøseth, V.; Yang, J.; Rytter, E.; Holmen, A., *Journal of Catalysis* **2013,** *297* (0), 187-192.

46.   Yang, J.; Frøseth, V.; Chen, D.; Holmen, A., *Surface Science* **2016,** *648*, 67-73.

47.   Zhang, X.-Q.; van Santen, R. A.; Hensen, E. J. M., *ACS Catalysis* **2014,** *5* (2), 596-601.

48.   Frøseth, V.; Holmen, A., *Topics in Catalysis* **2007,** *45* (1), 45.

49.   Panpranot, J.; Goodwin, J. G.; Sayari, A., *Journal of Catalysis* **2002,** *211* (2), 530-539.

50.   Bajusz, I. G.; Goodwin, J. G., *J. Catal.* **1997,** *169*, 157.

51.   Shetty, S.; Jansen, A. P. J.; van Santen, R. A., *Journal of the American Chemical Society* **2009,** *131* (36), 12874-12875.

52.   Govender, N. S.; de Croon, M. H. J. M.; Schouten, J. C., *Applied Catalysis A: General* **2010,** *373* (1–2), 81-89.

Chapter 4. New approach for the design of cobalt-zeolite nanocomposites for selective synthesis of isoparaffins in Fischer-Tropsch reaction

4.1 Introduction

A combination of metallic and acidic sites in a single nanocomposite material has been attractive for catalytic application for several decades. Zeolites appear to be among the best candidates for introducing an acidic function because of their high thermal stability, high acidity and unique nanometric porous network. There are a number of catalytic reactions where metal-zeolite composite materials have been efficiently used.

Aromatization of alkanes and methane takes place over bifunctional Ga/ZSM-5 or Zn-ZSM-5 and Mo/H-ZSM-5 catalysts, respectively [1]. Reduction of nitrogen oxides with hydrocarbons and ammonia is catalyzed by bifunctional metal (Cu, Fe, Co, Zn) - zeolite (ZSM-5, MOR, FAU) catalysts [2]. The single-step synthesis of dimethyl ether from syngas requires a Cu/zeolite composite catalyst [3]. Isomerization of long chain alkanes requires both metallic and acidic sites [4]. Metal-zeolite bifunctional catalysts are also used to convert biomass based feedstocks into value-added fine chemicals via combined hydrolysis or liquefaction with hydrogenation [5].

The effect of metal-zeolite composites in comparison for example with mechanical mixtures might be related to the shift of the thermodynamic equilibrium due to rapid conversion of a thermodynamically limited intermediate, increase in the reaction rate or in the selectivity to a specific product. Higher efficiency of metal-

zeolite nanocomposite materials often depends on the distance between metal sites and acid sites [6].

One of the most important applications of metal-zeolite composites is Fischer-Tropsch synthesis (FT) for direct synthesis of short chain isomerized hydrocarbons as gasoline fuel from syngas. FTS over Co, Fe and Ru metallic catalysts leads to the production of broad range of linear hydrocarbons [7]. Subsequent cracking and isomerization over zeolite based catalysts are used in industry nowadays for the fuel manufacturing. A lot of efforts have been dedicated to the development of the catalysts containing both metallic and zeolite phases for the direct one step synthesis of liquid fuels from syngas by combination of FTS and hydrocarbon cracking and isomerization [8-13].

Currently, the main method of preparation of metal-zeolite nanocomposites is impregnation of zeolite with metal salts. In this procedure, a significant part of metal is located on the external surface of zeolite [14, 15]. Mesoporous hierarchical zeolites [8, 9, 10] with encapsulated Co nanoparticles [13] and core-shell catalysts containing FT core and zeolite shell [11, 12] have been also proposed as the most promising solutions. Although the contact between metal and acid sites has been improved in these catalysts in comparison with mechanical mixtures, the yield of gasoline fuel is still not high enough for industrial application.

In this work we suggest a fundamentally new approach for the synthesis of metal-zeolite nanocomposites with selective localization of the metal inside of the zeolite pores. The Keggin-type tungstophosphoric acid $H_3PW_{12}O_{40}$ (HPW) which is one of the most commonly used heteropoly acids with a relatively large anion (around 1.2 nm), strong acidity and high stability [16] was used for metal extraction from the ZSM-5, MOR, and BEA zeolite outer surface.

The ZSM-5, MOR and BEA zeolites have pore sizes in the range of 0.54-0.77 nm, which is significantly smaller than the HPW anion diameter. At the first step, the zeolites were impregnated with cobalt nitrate promoted by a small amount of platinum followed by calcination. Then, the as-prepared materials have been

treated with HPW. Co_3O_4 nanoparticles in this case can be extracted by a strong acid only from the external surface of zeolite due to the large size of acid anion. Thus, the cobalt zeolite composite materials containing cobalt species only inside of the zeolite pores were prepared. These materials have been tested in the synthesis of isomerized hydrocarbons from syngas by Fischer-Tropsch reaction. At different stages of preparation, the zeolite structure and cobalt localization in the nanocomposites were characterized by combination of techniques.

4.2 Results and discussion

4.2.1 Cobalt localization in zeolites

The initial catalysts for further modifications have been prepared by incipient wetness impregnation of H-form of zeolites ZSM-5, MOR and BEA with a similar Si/Al ratio (Table 4.1) by cobalt nitrate with subsequent calcination. The characterization results for the Co/ZSM-5, Co/MOR and Co/BEA materials are shown in Table 4.1 and in Figures 4.1 and 4.2. All prepared catalysts contained about 18 wt. % of Co (Table 4.1) in the form of Co_3O_4.

Table 4.1 Physico-chemical properties of the materials.

Material	Si/Al	Co, wt%	N₂ adsorption		Theoretical volume of Co_3O_4 (cm³)
			S_{BET}^a	V_{mic}^a	
ZSM-5	13	-	305	0.12	-
Co/ZSM-5	-	17.5	281	0.1	-
Co/ZSM-5-HPW	-	8.1	270	0.09	0.016
MOR	8	-	400	0.17	-
Co/MOR	-	18.2	347	0.15	-
Co/MOR-HPW	-	10.3	334	0.13	0.023
BEA	9	-	556	0.15	-
Co/BEA	-	18.7	349	0.08	-
Co/BEA-HPW	-	13.1	382	0.09	0.030

[a] calculated for zeolite part only.

The N$_2$ adsorption–desorption isotherms for the catalysts prepared by impregnation of the parent zeolites are shown in Figure 4.1.
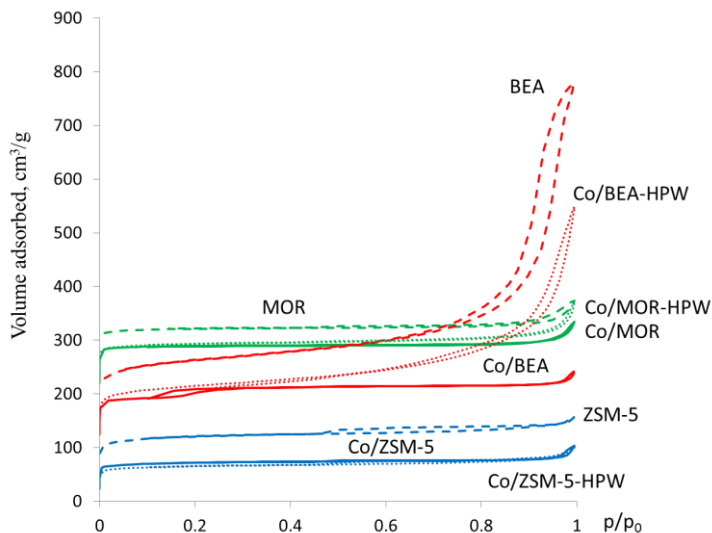
Figure 4.1 Nitrogen adsorption/desorption isotherms obtained at -196.5 °C over the parent zeolites, Co/zeolite catalysts and Co/zeolite catalysts after the HPW treatment.

The ZSM-5 and MOR samples display Type I isotherms with a sharp uptake at a low relative pressure followed by a plateau without a hysteresis. The BEA zeolite exhibits a combination of Type I and IV isotherms with additional hysteresis loop at a high relative pressure (P/P$_0$ larger than 0.8) due to filling of intercrystalline pores. This is a result of agglomeration of small crystallites in BEA zeolite as demonstrated in Figure 4.2.
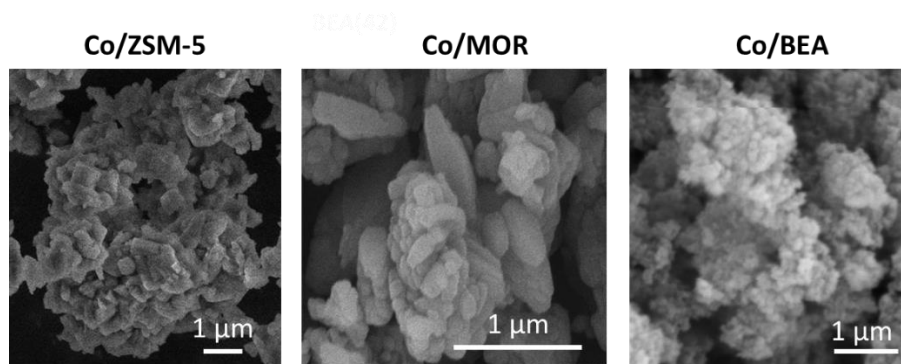
Figure 4.2 SEM images of zeolites.

Impregnation with cobalt results in a downward shift of adsorption isotherms in the case of MOR and ZSM-5 zeolites and transformation of BEA zeolite isotherm to Type I. These changes correspond to decrease in the surface area and micropore volume of zeolite after Co impregnation. This decrease is more pronounced in BEA (around 50%) followed by MOR (approximately 20%) and ZSM-5 (10%). Interestingly, the surface area and pore volume of Co/ZSM-5 only slightly decrease after impregnation relative to the parent zeolite. The 3D pore structure of BEA (pore sizes around 0.76×0.64 nm) is more open than that of MOR (pore sizes around 0.65×0.7 nm; 1 D) and ZSM-5 (pore sizes around 0.55 nm; 3D).

A more significant decrease in the BET surface area and micropore volume of BEA compared to that of ZSM-5 and MOR (Table 4.1) could be assigned, therefore, to much easier diffusion of Co cations into the zeolite pores during the impregnation, which results in a higher Co fraction in the BEA pores.

In the case of ZSM-5, the main fraction of Co oxide seems to be localized on the external surface area. The MOR zeolite with pore size comparable to BEA but 1D structure demonstrates intermediate behavior. The TEM data support these assumptions (Figure 4.3).
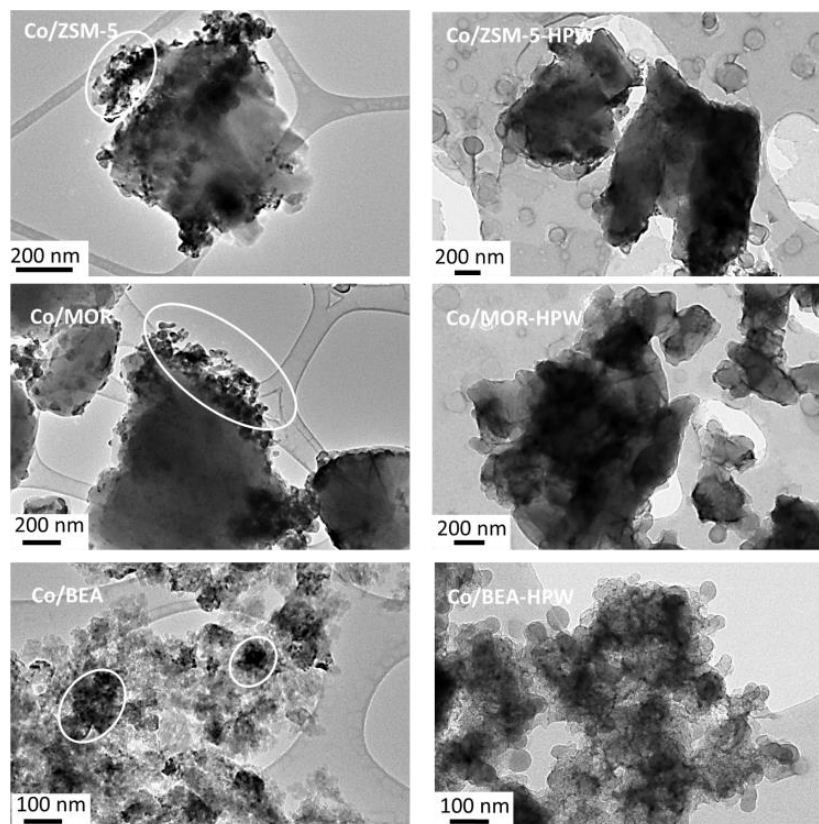
Figure 4.3 TEM image of the catalysts before and after HPW treatment. The agglomerates of Co nanoparticles are indicated by white circle.

In the impregnated calcined Co/ZSM-5, zeolite particles are covered by large agglomerates of Co nanoparticles (100–200 nm). These results are consistent with the preferential Co localization on the external surface of the ZSM-5 zeolite.

The TEM images of Co/MOR demonstrate a significantly higher incorporation of Co in the zeolite crystallites, although some fraction of Co nanoparticles can be observed on the surface of the zeolite crystals.

The TEM images of Co/BEA show that metal does not form a separate phase and most probably uniformly covers zeolite crystals with significant incorporation in the zeolite pores. Relatively uniform cobalt distribution in the BEA zeolite decreases interaction between nanocrystals, which explains disappearance of intercrystalline volume (Figure 4.3, Table 4.1).

4.2.2 Extraction of cobalt species by HPW from outer surface of the zeolites

Treatment of the cobalt zeolite nanocomposites prepared by incipient wetness impregnation with bulky HPW results in dissolution of Co oxide from the surface of zeolite crystals. No effect of this treatment is expected however on the metal oxide nanoparticles located in the zeolite pores. Indeed, because of the large HPW anion diameter, cobalt in the zeolite pore is not accessible for extraction. Cobalt was detected in the solution used for washing the zeolite materials after cobalt extraction with HPW. Interestingly, after 5 cycles of treatment at 90 ℃ with a 5 times excess of HPW to cobalt, no further cobalt extraction was observed from the zeolite.

The ICP analysis showed a significant decrease in the cobalt content in the zeolite (Table 4.1). The most significant decrease was observed for Co/ZSM-5. The resulting Co/ZSM-5-HPW contained twice smaller amount of cobalt in comparison with the parent material. The decrease in cobalt content in the Co/MOR catalyst was slightly smaller than in Co/ZSM-5. In the case of the Co/BEA zeolite, the amount of Co in the catalyst decreased only by 5 wt. % after HPA washing.

The cobalt content in the zeolite after extraction with HPW increases in the row ZSM-5<MOR<BEA which correlates with the increase in the fraction of Co oxide located in the pores according to N_2 adsorption. Thus, it might be considered that cobalt species remaining in the nanocomposites after extraction with HPW were principally located in the zeolite pores. Note that the microporous volume of Co/ZSM-5 and Co/MOR after treatment with HPW almost does not change. This indicates that cobalt oxide is still present inside of the zeolite micropores (Table 4.1, Figure 4.1).

Only in the case of Co/BEA, the micropore volume after the HPW treatment increases which might be explained by opening of the pores of zeolite due to removing large Co_3O_4 nanoparticles located in the pore mouths. Calculation of the volume of cobalt oxide in the catalysts after washing taking into account Co_3O_4 density of 6.1 g/cm^3 gives

0.016 cm^3 to 0.03 cm^3 for the 1 g of zeolite which correlates with the decrease in the microporous volume after cobalt impregnation, as demonstrated in Table 4.1 and Figure 4.4.
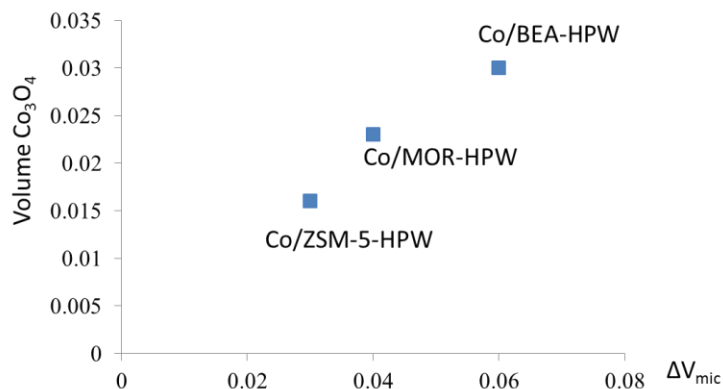
Figure 4.4 Correlation between decrease of the microporous volume of Co/Zeolite-HPW in comparison with parent zeolite and theoretical volume of the introduced Co.

TEM microscopy indicates that treatment of the catalysts with HPW leads to removal of cobalt oxide from the surface of the zeolite crystals for all the zeolites (Figure 4.3).

Figure 4.5 displays the TEM images at high magnification. It is possible to observe dots of Co oxide nanoparticles in the pores of zeolites and absence of Co species on the surface of zeolite crystals.
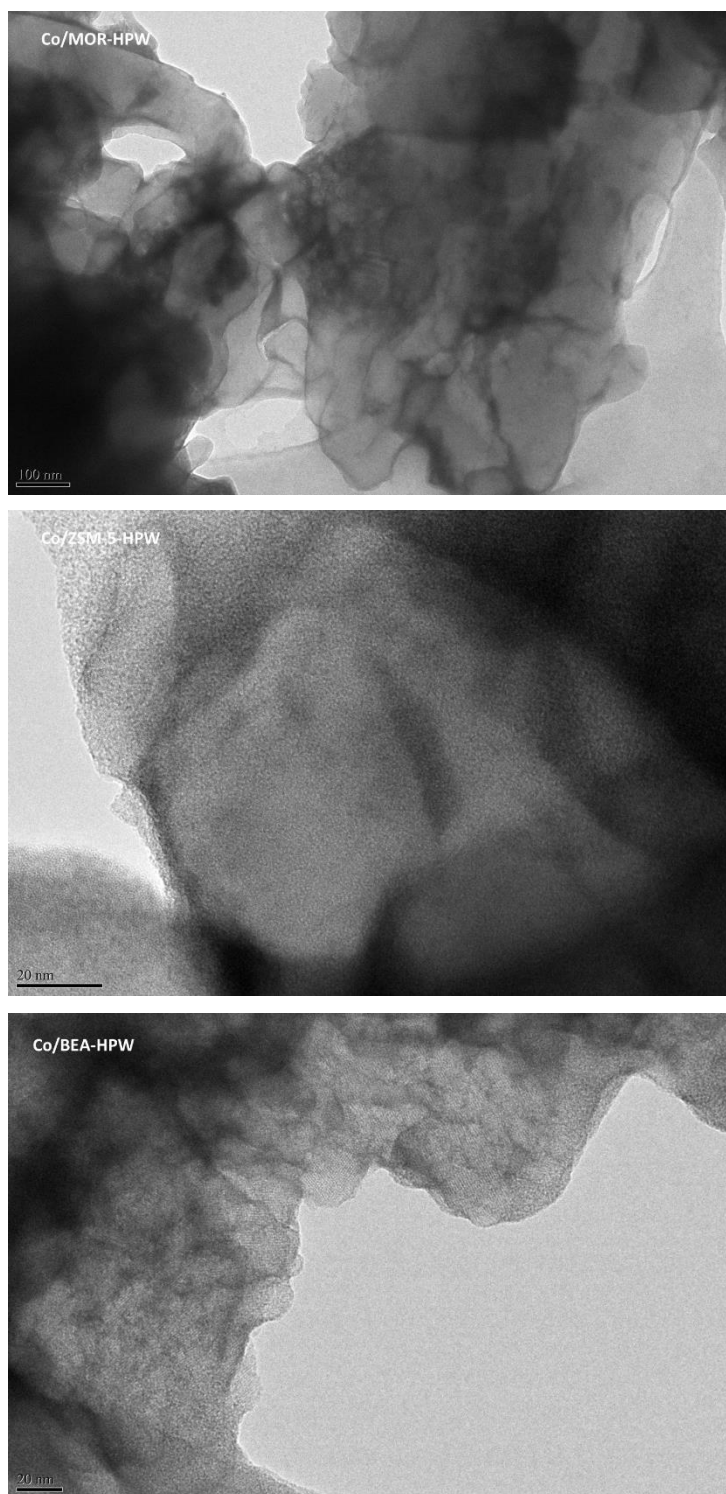
Figure 4.5 TEM image of the catalysts after HPW treatment.

Detailed analysis of Co/BEA-HPW has been performed by high angle annular dark-field (HAADF) STEM analysis. Intensity of the elements at this mode is roughly proportional to the square of the atomic number (Z^2) of the element. Thus, Co atoms ($Z = 58$) appear as bright scattering centers (see Figure 4.6) in the zeolite structure, which consists of only light atoms like Si, Al, O and H.
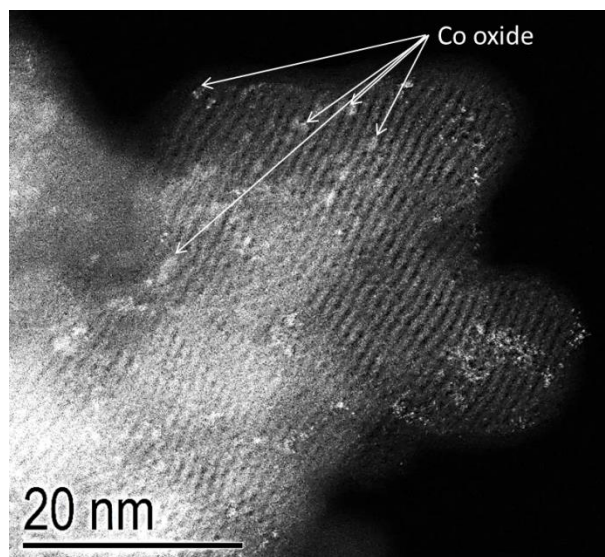
Figure 4.6 HAADF-STEM image of Co/BEA-HPW catalyst.

The image shows the presence of bright intense spots in the pores of zeolite BEA which are attributed to cobalt oxide nanoparticles (Figure 4.6). Interestingly, some of the metal oxide nanoparticles are elongated and arranged along the zeolite channels and some seems to have diameter larger than the diameter of the pore which could be a result of agglomeration of Co oxide species with partial destruction of zeolite structure. In any case, the size of the Co oxide species in any of the directions did not exceed 3 nm. No cobalt species have been observed on the outer surface of zeolite crystals.

It is expected that the properties of the metal species in the pores of zeolites could be significantly different from the properties of metal oxide on the outer surface of zeolite. Indeed, the size of cobalt oxide nanoparticles outside of the pores is at least an order of magnitude larger.

H$_2$-TPR has been used to study the reducibility of the metal species in the catalysts. Figure 4.7 shows that reduction of CoO$_x$ species to metallic Co in the parent catalysts takes place in the range of 200-400 ^{0}C. The TPR results suggest that most of cobalt in zeolites can be reduced at relatively moderate temperatures.
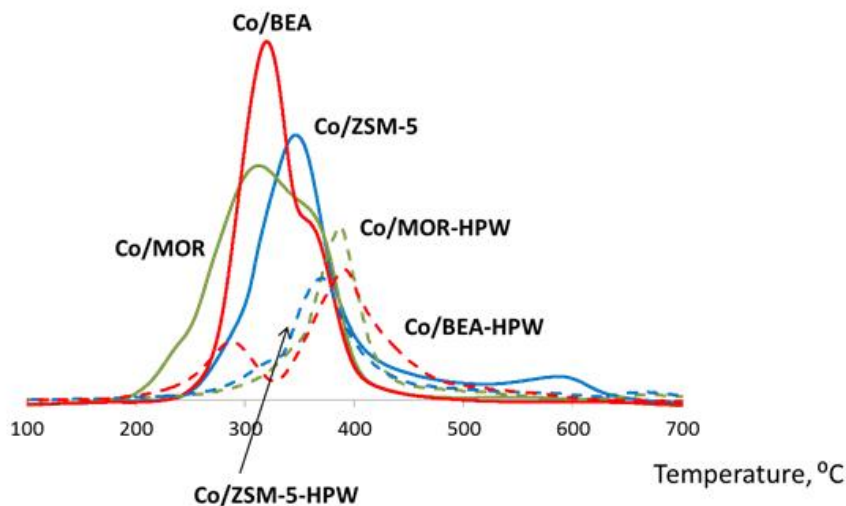
Figure 4.7 TPR reduction curves of Co/zeolite catalysts before and after treatment by HPW.

The treatment of the catalysts with HPW leads to a significant decrease in the TPR peak area due to the lower metal content. In addition, the peaks are shifted to the highest temperature range (approximately 400 ^{0}C) and have similar shapes for all zeolites.

The observed modification of cobalt reducibility correlates with the removal of large oxide nanoparticles from the zeolite outer surface via their extraction with HPW. In agreement with previous reports [17], smaller cobalt oxide particles in zeolites are reduced at higher temperatures compared to larger cobalt oxide particles on the zeolite outer surface. Besides, several other parameters like diffusion limitations of hydrogen into the pores of zeolite and strong interaction with support might have an impact on the reduction behaviour.

The acidity of the catalysts has been characterized by FTIR adsorption of pyridine (Py). The FTIR spectra recorded after Py adsorption on the reduced catalysts are presented in Figure 4.8. Pure zeolite catalysts exhibit characteristic bands at v = 1545 cm^{-1} and

1450 cm^{-1} assigned to the pyridinum ion (PyH^{+}) formed over Brønsted acid sites (BAS) and to Py adsorbed on Lewis acid sites (LAS) (which may include Co^{2+} ions), respectively. Py adsorbed on both the LAS and BAS also displays a band at $v = 1490$ cm^{-1}.
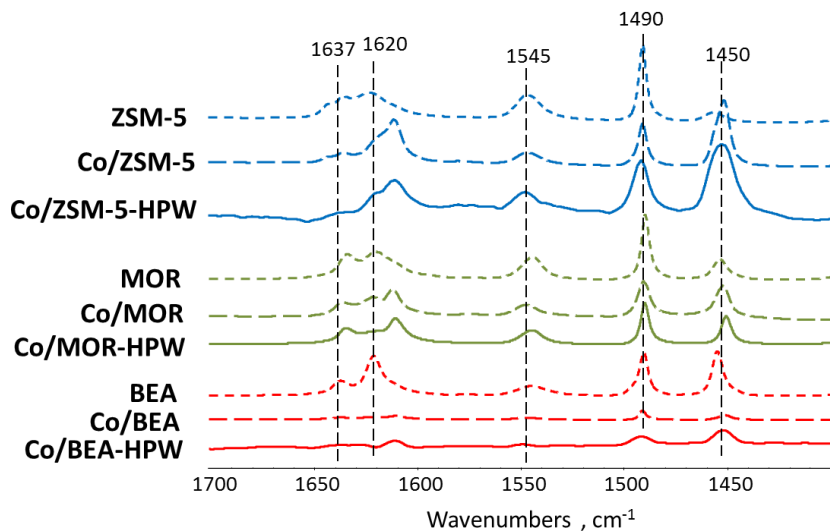
Figure 4.8 FTIR spectra observed after the adsorption of Py.

The concentration of BAS and LAS calculated using the published extinction coefficients for the bands at $v = 1545$ and 1450 cm^{-1} are presented in Table 4.2. The results suggest that impregnation with Co^{2+} cations leads to a significant decrease in the concentration of BAS in the zeolites.

Table 4.2 Concentration of Brønsted sites and Lewis sites of materials.

Material	Acidity (Py adsorption)	
	Brønsted sites (μmol/g)	Lewis sites (μmol/g)
ZSM-5	1090	240
Co/ZSM-5	507	1427
Co/ZSM-5-HPW	794	2100
MOR	921	452
Co/MOR	345	275
Co/MOR-HPW	323	444
BEA	486	834
Co/BEA	88	84
Co/BEA-HPW	56	382

The effect is more pronounced for the BEA zeolite compared to MOR and ZSM-5. The reduced Co/ZSM-5 catalyst retains about 50% of Brønsted acidity, however, the concentration of BAS in Co/BEA is only 18% compared to that of the parent zeolite. This effect might be explained by the ion exchange of the bridging OH group protons for Co^{2+} ions.

The samples treated by HPW demonstrate similar amount of Brønsted acid sites in comparison to non-treated catalysts (Table 4.2 and Figure 4.8). Thus, as expected HPW does not affect internal Brønsted acidity of the catalysts. In contrast, a reversed order is observed for Py adsorption on LAS in the impregnated reduced catalysts.

The number of LAS in ZSM-5 is significantly increased in the presence of Co in comparison with the parent sample. This is a result of Py adsorption over ion exchanged cobalt forming Lewis acid sites. The effect is smaller in the case of the MOR zeolite. At the same time, the parent BEA zeolite already demonstrates significant Lewis acidity because of its defect-rich structure in comparison with ZSM-5 and MOR. Impregnation with Co leads to a sharp decrease in the intensity of the band of Lewis acid sites in the spectrum of Co/BEA.

The weak or negative effect of the introduction of Co on Lewis acidity in BEA and MOR may be due to a more complete Co reduction in these zeolites as confirmed by TPR. The amount of Lewis acid sites in the catalysts washed by HPW is higher in comparison with impregnated catalysts, which might be explained by ion exchange of dissolved Co with external acid sites and unblocking of the pores of zeolite from Co species on the surface in the BEA zeolite.

4.2.3 FTS of isomerized hydrocarbons over cobalt nanoparticles encapsulated in the zeolite pores

The cobalt zeolite nanocomposites with different localization of cobalt species were evaluated as catalysts in FTS. There might be several effects on the FT catalytic performance from the presence of metal nanoparticles only inside of the zeolite pores. First, the size of cobalt nanoparticles inside of the pores of zeolite should be smaller or

comparable to the zeolite micropores. According to earlier studies [18, 19], the decrease in the size of Co nanoparticles leads to lower intrinsic activity in FTS and higher methane selectivity. Second, localization of cobalt nanoparticles inside the zeolite pore can facilitate cracking and isomerization of hydrocarbons produced in FTS. Finally, hydrocarbon synthesis on cobalt nanoparticles in the zeolite micropores can introduce the effect of shape selectivity [20].

The parent nanocomposite Co/zeolite catalysts with cobalt species located both inside and outside of the zeolite pores show a rather broad hydrocarbon distribution with a significant fraction of long chain hydrocarbons (Table 4.1).

Earlier studies [15] indicate that both zeolite pore structure and acidity play key roles in the catalytic performance. For the light C_5-C_{12} hydrocarbons, the isomerization activity is mostly a function of the number of strong acid sites. The ZSM-5 zeolite has been shown to have the highest concentration of the strongest Brönsted acid sites compared to the MOR and BEA zeolites [15]. This is why a higher concentration of isoparaffins was observed over Co/ZSM-5, as show in Table 4.3.

Table 4.3 Catalytic properties of materials (Conditions: T = 250 ^{0}C, P = 20 bar, H_2/CO = 2, GHSV = 1.7-5 L/g h).

Material	XCO (%)	CTY (10^{-4} mol/gCo s)	SCH_4 (%)	SC_2-C_4 (%)	SC_5-C_{11} normal (%)	SC_5-C_{11} iso (%)	$SC_{12\geq}$ (%)	Cis o/ Cn
Co/ZSM-5	27	6.8	12	13	6	16	52	2.6
Co/ZSM-5-HPW	14	5.0	28	13	6	32	21	5.3
Co/MOR	40	9.7	9	10	13	6	62	0.5
Co/MOR-HPW	18	4.8	26	11	5	26	32	5.2
Co/BEA	18	4.2	10	14	12	8	56	0.6
Co/BEA-HPW	22	5.5	25	14	7	35	21	5.8

For longer-chain hydrocarbons, because of their slow diffusion, the selectivity to the branched hydrocarbons is mainly influenced by spatial effects such as the pore size and open character of the zeolite pore structure as well as the location of Co species in the zeolite structure. Broad application of mesoporous zeolite materials for the synthesis of isoparaffins supports this assumption [8, 9, 10]. The large-pore zeolites like BEA and MOR exhibit higher selectivity to long chain isoparaffins and a lower selectivity to linear $C_{20}+$ hydrocarbons (Figure 4.9). The selectivity to the long-chain isoparaffins is favored by the proximity between Co metallic species and Brönsted acid sites.
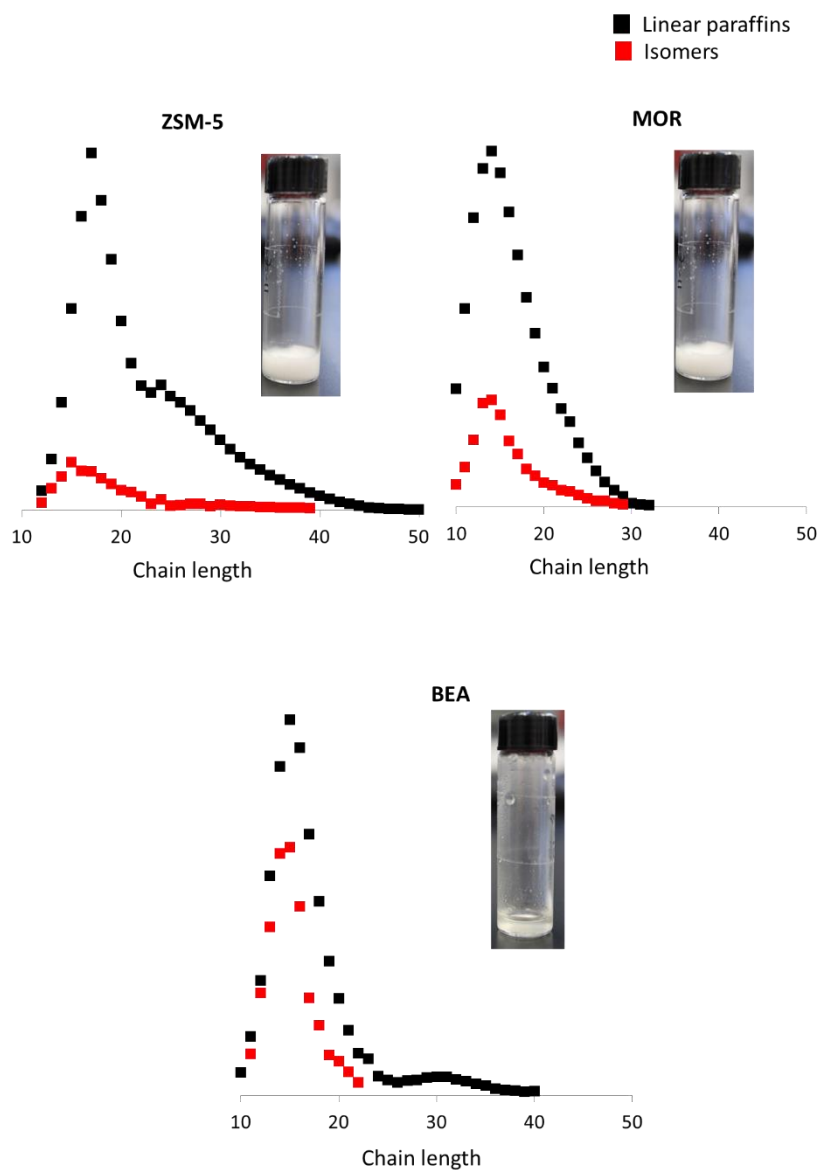
Figure 4.9 Hydrocarbon distribution in liquid products.

The presence of olefins is a key factor for isomerization activity. Earlier studies show that an increase in the isomerization and cracking activity over hydrocracking catalysts (like Pt/USY and Ni/ZSM-5) coincided with increase of the chain length of hydrocarbons [21]. The rate of isomerization is therefore a function of both diffusion and intrinsic catalytic activity.

The catalytic performance of the cobalt zeolite nanocomposites after cobalt extraction from the zeolite outer surface by HPW was rather different in comparison with the parent materials. First, the overall activity significantly decreased after the HPW treatment. This seems to be consistent with the decrease in the overall metal content. Interestingly, the cobalt time yield (CTY) has also significantly decreased (Table 4.3) compared to the parent cobalt zeolite nanocomposite.

It is known that smaller cobalt particles exhibit different behavior in FTS. Kuznetsov [22] and Bartholomew [23] in the pioneering works observed much lower FT turnover frequency on small cobalt nanoparticles. Those observations have been supported with more recent results of the group of de Jong [24]. The decrease in the size smaller than 6 nm resulted in lower FT turnover frequency and higher methane selectivity.

It is interesting to note that CTY over all catalysts after the HPW treatment is very similar (approximately $5 \cdot 10^{-4}$ mol/g_{Co} s) which might be explained by similar structure and size of Co nanoparticles inside of the pores in all zeolites. The slightly higher CTY of Co/BEA-HPW in comparison with the parent catalyst could be explained by easier access of syngas to the cobalt metal sites after the removal of large cobalt nanoparticles from the zeolite outer surface. This is also consistent with the increase in the pore volume of the Co/BEA zeolite after the HPW treatment (Table 4.1, Figure 4.1).

The distribution of hydrocarbons produced on the impregnated samples before and after the HPW treatment is shown in Figure 4.10 and Table 4.3. The selectivities are presented at comparable conversion, which was obtained by the GHSV variation. The results are presented after reaching the steady-state activity of the catalysts. Note that the selectivity to methane significantly increases from about 10% over the parent catalysts to 25% over all the catalysts after the HPW treatment. Higher methane selectivity could be

explained by the presence of smaller Co nanoparticles which have higher intrinsic methanation activity [25]. The selectivity to the C_2-C_4 hydrocarbons is only slightly affected by the HPW treatment.
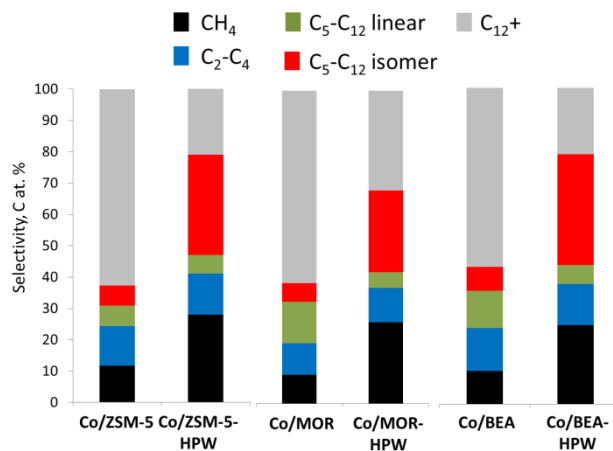
Figure 4.10 Selectivity to hydrocarbons during FTS over Co/zeolite catalysts before and after cobalt extraction with HPW at CO conversion of about 20 %. Conditions: T = 250 ^{0}C, P = 20 bar, H_2/CO = 2, GHSV = 1.7-5 L/g h.

It is interesting to note that the C_2-C_4 hydrocarbon fraction does not contain olefins over the catalysts after HPW treatment in comparison with significant amounts of olefins over catalysts before HPW treatment (Table 4.3). This fact might be explained by participation of the C_2-C_4 olefins in oligomerization over acid sites with formation of isomerized short chain hydrocarbons. According to the literature, the oligomerization of light olefins proceeds at the similar reaction conditions [27].

The most significant differences in the hydrocarbon selectivities have been observed in the middle range (C_5-C_{12}) branched hydrocarbons (Table 4.3 and Figure 4.10). The selectivity to this hydrocarbon fraction increases up to 5 times in comparison with the parent catalysts reaching the 35% selectivity over the Co/BEA-HPW nanocomposite.

The ratio of isoparaffins to linear paraffins in the C_5-C_{12} range, which correlates with the quality of gasoline fuel, also significantly increases in the cobalt zeolite materials containing cobalt nanoparticles only in the zeolite micropores and reaches 5.2-5.8 (Table 4.3). At the same time, the selectivity to long chain hydrocarbons was significantly lower

over the catalysts with cobalt extracted from outer surface in comparison with the parent impregnated catalyst.

Lower selectivity to long chain hydrocarbons can be due to either to fast secondary reactions of the hydrocarbons which form by FT reaction or to the steric effects which restrict chain growth in the zeolite pores. The secondary reactions which occur over the acid sites in the zeolites include hydrocracking and isomerization of the primary hydrocarbons. Cracking of primary FT hydrocarbons should lead to a markedly higher selectivity to light hydrocarbons. Note that the C_2-C_4 selectivities are not really influenced by cobalt extraction from the zeolite outer surface. Low selectivity to light hydrocarbons observed over cobalt zeolite nanocomposites is indicative of low contribution of hydrocracking reactions.

Low impact of hydrocracking reactions have been observed earlier by application of mesoporous zeolites [28]. It is expected that use of a mesoporous zeolite to replace the conventional microporous zeolite may avoid the overcracking because of the improved mass transport, decreasing the selectivities to light alkanes.

The hydrocarbon selectivities in FTS can be also affected by the shape selectivity effects. The effect of shape selectivity in FTS was first uncovered by Fraenkel in 1980 [27]. It has been shown that cobalt metal clusters incorporated inside very small cages of A zeolite (1.1 nm) produce mainly propane and propylene. This effect has been later confirmed over different bifunctional Co−zeolite catalysts [28, 29, 30]. More recently, the effect of shape selectivity was also observed in FTS on Co/SBA-15. A decrease in the SBA-15 pore size from 11 to 5 nm led to a significant decrease in the C_{19+} selectivity from 15% to 4% [31].

It can be expected that the shape selectivity will impose some steric limitations on the hydrocarbon chain growth in FTS, while no influence of steric limitations is expected on the catalyst isomerisation activity. Thus, isomerization over zeolite acid sites and shape selectivity due to the localisation of cobalt nanoparticles in the zeolite pores give main impacts on the hydrocarbon distribution over cobalt zeolite nanocomposites in FTS. The limitation of the chain growth in the pores of zeolite results in a non-linear ASF distribution

over nanocomposite catalysts after cobalt extraction with HPW (Figure 4.11). Similar effect of the restriction of the hydrocarbon chain growth has been observed earlier for FTS in nanoreactors [31].
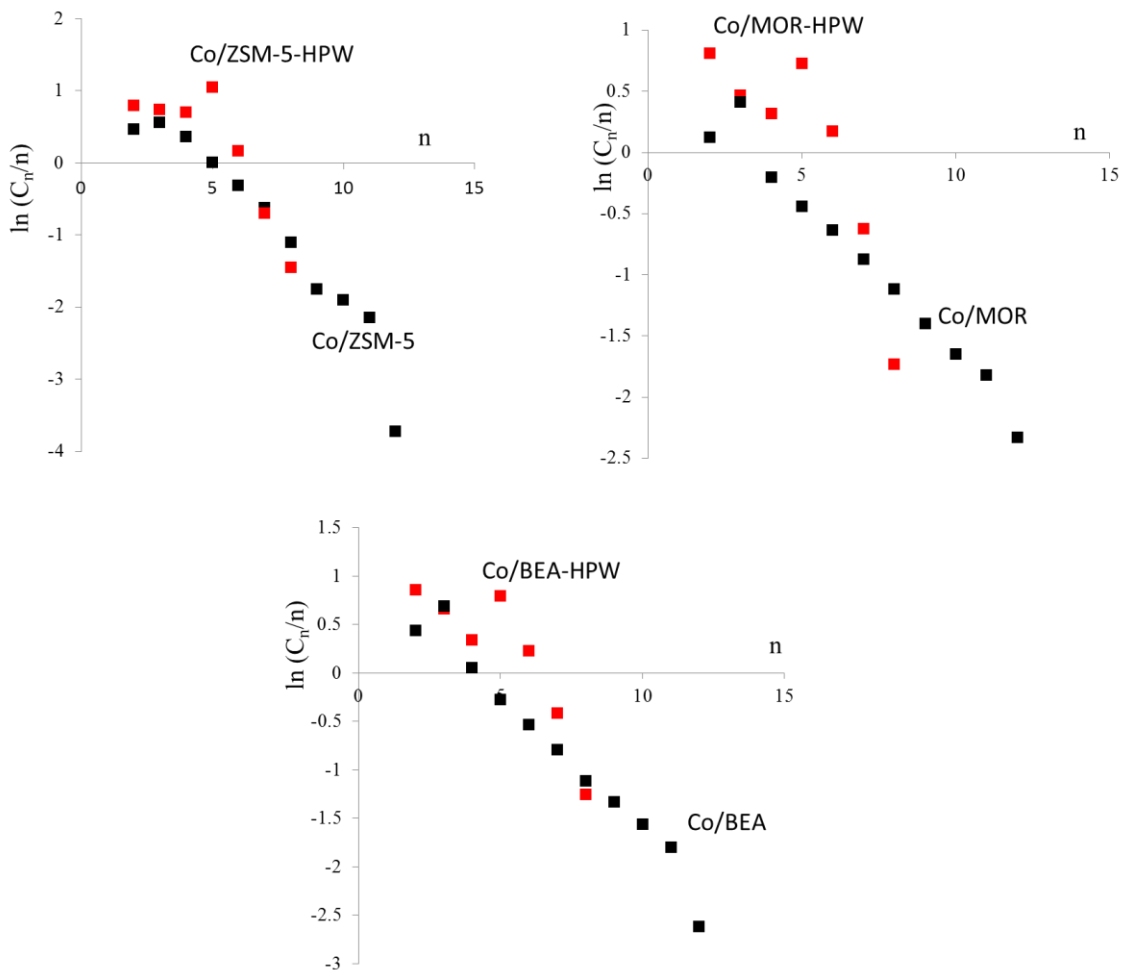
Figure 4.11 Anderson-Schulz-Flory SF distribution of hydrocarbons produced in Fischer-Tropsch synthesis over Co/Zeolite nanocomposites before and after HPW treatment.

It is interesting to note that the nanocomposites containing only cobalt species in the zeolite pores demonstrate almost absence of linear olefins in the products in comparison with non-treated materials (Figure 4.12-4.14).
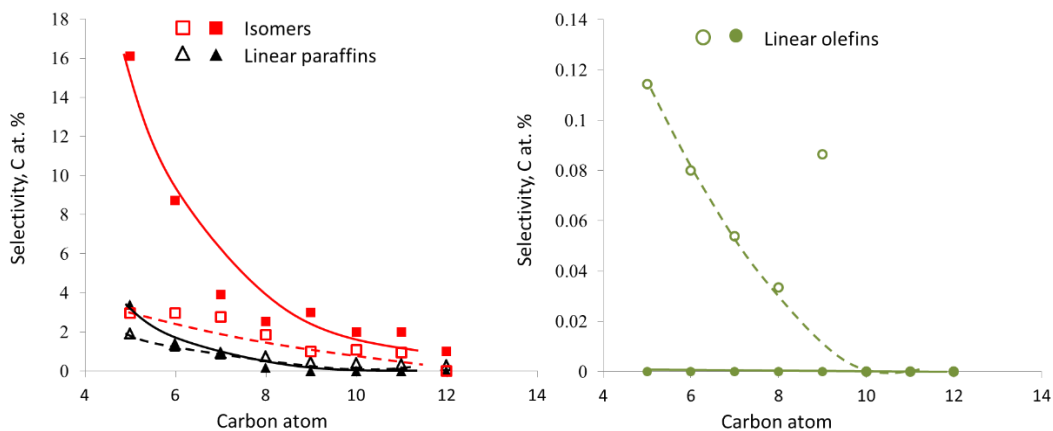
Figure 4.12 Distribution of isomers, linear paraffins and linear olefins depending on the chain length for Co/ZSM-5 (open symbols) and Co/ZSM-5-HPW (filled symbols).
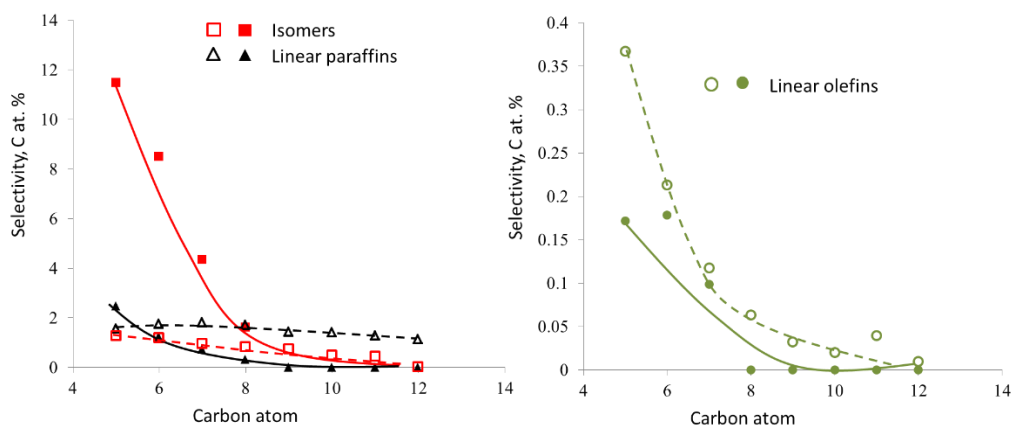
Figure 4.13 Distribution of isomers, linear paraffins and linear olefins depending on the chain length for Co/MOR (open symbols) and Co/MOR-HPW (filled symbols).
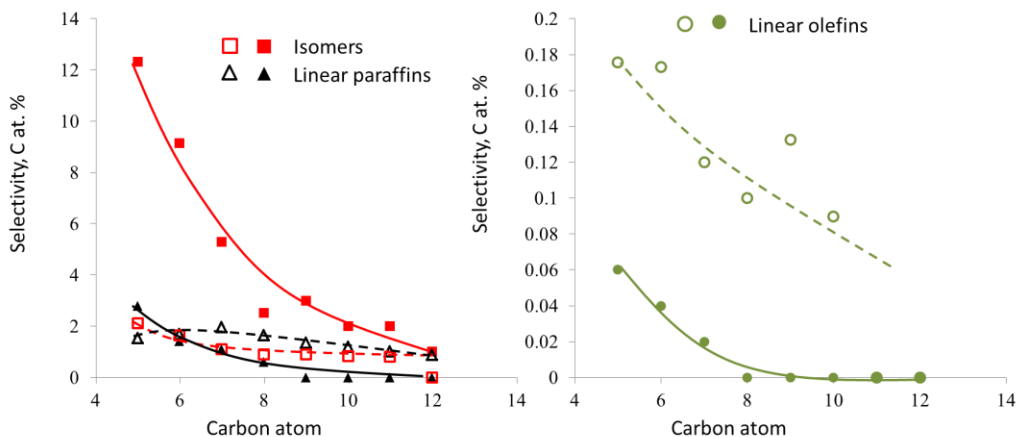
Figure 4.14 Distribution of isomers, linear paraffins and linear olefins depending on the chain length for Co/BEA (open symbols) and Co/BEA-HPW (filled symbols).

Our previous observations [15] indicate that a decrease in the amount of olefins in the products correlate with an increase in the selectivity to isomerized hydrocarbons. Indeed, the reaction mechanism implies protonation of olefins with subsequent isomerization or cracking of carbocations and hydrogenation of the products. Our results suggest that olefin protonation and subsequent isomerization proceed much faster than olefin secondary hydrogenation to linear paraffins.

Development of hierarchical zeolite materials in order to decrease diffusion limitations and overcracking of long chain hydrocarbons in FTS has been a subject of several recent reports. This strategy resulted in the enhanced selectivity to C_5-C_{11} hydrocarbons in FTS. Thus, the C_5-C_{11} hydrocarbon selectivities of about 50-60% have been earlier reached over mesoporous catalysts prepared by the groups of Kapteijn [10] and Wang [28].

Lower fraction of branched hydrocarbons in the reaction products led however, to the low octane number gasoline fuel. The ratio of isoparaffins to n-paraffins observed in FTS over cobalt zeolite catalysts is usually close to unity. Recently Wang and co-workers has reported the isoparaffins to n-paraffins ratio of 3 over Ru catalysts supported by the mesoporous BEA zeolites [8]. The results presented in this work show that the ratio can be increased to 6 over cobalt catalyst prepared by selective extraction of cobalt species from the zeolite outer surface by HPW. The main factor, which significantly increases the

efficiency of isomerization over the nanocomposite catalysts seems to be a proximity between acid and metallic sites. This proximity might be attained by localization of metal nanoparticles inside of the zeolite pores. In this case, a strong synergetic interaction between dehydrogenation/hydrogenation and isomerization functions might be observed with a significant increase in the selectivity to isomerized products.

4.3 Conclusion

The extraction of the cobalt nanoparticles of the external surface of ZSM-5, MOR and BEA zeolite crystals was successfully performed through acid leaching with the phosphotungstic acid ($H_3PW_{12}O_{40}$). The removal of the external cobalt oxide particles led to a decrease in the catalysts activity (on cobalt basis) due to the diffusion limitations and more difficult reduction of the metal inside the zeolite framework. On the other hand, on the washed catalysts, the hydrocarbon selectivity was shifted to products with fewer carbons, i.e. less wax. A higher isomerization degree was observed in particular in the gasoline range (C_5-C_{12}). Thus, by removing the external particles from the zeolite crystals external surface it is possible to improve FT selectivity for the direct production of fuels, i.e. gasoline. The proposed method of selective removal of external nanoparticles demonstrates excellent perspectives for the synthesis of the materials with metal localized only inside of the pores of zeolite. Application of these materials in FTS has demonstrated their high efficiency in the selective synthesis of isomerized hydrocarbons from syngas with the highest ratio of isoparaffins to n-paraffins.

The strategy developed in the present work might be efficiently extended for the synthesis of other metal/oxide-zeolite nanocomposites with selective localization of metal inside of the zeolite pores. The main advantage of this method is its simplicity due to the combination of conventional impregnation and extraction using bulky acids. The proposed methodology can be therefore easily scaled up for the industrial applications. Note however that the extraction using bulky acids might be used only for non-noble metal catalysts. The extraction of noble metals from the zeolite outer surface will require use of other bulky ligands such nitriles or tetraalkylammonium hydroxides. Variation of the extraction agent

_____

diameter might be also used for selective introduction of metal species into mesoporous materials.

References

1 J.A. Biscardi, G.D. Meitzner, E. Iglesia, *J. Catal.*, **1998**, 179, 192-202.

2 Y.J. Li, J.N. Armor, *J. Catal.*, **1994**, 145, 1-9.

3 G. Yang, N. Tsubaki, J. Shamoto, Y. Yoneyama, Y. Zhang, *JACS*, **2010**, 132, 8129-8136.

4 E. Blomsma, J.A. Martens, P.A. Jacobs, *J. Catal.*, **1996**, 159, 323-331.

5 C.-H. Zhou, X. Xia, C.-X. Lin, D.-S. Tong, J. Beltramini, *Chem. Soc. Rev.*, **2011**, 40, 5588-5617.

6 D. Farrusseng, A. Tuel, *New J. Chem.*, **2016**, 40, 3933-3949.

7 A. Y. Khodakov, W. Chu, P. Fongarland, *Chem. Rev.,* **2007**, 107, 1692–1744.

8 K. Cheng, J. Kang, S. Huang, Z. You, Q. Zhang, J. Ding, W. Hua, Y. Lou, W. Deng, Y. Wang, *ACS Catal.,* **2012**, 2, 441 – 449.

9 S. Sartipi, K. Parashar, M. Makkee, J. Gascon, F. Kapteijn, *Catal. Sci. Technol.,* **2013**, 3, 572 – 575

10 S. Sartipi, M. Alberts, M. J. Meijerink, T. C. Keller, J. Perez-Ramirez, J. Gascon, F. Kapteijn, *ChemSusChem,* **2013**, 6, 1646 –1650.

11 G. Yang, C. Xing, W. Hirohama, Y. Jin, C. Zeng, Y. Suehiro, T. Wang, Y. Yoneyama, N. Tsubaki, *Catal. Today*, **2013**, 215, 29– 35.

12 X. Li, J. He, M. Meng, Y. Yoneyama, N. Tsubaki, *J. Catal.*, **2009**, 265, 26–34.

13 N. Kruse, A.G. Machoke, W. Schwieger, R. Güttel, *ChemCatChem,* **2015**, 7(6), 1018-1022.

14 S. Bessel, *Appl. Catal. A,* **1993**, 96, 253-268.

15 V. Subramanian, V.L. Zholobenko, K. Cheng, C. Lancelot, S. Heyte, J. Thuriot, S. Paul, V.V. Ordomsky, A.Y. Khodakov, *ChemCatChem,* **2016**, 8, 380-389.

16 I.V. Kozhevnikov, *Chem. Rev.*, **1998**, 98, 171-198.

17 L.J. Garces, B. Hincapie, R. Zerger, S.L. Suib, *J. Phys. Chem. C*, **2015**, 119, 5484-5490.

18 J.P. den Breejen, J.R.A. Sietsma, H. Friedrich, J.H. Bitter, K.P. de Jong, *J. Catal.*, **2010**, 270, 146−152.

19 J. P. den Breejen, P. B. Radstake, G. L. Bezemer, J. H. Bitter, V. Frøseth, A. Holmen, K. P. de Jong, *JACS*, **2009**, 131, 7197-7203.

20 B. Smit, T.L.M. Maesen, *Nature* **2008**, 451, 671−678.

21 W. Linghu, X. Liu, X. Li, K. Fujimoto, *Catal. Lett.* **2006**, 108, 11-13.

22 E.F. Sousa-Aguiar, F.B. Noronhac, A. Faro, *Catal. Sci. Technol.* **2011**, 1, 698–713.

23 K. Pabst, M.I. González, B. Kraushaar-Czarnetzki, G. Schaub, *Ind. Eng. Chem. Res.* **2013**, 52 (26), 8978–8987.

24 A.S. Lisitsyn, A.V. Golovin, V.L. Kuznetsov, Y.I. Yermakov, *J. Catal.* **1985**, 95, 527–538.

25 R.C. Reuel, C.H. Bartholomew, *J. Catal.* **1984**, 85, 78–88.

26 G.L. Bezemer, J.H. Bitter, H.P.C.E. Kuipers, H. Oosterbeek, J.E. Holewijn, X. Xu, F. Kapteijn, A.J. van Dillen, K.P. de Jong, *J. Am. Chem. Soc*. **2006**, 128, 3956–3964.

27 R.J. Quam, L.A. Green, S.A. Tabak, F.J. Krambeck, *Ind. Eng. Chem. Res.* **1988**, 27, 565-570.

28 K. Cheng, L. Zhang, J. Kang, X. Peng, Q. Zhang, Y. Wang, *Chem. Eur. J.* **2015**, 21, 1928 – 1937.

29 D. Fraenkel, B.C. Gates, *J. Am. Chem. Soc.* **1980**, 102, 478−2480.

30 J. He, Z. Liu, Y. Yoneyama, N. Nishiyama, N. Tsubaki, *Chem. Eur. J*., **2006**, 12, 8296−8304.

31 G. Yang, J. He, Y. Yoneyama, Y. Tan, Y. Han, N. Tsubaki, *Appl. Catal. A*, **2007**, 329, 99−105.

32 V. Subramanian, K. Cheng, C. Lancelot, S. Heyte, S. Paul, S. Moldovan, O. Ersen, M. Marinova, V. V. Ordomsky, A.Y. Khodakov, *ACS Catal*. **2012**, 2, 441−449.

33 M. Bartolini, J. Molina, J. Alvarez, M. Goldwasser, P. Pereira Almao, M.J.P. Zurita, *J. Power Sources* **2015**, 285, 1−11.

Chapter 5. Elucidation of deactivation phenomena in cobalt catalysts for Fischer Tropsch synthesis using SSITKA

5.1 Introduction

Deactivation has been a major limitation for obtaining higher and enduring hydrocarbon productivity [1, 2, 3, 4] on supported cobalt catalysts in FTS. Catalyst deactivation leads to the decrease in catalyst productivity, a loss of the active phase, recurrent startups and shutdowns of the reactor and replacement of relatively expensive catalysts.

Catalyst stability may be optimized by both catalyst structure and reactor operating conditions. The deactivation can be caused by an interplay of several mechanisms, such as cobalt sintering [1, 5, 6, 7] at micro- [8] and nano-scale level, cobalt surface [9] or bulk oxidation [4, 10, 11], carbon deposition [8, 12, 13], catalyst poisoning [14, 15] and carbidization [6].

Considering the effect of catalyst deactivation on FT reaction rate, two different but complementary phenomena can occur. First, catalyst deactivation coincides with the decrease in the total number of active sites for FTS. This effect is more pronounced if all cobalt surface sites have similar intrinsic activity (turnover frequency, TOF). In this case, the drop in the FT reaction rate during deactivation would be proportional to a decrease in the number of cobalt surface sites. Note however, that the catalyst may contain active sites, which may differ significantly in their intrinsic activity. Thus, another possible phenomenon can occur in this case.

Catalyst deactivation can coincide with selective poisoning of the active sites which are the most active and which play the most important role in the catalytic reaction, while the total number of active sites can be only slightly reduced by the deactivation.

The lifetime of FT catalysts can be extended by regeneration and rejuvenation procedures [1, 6, 8, 12, 14, 15]. Regeneration of the catalyst can efficiently restore the activity and should be capable of removing poisons and coke from the surface, as well as redisperse cobalt nanoparticles that have sintered. Diverse regeneration procedures of FT catalysts involve solvent washing, hydrogen treatment, and steam treatment, and oxidative and reductive treatments of spent FT catalysts [16]. Often the regeneration procedures include a combination of the above described processes. One of the possible and most common ways to regenerate FT catalysts is a periodic rejuvenation in hydrogen.

The advantage of the reductive rejuvenation with hydrogen is that this treatment may be performed in situ in fixed bed, slurry or microreactors. The rejuvenation with hydrogen leads to the removal of most of carbon species and reversible poisons (e.g. nitrogen containing compounds) and possibly to the reduction of cobalt which might be partially oxidized in the presence of FT reacting medium (e.g. surface cobalt oxidation) [9]. Much smaller effect of treatment with hydrogen can be expected however on more refractory deposited atomic or polymeric carbon species [16].

In addition to coke, several impurities in syngas may cause irreversible deactivation of FT catalysts. A number of reports [15, 17, 18, 19, 20, 21, 22, 23] have recently addressed the effect of sulphur impurities on the stability of cobalt FT catalysts. Much less attention has been paid to the effects of nitrogen compounds in syngas on the performance and stability of FT catalysts. The reported results however, have been rather contradictory.

Borg et al. [21] studied the catalytic performance of alumina and titania supported catalysts in the presence of 4 ppm of NH_3 in syngas. No effect of ammonia on the catalytic performance was observed. Leviness et al. [24] found that nitrogen compounds produce reversible effect on the catalytic performance of cobalt catalysts. The catalyst activity was restored by treatment in pure hydrogen.

Pendyala et al. [25] studied the effect of addition of ammonia on the performance of platinum promoted cobalt/alumina catalysts. A significant irreversible catalyst deactivation was observed at ammonia levels from 1 to 1200 ppmw. In addition, in the presence of ammonia, the catalyst exhibited lower methane and higher C_{5+} hydrocarbon selectivity, which were attributed to selective poisoning of the methanation sites.

Ma et al. [26] studied the effect of different ammonia containing compounds on the performance of precipitated iron catalysts in a slurry reactor. No deactivation was observed at low ammonia concentrations, while important catalyst deactivation was observed at concentrations of ammonia higher than 400 ppm.

In the work by Sango et al. [27] significant amounts of ammonia (up to 10 wt. %) were added to the syngas feed over unsupported iron catalysts. The catalysts did not shown any noticeable deactivation at the ammonia concentration below 2% wt. In addition to the usual FT products such as hydrocarbons and oxygenates, the reaction yielded long chained aliphatic amines, nitriles and amides, while the selectivities to alcohols, aldehydes and organic acids were much lower in the presence of ammonia.

SSITKA can be particularly useful to identify the origin of the loss of activity and selectivity, because it yields independent information about the number of active sites and also allows measuring their intrinsic activity.

In this chapter, the goal is to elucidate and to characterize the deactivation phenomena occurring with cobalt catalysts during FTS using pure syngas and syngas containing nitrogen compounds. Combining SSITKA with the extensive characterization of deactivated samples yields important insights into the deactivation phenomena and represents an efficient strategy for the design of more stable cobalt catalysts for FTS. The new approach provides an opportunity to clearly identify different deactivation mechanisms as well to determine surface kinetic parameters such as the number of intermediates and their reactivity at different deactivation and rejuvenation steps. The influence of catalyst rejuvenation via the pretreatment with hydrogen on the number of active sites and their kinetic parameters has also been evaluated.

5.2 Results and discussion

5.2.1 CO adsorption

Prior to the catalytic test, the $CoPt/SiO_2$ catalyst was reduced in hydrogen flow of 8 cm^3/min at 400°C. After that, switches between $^{12}CO/He/Ne$ and $^{13}CO/He$ were performed in the absence of catalytic reaction at 100 °C to evaluate the number of CO adsorption sites present in the catalyst (Figure 5.1). No carbon dioxide or hydrocarbon formation was observed under these conditions.
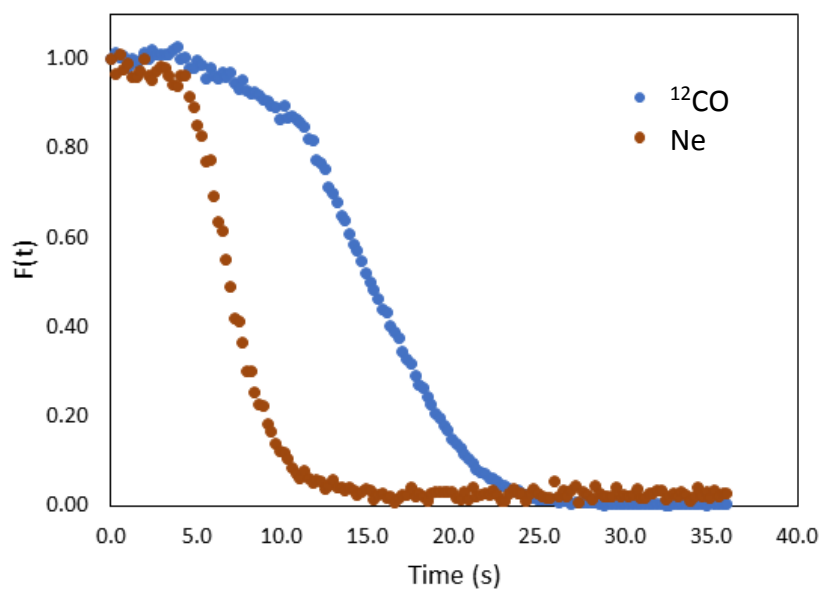
Figure 5.1 Normalized concentrations of ^{12}CO and Ne during switches from $^{12}CO/He/Ne$ to $^{13}CO/He$ at 100 °C.

Carbon monoxide transient response shows a delay relative to neon (Ne) which can be attributed to carbon monoxide adsorption. The observed delay is due to the CO interaction with cobalt active sites. The delay indicates the presence of reversibly adsorbed carbon monoxide molecules on the catalyst surface which are in equilibrium with carbon monoxide in gaseous phase. The transient delay ($\tau_{CO}-\tau_{Ne}$) which represents the average

_____

carbon monoxide residence time on the catalyst surface was calculated from the SSITKA transient curves.

Carbon monoxide adsorption was completely reversible under these conditions (Figure 5.1). Calculation using the results obtained at 100 °C (without the catalytic reaction) gave 107.3 ± 6.8 μmol/g as the number of the adsorption sites present in the catalyst and carbon monoxide surface residence time of 7.7 s.

5.2.2 Catalytic behavior of silica supported cobalt catalyst in carbon monoxide hydrogenation

After reduction (procedure already mentioned in Section 5.2.1), the activated sample was exposed to a steady flow of syngas under FT reaction conditions (GHSV = 10 800 mL/g h, ambient pressure, 250 °C, H_2/CO ratio = 2). Because of higher temperature, the main products of carbon monoxide hydrogenation under these conditions during the whole time of reaction were methane (methane selectivity >60%) and water. The duration of the whole catalytic tests was at least 150 h.

Figure 5.2 shows that the CO conversion decreases as a function of time on stream from 18% to 8%, which is probably assigned to catalyst deactivation. Interestingly, the methane selectivity is not much affected by the conversion and remains high during the entire catalytic test.
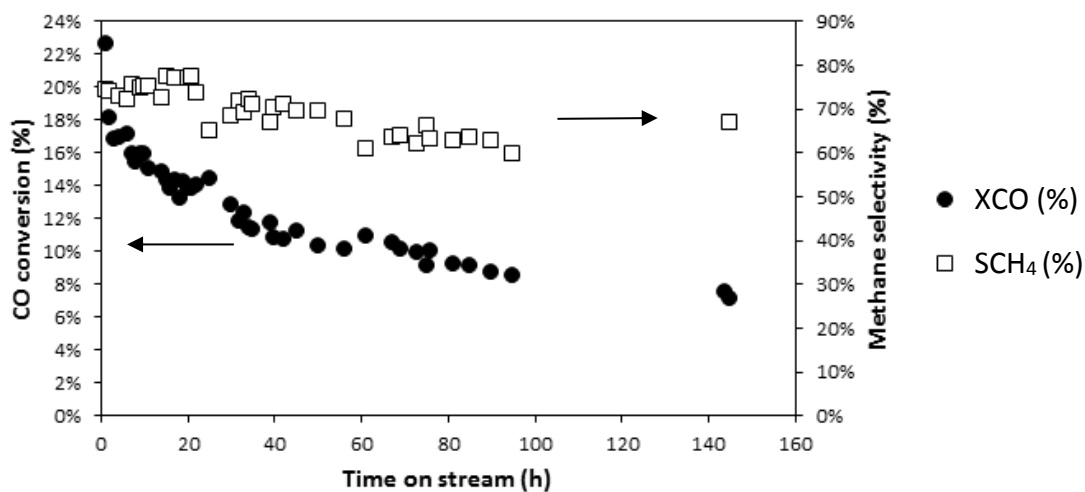
Figure 5.2 CO conversion and methane selectivity as functions of time on stream during FTS under methanation condition (1 atm, 250°C, $H_2/CO = 2$, GHSV = 10 800 mL/g h).

The SSITKA experiments were performed with the catalyst at different times on stream (1 h, 22 h, 40 h and 150 h). The switches between $^{12}CO/H_2/He/Ne$ to $^{13}CO/H_2/He$ were conducted with simultaneous measurements of transient responses of unlabeled and ^{13}C-labelled CO and CH_4. The SSITKA data obtained after different times on stream are shown in Figures 5.3a and b. A delay is observed between response of inert tracer Ne (τ_{Ne}) and ^{12}CO (τ_{CO}) (Figure 5.3a). The information about number of adsorbed species present on the catalyst surface as a function of time and deactivation is given in Table 5.1.

Table 5.1 SSITKA results (P = 1 atm, T = 250 °C, H_2/CO = 2, GHSV = 10 800 mL/g h).

TOS (h)	N_{CO}[a] (μmol/g)	N_{CH4}[a] (μmol/g)	τ_{CO} (s)	τ_{CH4} (s)	XCO	TOF $_{SSITKA}$[b] (s^{-1})	TOF[c] (s^{-1})
1	56.0	39.6	5.2	17.0	18%	0.022	0.013
22	53.4	27.1	4.5	18.8	14%	0.013	0.011
40	51.2	23.2	4.1	22.0	11%	-	-
150	39.4	22.7	3.1	29.2	7%	0.007	0.005

[a] $N_i = \frac{F_{i,out}}{W} \cdot \tau_i$ (Experimental error in the number of active sites equal to 6%).

[b] TOF_{SSITKA} = fractional coverage/surface residence time of CH_x.

Interestingly, the carbon monoxide surface residence time (τ_{CO}) and number of carbon monoxide adsorption sites (N_{CO}) decrease with time on stream (Table 5.1, Figure 5.3a). When the catalyst has been exposed to syngas for a longer time on stream, the delay between Ne and ^{12}CO responses decreases, while the slope of the ^{12}CO transient response curves is not much affected by the reaction time.

Analysis of the SSITKA data suggests a decrease in reversible carbon monoxide adsorption during the reaction. Note that 22 h of the reaction are sufficient for producing a decrease in the number of sites for reversibly adsorbed carbon monoxide. Carbon monoxide residence time also decreases with time on stream (Figure 5.3a). Several deactivation phenomena responsible for these modifications may occur under these reaction conditions (e.g. cobalt sintering, carbon deposition, oxidation etc) [5, 28, 29].

An alternative interpretation of the decrease in surface coverage of CO with the time on stream measured by SSITKA can be due to the formation of inactive CO species irreversibly adsorbed on the metal sites. The effect can be similar to that observed in the WGS reaction on supported Pt catalysts [30] where only part of adsorbed linear CO was considered as an active intermediate in WGS. In contrast to the ^{12}CO isotopic response, the switches between $^{12}CO/H_2/He/Ne$ to $^{13}CO/H_2/He$ produce different effects on the $^{12}CH_4$

transient (Figure 5.3 and Table 5.1). The slope of the $^{12}CH_4$ response becomes flatter with time on stream.
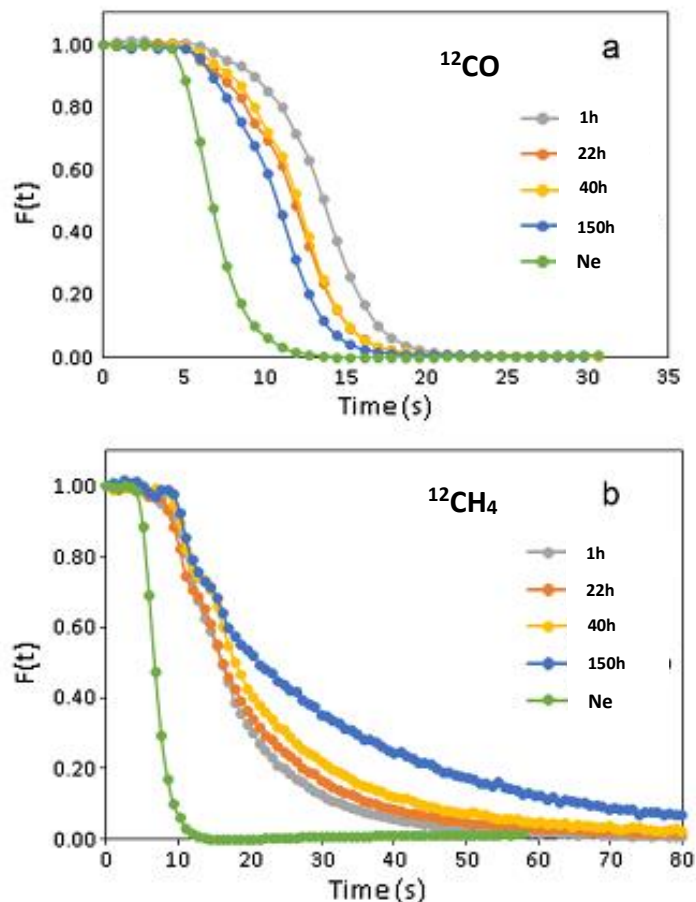
Figure 5.3 ^{12}CO (a) and $^{12}CH_4$ (b) normalized concentrations during switches from $^{12}CO/H_2/He/Ne$ to $^{13}CO/H_2/He$ on CoPt/SiO$_2$ at different times on stream. Reaction conditions: 1 atm, GHSV = 10 800 mL/g h, 250 °C, gas composition 1CO/2H$_2$/5.5He/0.5Ne.

Quantitative analysis of the ^{12}C methane SSITKA responses indicates a decrease in the number of surface intermediates leading to methane under these conditions (Figure 5.3b). Interestingly, for the fresh catalyst after 1 h on stream, the sum of the number of sites of carbon monoxide reversible adsorption and CH$_4$ intermediates measured by SSITKA at the beginning of the reaction is almost equal to the number of sites of reversibly adsorbed carbon monoxide determined by carbon monoxide desorption experiments conducted without reaction at 100 °C. This suggests that carbon monoxide adsorption under the

_____

reaction conditions of FTS may lead either to reversible CO adsorption or to direct or hydrogen-assisted dissociative CO adsorption taking place on cobalt metal sites and leading in turn to CH_4 intermediates.

Most of CO molecules adsorb molecularly on the surface of the cobalt nanoparticles, but some undergo dissociation which can be assisted by hydrogen [28]. The surface residence time (τ_{CH4}) increases with time on stream. This suggests a lower hydrogenation rate of CH_x intermediates in the partially deactivated catalyst. It should also be noted that the decrease in the number of surface CH_x species occurs much faster than that in the number of sites for reversibly adsorbed carbon monoxide (Figure 5.4a,b).
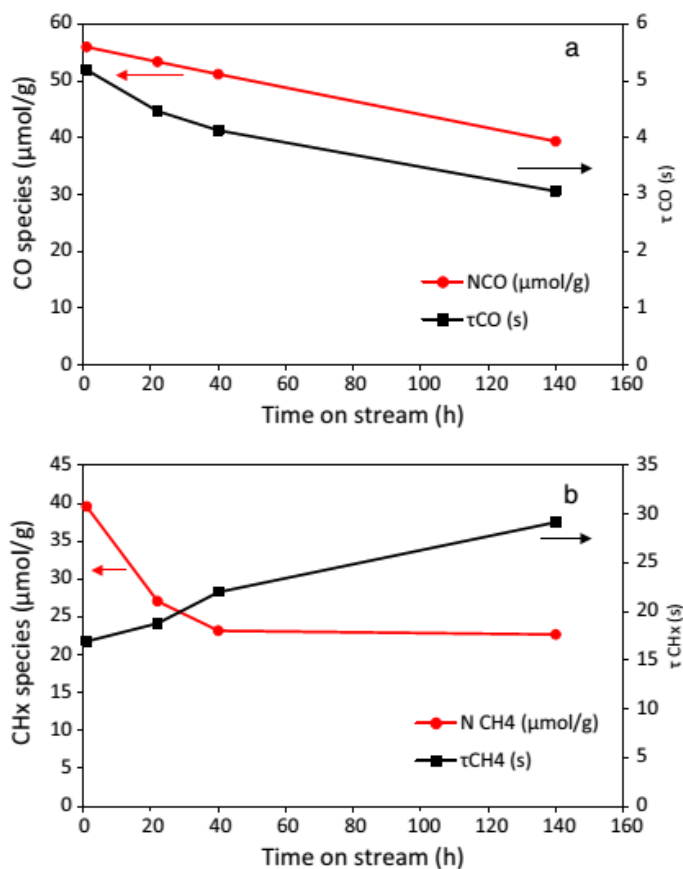
Figure 5.4 Concentration of CO (a) and CH_4 (b) intermediates and their surface residence time versus time on stream.

Thus, catalyst deactivation leads to a decrease in the number of reversibly adsorbed CO molecules and most active CH_4 intermediates. The residence times of CO and CH_4

intermediates are also affected. The residence time for adsorbed molecular CO decreases, while the residence time of CH_4 species increases. This can be interpreted as preferential poisoning of stronger sites of CO molecular adsorption and most active CH_4 methanation sites.

Note that the number of CH_4 intermediates decreases much faster than the number of reversibly adsorbed CO molecules (Figure 5.4). In addition, SSITKA was also indicative of shorter carbon monoxide residence times and longer CH_4 residence times on partially deactivated catalysts. This suggests preferential poisoning of the stronger carbon monoxide adsorption sites and the sites which form the most reactive CH_4 intermediates.

Some decrease in hydrogen coverage of the catalyst surface during the deactivation can also contribute to the increase in the CH_4 residence time. Indeed, it has been previously shown [31] that molecular adsorption of CO on cobalt metal sites usually proceeds without any activation barrier. Thus, the rate establishing equilibrium between adsorbed and gaseous CO molecules is principally affected by the activation energy of CO desorption from the catalyst. Catalyst deactivation results in the decrease in the concentration of the sites on which CO is strongly adsorbed and thus in apparent activation energy of CO desorption.

On the other hand, catalyst deactivation leads to longer residence times of adsorbed CH_4 species. Previous report [32] suggest that hydrogenation of CH_x species can be the rate limiting step under these conditions. The observed increase in the CH_4 surface residence time may therefore indicate a slower rate of methane production over partially deactivated catalysts.

5.2.3 Characterization of spent catalysts

The spent catalyst samples were removed from the reactor at different reaction times and extensively characterized by TEM and TPH-MS. TEM images of the parent sample and counterparts after different times on stream (1 h, 22 h and 150 h) are given in

Figure 5.5. In the sample exposed for 1 h to the reaction conditions, the TEM images display mostly cobalt nanoparticles with a diameter of about 20 nm dispersed on silica support.
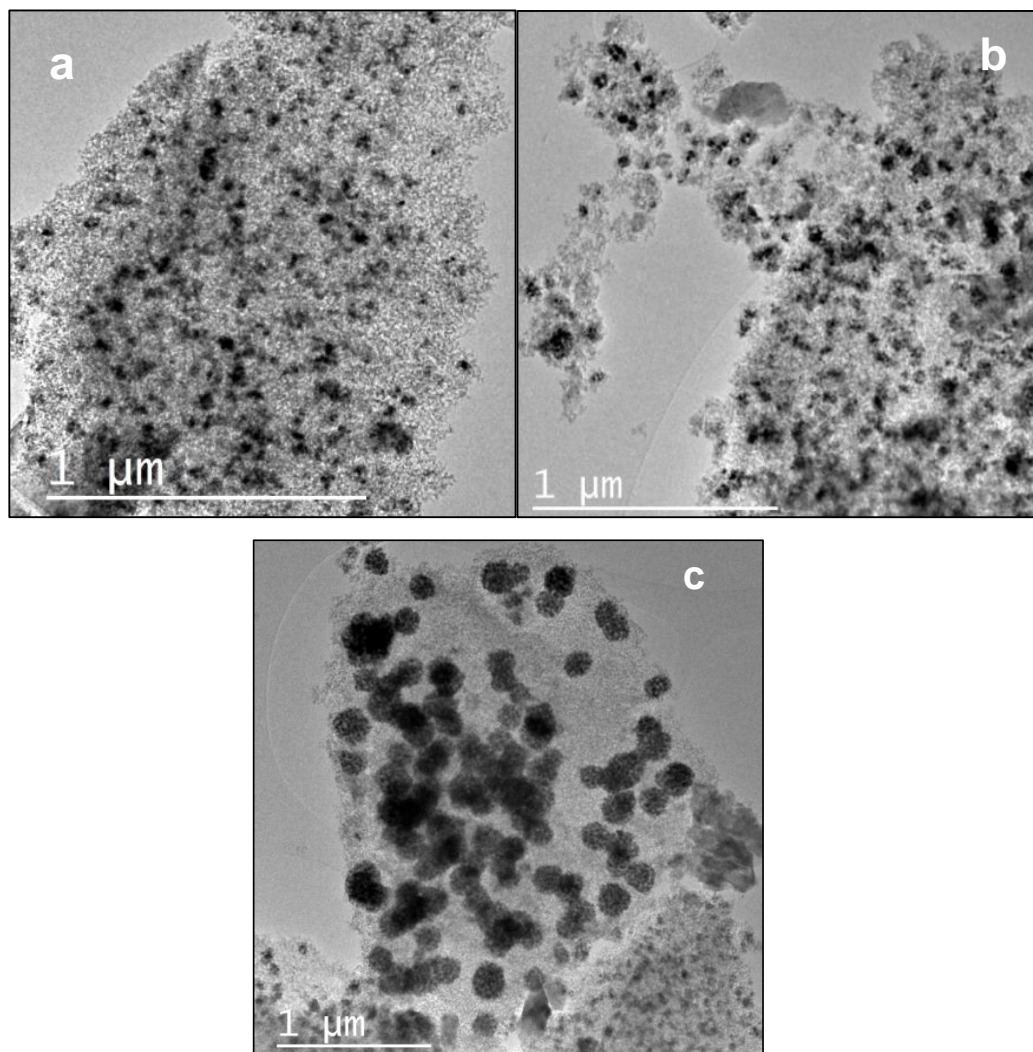
Figure 5.5 TEM images of the CoPt/SiO$_2$ catalyst after different times on stream 1 h (a), 22 h (b), 150 h (c).

The TEM results are consistent with the XRD data of the calcined catalyst, which also suggest a cobalt particle size in the same range. Conducting reaction for 22 h leads only to a slight increase in the apparent cobalt particles size. Previous investigations [5, 6, 7, 33] suggest that cobalt sintering in supported catalysts principally occurs during the initial reaction time. Note that we did not observe any major cobalt sintering during the first 22 h of the reaction. Interestingly, after 150 h of the reaction very large cobalt

agglomerates probably consisting of several individual cobalt nanoparticles were detected in the catalysts.

The silica support texture (average pore size of 10 nm according the Fuji-Silysia website) could be responsible for this large cobalt agglomeration at 150 h, even in low water partial pressure condition. Figure 5.6 shows the cobalt agglomerate size distributions for the catalyst samples after 1 h and 150 h of FT reaction. The whole distribution shifts to larger values after conducting FTS. The average size of agglomerates increases to 130 nm for the catalyst exposed to FT reaction for 150 h. It is expected, however, that the presence of these larger cobalt agglomerates should not significantly affect the FT reaction rate. Previously it was shown [33, 34] that the FT reaction rate on cobalt catalysts is a function of individual cobalt crystallites rather than of larger cobalt nanoparticle agglomerates.
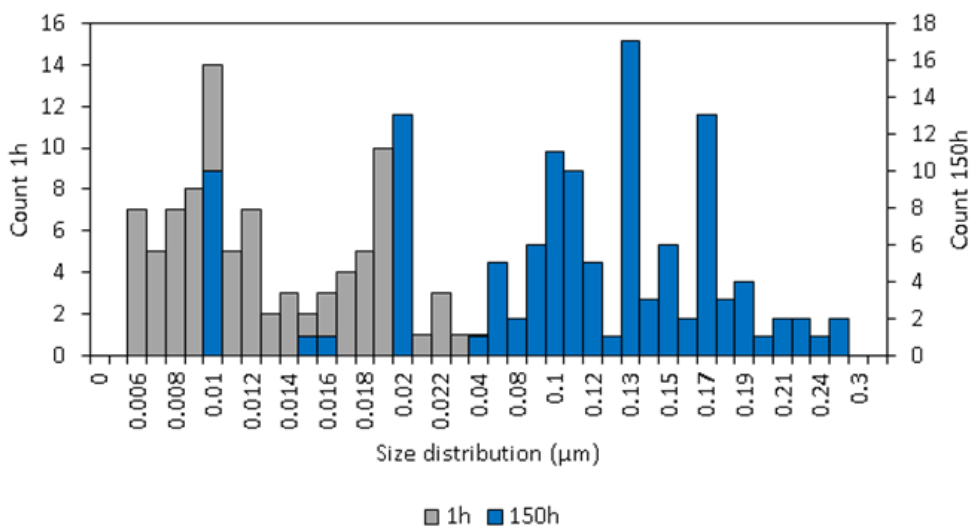
Figure 5.6 Histograms of cobalt agglomerate size distribution after 1 h and 150 h of reaction.

Several correlations are observed in this work between the SSITKA parameters and the structure of spent catalysts. On the one hand, TEM of the spent catalysts was indicative of very slight cobalt sintering occurring under our reaction conditions during the initial reaction time followed by formation of larger cobalt nanoparticle agglomerates at longer time on stream. In agreement with previous reports [33, 35], the formation of larger cobalt

nanoparticle aggregates should not significantly affect the FT reaction rates. Indeed, if the reaction rate was principally affected by the size of cobalt agglomerates, the increase in the size of cobalt agglomerated observed by TEM (from 20 nm to 130 nm) should correspond to almost 6 times the decrease in the FT reaction rate. This decrease, however, did not occur. Some influence of the agglomeration of cobalt nanoparticles on the FT catalytic performance cannot, however, be completely excluded.

Carbon species deposited on the catalyst surface during the FT reaction were investigated by TPH-MS. Figure 5.7 displays curves of methane production during heating of spent silica supported cobalt catalysts in hydrogen.
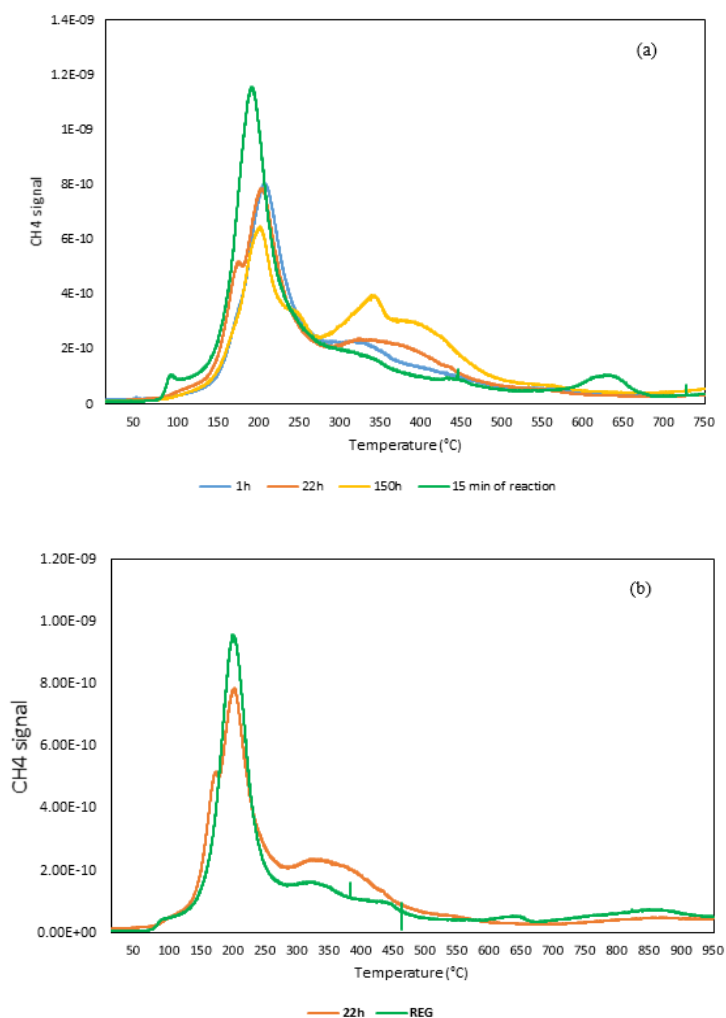
Figure 5.7 TPH MS profiles (m/e = 15) measured on the CoPt/SiO$_2$ catalyst at different reaction times (a), and after rejuvenation conducted after 22 h of reaction (b).

Only methane formation was detected by the signal (m/e = 15). Analysis of variation of the m/e = 28 signal during TPH suggests that no higher hydrocarbons were produced. A broad methane peak in the temperature range of 85 °C – 280 °C was observed in the TPH profile after the catalyst exposure to syngas during the first 15 min of reaction. As the reaction proceeds, two phenomena occurred. The intensity of the main broad peak decreases, while additional peaks appear at higher temperatures. The formation of carbon species calculated by the peaks of TPH-MS is given in Table 5.2.

The presence of several TPH peaks can be attributed to different carbon species present on the catalyst surface. It is interesting to note that the concentration of carbon species determined by TPH is significantly smaller than the decrease in the number of CH_x species during the deactivation. Previously, formation of carbon species on cobalt catalysts during the FT catalytic tests in a slurry reactor was studied in a greater detail by Peña et al. [8, 13]. The methane production peaks observed at 250 °C were attributed to hydrogenolysis of adsorbed hydrocarbon fragments, including CH_x species yielding methane on hydrogenation.

Table 5.2 Concentration of carbon species observed by TPH MS with SSITKA (1 atm, 250 °C, $H_2/CO = 2$, GHSV = 10 800 mL/g h). Rejuvenation conditions are given in Table 5.1.

Time on stream	Concentration of carbon species (µmol/g)		R_{SSITKA} (µmol/g s)
	Peak A: 85 °C – 280 °C	Peak B: 310 °C – 450 °C	
10 min	2.89	-	2.88
1 h	2.34	0.66	2.19
22 h	1.95	1.19	1.2
Rejuvenated sample	2.28	0.37	2.89

_____

These adsorbed hydrocarbons are not likely relevant to catalyst deactivation. The high temperature peaks at 300-350 °C were assigned to more strongly adsorbed hydrocarbons probably located inside the catalyst pores. Those suggestions are consistent with the data of Moodley [12] and Gruver [35]. In addition, it should be noted that the peaks at 250 °C might have been also assigned to the presence of cobalt carbide. Several in-situ studies [4, 6, 36, 37] were indicative of cobalt carbide formation under the conditions of FTS. Surface cobalt carbide is, however, usually unstable after exposure to air and thus cannot be observed by the conventional TPH method [8, 12, 13].

5.2.4 Catalyst rejuvenation

A noticeable decrease in carbon monoxide conversion (Figure 5.2) was observed during FTS, which suggests catalyst deactivation. Catalyst rejuvenation was conducted at 250 °C during 2 h using the H_2/N_2 (5:6) gas mixture. After rejuvenation, the flow of syngas (H_2/CO ratio = 2) was reestablished to the catalyst bed. It can be expected that the rejuvenation in hydrogen can reduce the concentration of carbon species formed on the catalysts during FT reaction and recover the catalytic activity. Indeed, rejuvenation in hydrogen resulted in a higher FT reaction rate (Table 5.3).

Table 5.3 SSITKA results obtained during reaction after rejuvenation.
Reaction conditions: 1 atm, 250 °C, H_2/CO = 2, GHSV = 10 800 mL/g h.
Rejuvenation conditions: 1 atm, 250 °C, during 2h, H_2/N_2=5/6, GHSV = 13 200 mL/g h.

Time of reaction after H_2 rejuvenation	τ_{CO} (s)	τ_{CH4} (s)	N_{CO} (µmol/g)	N_{CH4} (µmol/g)	XCO
10 min	5.5	16.8	53.6	48.6	30%
1 h	5.2	17.6	53.6	44.3	22%

The influence of catalyst rejuvenation in hydrogen on the number and reactivity of the surface intermediates was studied using SSITKA. The $^{12}CO/H_2/He/Ne$ to $^{13}CO/H_2/He$ switches were realized after 10 min and 1 h of reaction over the rejuvenated catalyst. Table

5.3 and Figure 5.8 show that both the concentration and residence time of surface intermediates were affected by the rejuvenation. Interestingly, the concentration of the reversibly adsorbed CO molecules was not significantly changed, while the concentration of CH_4 surface intermediates leading to methane (N_{CH_4}) almost doubled after conducting the rejuvenation. This suggests that treatment in hydrogen results in hydrogenation of carbon species, which can block the sites responsible for methane formation.

In addition, the CH_4 residence time decreases after the rejuvenation, while CO residence time slightly increases after the rejuvenation. The decrease in CH_4 residence time could be indicative of a higher CH_4 hydrogenation rate in the rejuvenated sample, while the increase in CO residence time suggests reemergence of stronger sites for reversibly adsorbed CO.
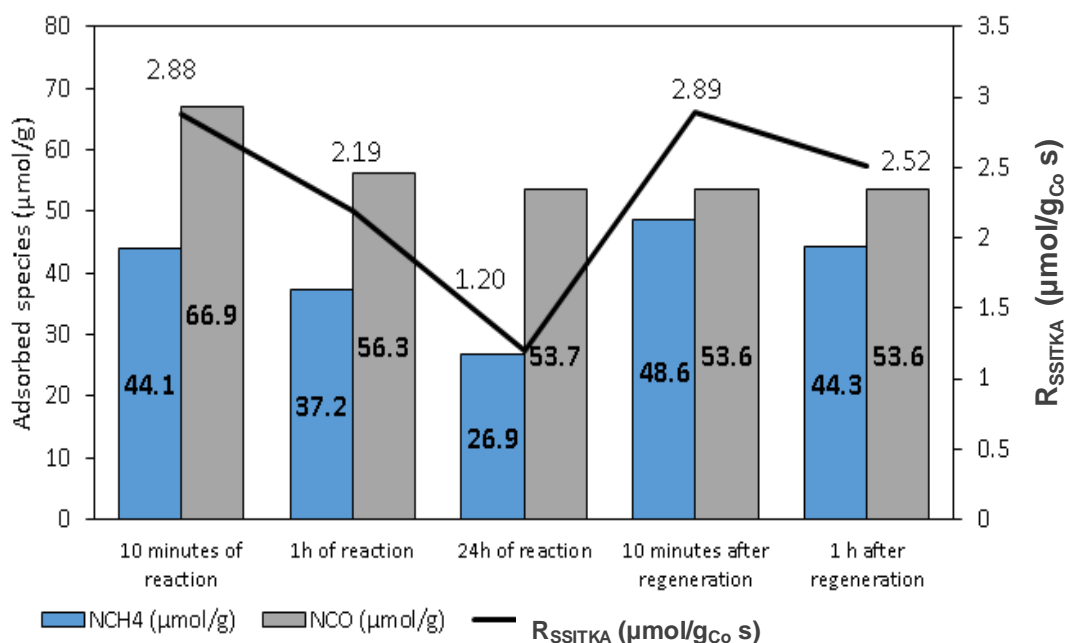
Figure 5.8 SSITKA parameters before and after H_2 rejuvenation (Reaction: 250 °C, H_2/CO ratio = 2, 1 atm, GHSV= 10 800 mL/g h; rejuvenation: 250°C, 2 h, 1 atm, H_2/N_2 = 5/6.

Exposure of the regenerated catalyst for 1 h to the FT reaction conditions again leads to a decrease in the number of CH_4 intermediates and a slight increase in CH_4 residence time (Figure 5.8, Table 5.3). This probably corresponds to a built up of carbon

species, blocking the most active surface hydrogenation sites and lowering the hydrogen surface coverage. Similar phenomena occurred on the cobalt catalyst during the initial episodes of FTS with the freshly activated catalyst.

The catalyst regenerated in hydrogen was characterized by TPH-MS (Figure 5.7b). Compared to the catalyst before rejuvenation, the regenerated sample showed preferential removal of carbon species, which exhibit high temperature TPH peaks and which can probably block the surface hydrogenation sites. On the one hand, TPH profiles conducted with the spent catalysts which have been exposed to syngas even for a relatively short time, show methane production peaks which can be attributed to hydrogenation of deposited carbon species. Exposure of the cobalt catalyst to FT reaction conditions for a longer time results in a progressive increase in the fraction of more difficult to hydrogenate carbon species.

Carbon deposition seems to result in blocking of the most active FT sites located on the steps and edges of cobalt nanoparticles and thus leads to a major drop in the FT reaction rate. Carbon species deposited on the cobalt steps seem to be more strongly bonded to the surface. They exhibit high temperature TPH peaks and are more difficult to hydrogenate than those located on cobalt terraces.

Some hypotheses about the structure of the most active cobalt sites can be built on the basis of molecular modeling. Recently conducted DFT calculations [38, 39] suggest that direct carbon monoxide dissociation is more difficult on cobalt flat terraces such as (0 0 0 1) where the CO activation can only proceed through the H-assisted pathway [40, 41, 42]. However, the sites situated on the steps of cobalt particles can be more efficient in CO activation. Several reports indicate [38, 39, 43] that CO dissociation on these sites can even occur directly without participation of hydrogen.

Catalyst treatment in hydrogen results in some recovery of the catalytic activity (Figure 5.8). The concentration of carbon species exhibiting a TPH methane peak at 350 °C was also slightly reduced after catalyst rejuvenation in hydrogen. The surface residence time of CH_x species also decreases after the rejuvenation. This also suggests partial recovery of the most active sites after hydrogen treatment.

5.2.5 Kinetic modeling

In order to understand the effect of the deactivation phenomena on methanation reaction pathway and consequently on the values of rate constants of each mechanism, SSITKA modeling study was performed using the PFR approach with an set of PDE (see Chapter 2). The Table 5.4 shows the structure parameters of cobalt supported on silica used in the set of the partial differential equations (PDE) applied on EMSO software.

Table 5.4 Parameters of the PDE set of equation applied on the EMSO software.

CoPt/SiO$_2$[a] (kg/m^3)	Inert SiC[a] (kg/m^3)	Catalyst bed porosity[b] (m$^3_{gas}$/m$^3_{reactor}$)	Density of catalyst bed (kg/m^3)	Surface residence time[c] (s)
2610.2	3197.9	0.97	796	0.37

The modeling approach described in Chapter 1 was used to estimate the kinetic parameters according to six different mechanisms (M1 to M6, see Figure 1.8 in Chapter 1). Figure 5.9 shows an example of the model fitting to the transient curves of ^{12}CO and $^{12}CH_4$, generated from SSITKA when applied after 1 h of operation.
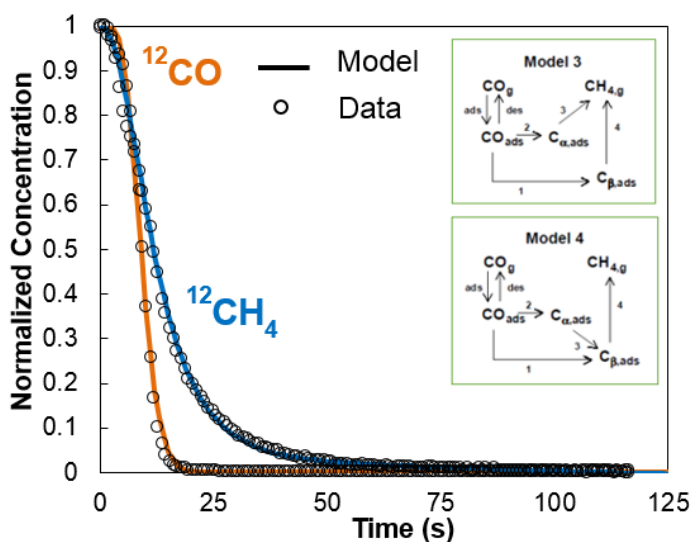

Figure 5.9 SSITKA data experimental and modeling results at 1h of reaction for M3 and M4.

_____

The same analysis was performed for SSITKA data generated after 1 h and 150 h of operation. A complete set of parameters for the three experiments according to the proposed mechanisms (M1 to M6) is given in Table 5.5.

Table 5.5 Estimated parameters for each relevant model and case (TOS = 1 h, 24 h and 150 h), including standard deviation (dev).

1 h of reaction	Model 1		Model 3		Model 4		Model 5	
	k	dev	k	dev	k	dev	k	dev
k ads (m^3/kg s)	4.63E-02	2.736E-03	5.67E-02	6.97E-03	4.69E-02	3.36E-03	4.63E-02	5.20E-03
k des (s^{-1})	1.721	1.011E-01	2.115	2.68E-01	1.744	1.29E-01	1.72	2.01E-01
k1 (s^{-1})	2.18E-02	2.836E-04	2.11E-02	5.74E-04	2.15E-02	3.40E-04	2.22E-02	3.95E-04
k2 (s^{-1})			1.24E-03	2.79E-04	5.18E-04	1.56E-04	7.11E-03	1.60E-03
k3 (s^{-1})			1.41E-02	1.09E-02	5.87E-03	4.21E-03	2.23E-02	1.43E-02
k4 (s^{-1})	1.16E-01	2.15E-03	1.22E-01	4.06E-03	1.20E-01	2.70E-03	1.20E-01	3.00E-03
Residual	**4.53E-04**		**4.28E-04**		**3.70E-04**		**4.03E-04**	
24 h of reaction	**Model 1**		**Model 3**		**Model 4**		**Model 5**	
	k	dev	k	dev	k	dev	k	dev
kads (m^3/kg s)	3.85E-02	2.29E-03	3.83E-02	3.17E-03	3.87E-02	2.65E-03	4.13E-02	3.23E-03
k des (s^{-1})	1.61	9.76E-02	1.60	1.35E-01	1.61	1.17E-01	1.73	1.381E-01
k1 (s^{-1})	1.86E-02	2.22E-04	1.76E-02	6.44E-04	1.81E-02	2.88E-04	1.89E-02	2.51E-04
k2 (s^{-1})			1.42E-03	4.12E-04	4.80E-04	8.19E-05	7.89E-03	3.16E-03
k3 (s^{-1})			1.69E-02	1.01E-02	7.68E-03	3.83E-03	2.62E-02	1.21E-02
k4 (s^{-1})	8.95E-02	1.57E-03	9.87E-02	3.65E-03	9.46E-02	1.99E-03	9.35E-02	2.21E-03
Residual	**3.42E-04**		**2.83E-04**		**2.69E-04**		**2.89E-04**	
150 h of reaction	**Model 1**		**Model 3**		**Model 4**		**Model 5**	
	k	dev	k	dev	k	dev	k	dev
kads (m^3/kg s)	3.44E-02	1.55E-03	3.95E-02	2.22E-03	3.64E-02	2.02E-03	3.20E-02	2.79E-03
k des (s^{-1})	1.89	8.85E-02	2.15	1.23E-01	1.976	1.13E-01	1.73	1.61E-01
k1 (s^{-1})	1.16E-02	9.02E-05	7.14E-03	5.73E-04	1.03E-02	2.01E-04	1.16E-02	1.00E-04
k2 (s^{-1})			4.53E-03	5.32E-04	7.69E-04	8.39E-05	5.32E-02	4.78E-03
k3 (s^{-1})			2.47E-02	1.87E-03	1.20E-02	2.02E-03	3.29E-02	1.05E-03
k4 (s^{-1})	4.82E-02	8.28E-04	7.67E-02	4.54E-03	5.84E-02	1.52E-03	6.30E-02	1.25E-03
Residual	**3.74E-04**		**1.53E-04**		**2.08E-04**		**1.32E-04**	

The results suggest that models M3, M4 and M5 gave the best fits and can be considered equivalent and indistinguishable regarding the prediction of $^{12}CH_4$ and ^{12}CO transient curves from a statistical point of view. Also, the three aforementioned models predict the same CO adsorbed concentration (C_{COads}) and rate of CH_4 formation for a given experiment.

Differences between the predictions from each model arise in the concentration of the adsorbed species. Figures 5.10-5.12 show respectively the model predictions for the total concentration of CO adsorbed (C_{COads}), concentration of carbon intermediate species (C_{ads}), and CH_4 formation rate as a function of the time on stream (1 h, 24 h, 150 h); the results are normalized using the corresponding values of the variables obtained in the experiment carried out at 1 h.

Experimental data for N_{CO}, N_{CH4} calculated from SSITKA and activity are plotted in Figures 5.10, 5.11 and 5.12 respectively; these parameters can be correlated to the aforementioned variables predicted by the model. Interestingly the models predict a decrease in the number of adsorption CO sites and in the methane production (related to activity) at longer time of stream. Models M1, M3, M4 and M5 give the same predictions for concentration of adsorbed CO and CH_4 formation rate; the dependence of these parameters with the time on stream is in agreement with the experimental results of N_{CO} (Figure 5.10) and activity (Figure 5.11) versus time on stream.
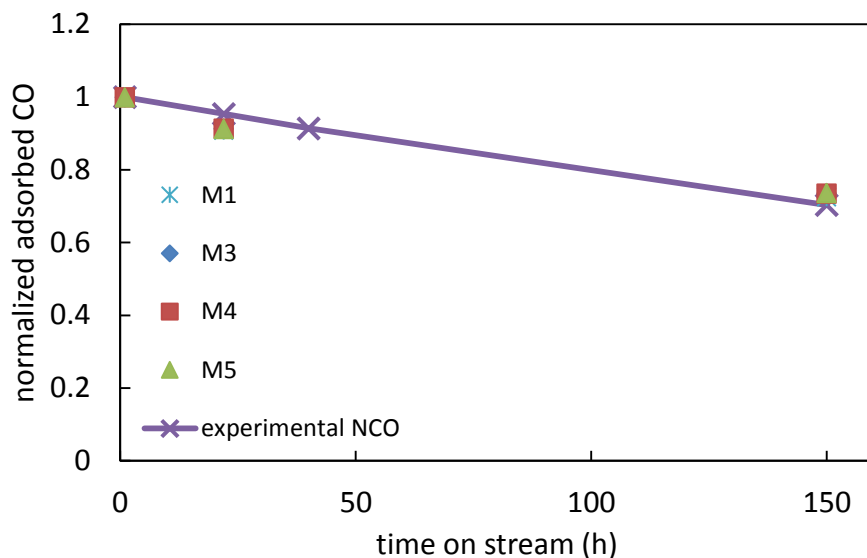
Figure 5.10 Predicted concentration of adsorbed CO according M1, M3, M4 and M5 models and experimental values of N_{CO} as function of time on stream. Results are normalized by their corresponding value at 1 h.
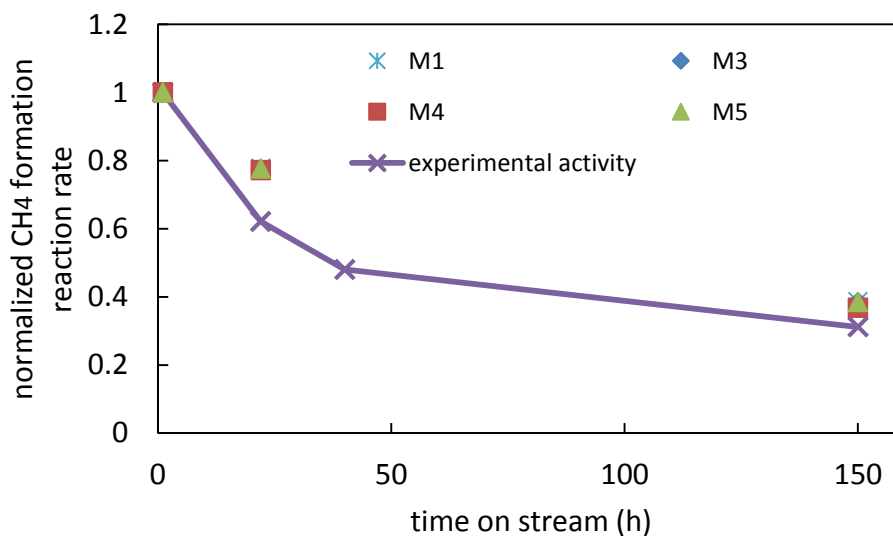
Figure 5.11 Predicted concentration of CH_4 formation rate according M1, M3, M4 and M5 models and experimental values of activity as function of time on stream. Results are normalized by their corresponding value at 1 h.

However, models M1, M3, M4 and M5 give different predictions regarding the concentration of adsorbed intermediate carbon species (Figure 5.12). Models M1 (one single pool of intermediates) and M3 and M5 (two pools of intermediates) predict small changes in the concentration of adsorbed intermediates as time on stream increases. Model M4 (two pools of intermediates) predicts slightly larger changes, showing better agreement with the observed experimental value of N_{CH4} at150 h of reaction.
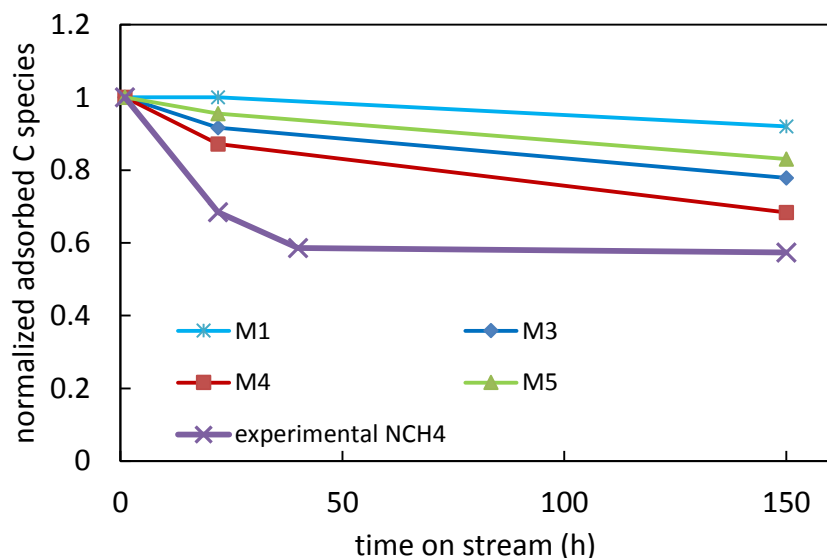
Figure 5.12 Predicted concentration of adsorbed intermediate species according M1, M3, M4 and M5 models and experimental values of N_{CH4} as function of time on stream. Results are normalized by their corresponding value at 1 h.

There are some differences also in the concentration of each adsorbed intermediate species $C_{\alpha,ads}$, $C_{\beta,ads}$ predicted by models M3, M4 and M5. These models could be further discriminated using these differences along with additional surface characterization and/or theoretical analysis. Despite the quantitative differences, these different models exhibit several common features regarding the dependence of predicted reaction rates and concentration of intermediates on the time on stream. The predicted values for total $C_{\alpha,ads}$, $C_{\beta,ads}$ and individual reaction rates as a function of time (1 h, 24 h and 150 h) for models M3 and M4 are presented in Figures 5.13 and 5.14, respectively.

_____

a   **b**
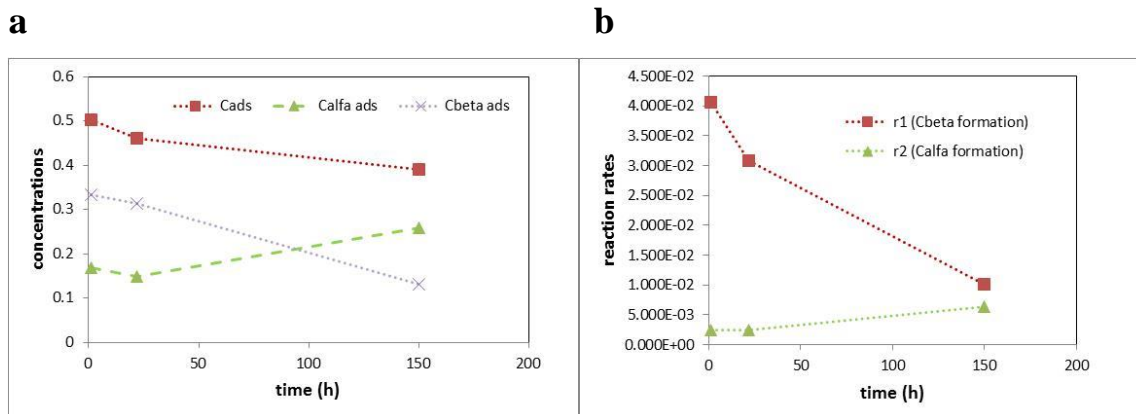
Figure 5.13 Predicted (a) concentration of adsorbed intermediate species and (b) individual reaction rates (parallel routes for formation of Cα,ads and Cβ,ads from CO adsorbed) according model M3, as function of time on stream.

a   **b**
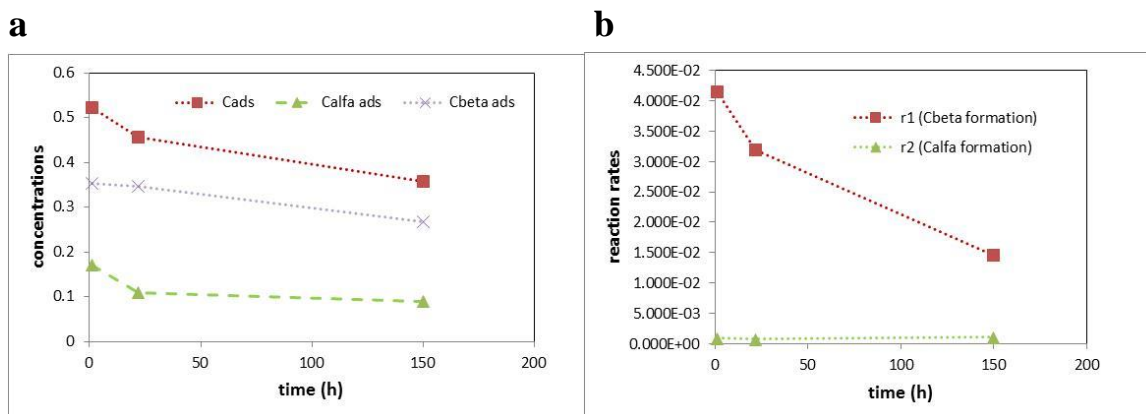
Figure 5.14 Predicted (a) concentration of adsorbed intermediate species and (b) individual reaction rates (parallel routes for formation of Cα,ads and Cβ,ads from CO adsorbed, however, Cβ,ads is also formed from Cα,ads in a consecutive reaction) according model M4, as function of time on stream.

These results show that one of the intermediate species is predominant (present in larger amounts), and most importantly, the rate of formation of the predominant intermediates from adsorbed CO (and consequently, subsequent formation of CH_4 through the corresponding route) is significantly much higher than for the other minority intermediate. In addition, the predominant route of formation of C intermediate is affected by the deactivation as time on stream proceeds, as seen in Figures 5.13 and 5.14.

The surface coverage is lumped in the kinetic constants as usually done in models for analyzing SSITKA transient responses using $^{12}C/^{13}C$ switches. Consequently, as showed by Van Dijk et al. [53], the kinetic parameters should depend on the H_2/CO feed

ratio used in the experiment (apart of other variables as temperature, for example). Considering that we were using the same H_2/CO ratio and other conditions as well throughout the 150 h-long experiment, this approach can be safely applied individually at each instant of time on stream and application of switches.

Analysis shows that the M1, M2, M5 and M6 models are equivalent and undistinguishable from a statistical point of view. In agreement with previous reports [55, 56], the M3 and M4 models (which consider the existence of two intermediate carbon pools) have given the best fits based on the smaller values of the weighted residuals for all sets of experiments.

As pointed out in previous studies [55, 56], these models could be further discriminated using the differences in the predictions along with additional experimental characterization and/or theoretical calculations. Interestingly, models M3 and M4 remain the most appropriate to describe the SSITKA responses even for the deactivated catalysts after exposure to syngas for a longer time on stream. These two models predict decay in the concentrations of reversible adsorbed carbon monoxide molecules and CH_x intermediates with time on stream. The relative fraction of two carbon polls is affected however differently in M3 and M4 models during the deactivation (Figures 5.13 and 5.14).

5.2.6 Catalytic performance of alumina supported cobalt catalyst in pure syngas and after ammonia treatment

Catalyst deactivation can be also due to the presence of nitrogen compounds in the syngas feed. The present section addresses the impact of addition of small amounts of acetonitrile and ammonia (1500 and 2500 ppmv) to the syngas feed on the catalytic performance of supported cobalt catalysts. In particular, the effects of co-fed ammonia on the catalyst performance and concentration and intrinsic activity of cobalt surface sites are discussed using SSITKA.

FT catalytic data obtained in the presence of ammonia over cobalt catalysts are presented in Figures 5.15-5.17. In the case of co-fed with acetonitrile, it was observed that acetonitrile is not stable at the reaction conditions in the presence of water. It undergoes hydrolysis into acetic acid and ammonia with subsequent partial decomposition of acetic acid into methane and CO_2: $CH_3CN + 2H_2O = CH_3COOH + NH_3 = NH_3 + CO_2 + CH_4$ [53]. The Co based catalysts almost do not produce carbon dioxide during FTS. Some slight increase in CO_2 on cobalt catalysts in the presence of added CH_3CN may indicate partial decomposition of acetonitrile. Aqueous ammonia (30 wt. %) also has been added in order to check the main effect of acetonitrile as the source of ammonia [53].

The catalyst activation was performed by hydrogen flow of 8 mL/min at 400 ºC for 3 h. In the CO hydrogenation with pure syngas at reaction conditions of H_2/CO of 5, 220 °C and atmospheric pressure, 13 h of reaction was conducted before the periodic switches from $^{12}CO/H_2/He/Ne$ to $^{13}CO/H_2/He$. In the experiment with NH_3 treatment, the cobalt catalyst was exposed to the flow of gaseous NH_3 at 220 ºC and atmospheric pressure for 2 h. After that, the ammonia flow was interrupted and the syngas in ratio feed of H_2 to CO equal to 5 was directed to the catalyst. After conducting the 13 h of reaction at the same reaction conditions, switches from $^{12}CO/H_2/He/Ne$ to $^{13}CO/H_2/He$ were performed. The CO conversion behavior for $CoPt/Al_2O_3$ with and without treatment is displayed in Figure 5.15.
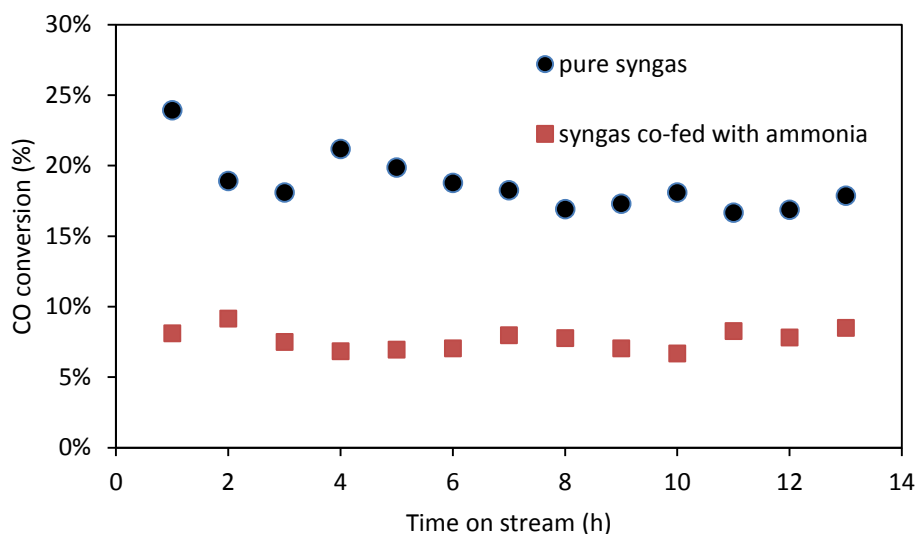
Figure 5.15 CO conversion as a function of time on stream for CoPt/Al$_2$O$_3$ without and with treatment with NH$_3$. Reaction conditions: 1 atm, 220 °C, H$_2$/CO = 5, GHSV = 14 400 mL/g h.

According to Figure 5.15, the catalytic performance is significantly affected by nitrogen containing compounds. The addition of saturated NH$_3$ led to a significant drop in CO conversion in comparison with the non-treated cobalt catalyst (from 24 % to 8 % at 1 h of reaction). Even after 13 h on stream, the CO conversion on the sample without NH$_3$ treatment is the double in comparison with NH$_3$ treated cobalt catalyst. Methane and C$_2$-C$_4$ hydrocarbons were the major products of CO hydrogenation.

Figure 5.16 shows methane selectivity as a function of time on stream. Methane formation is practically the same on the cobalt catalysts with and without treatment with NH$_3$ during the whole time on stream.
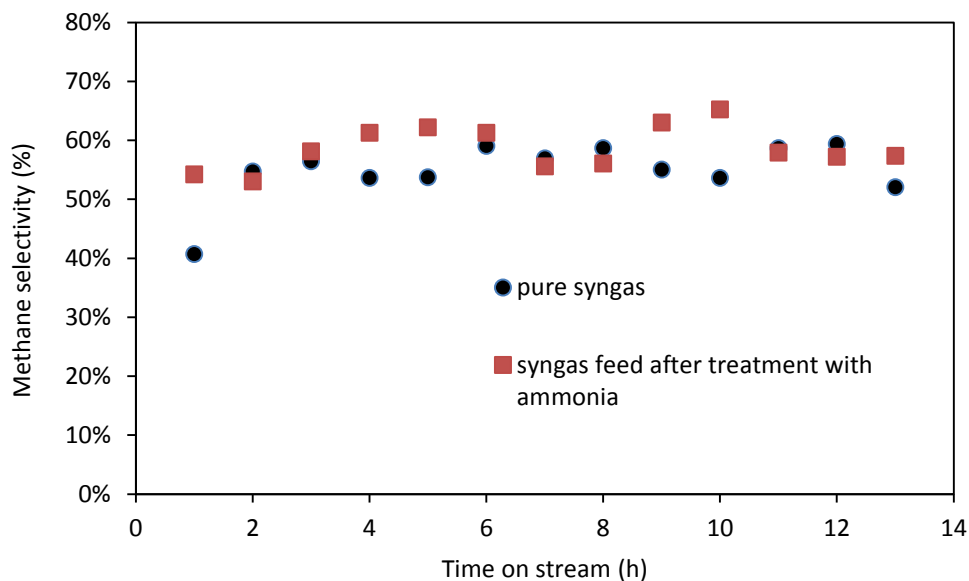
Figure 5.16 Methane selectivity as a function of time on stream for CoPt/Al$_2$O$_3$ treated with pure syngas and ammonia.

Figure 5.17 demonstrates that the selectivity for C$_2$-C$_4$ hydrocarbons is only very slightly altered for the catalyst with ammonia treatment (likewise to the methane selectivity behavior). However, as showed in Figure 5.15 the CO conversion level obtained was different, which makes such comparison not so reliable.

Figure 5.17 C$_2$-C$_4$ hydrocarbon selectivity as a function of time on stream in CoPt/Al$_2$O$_3$ with pure syngas and ammonia treatment.

The hydrocarbon selectivities and C_2-C_4 olefin to paraffin ratios as functions of carbon monoxide conversion on cobalt catalysts are shown in Figure 5.18. Introduction of acetonitrile and ammonia leads to lower carbon monoxide conversions (at similar GHSV) and lower FT reaction rates during and 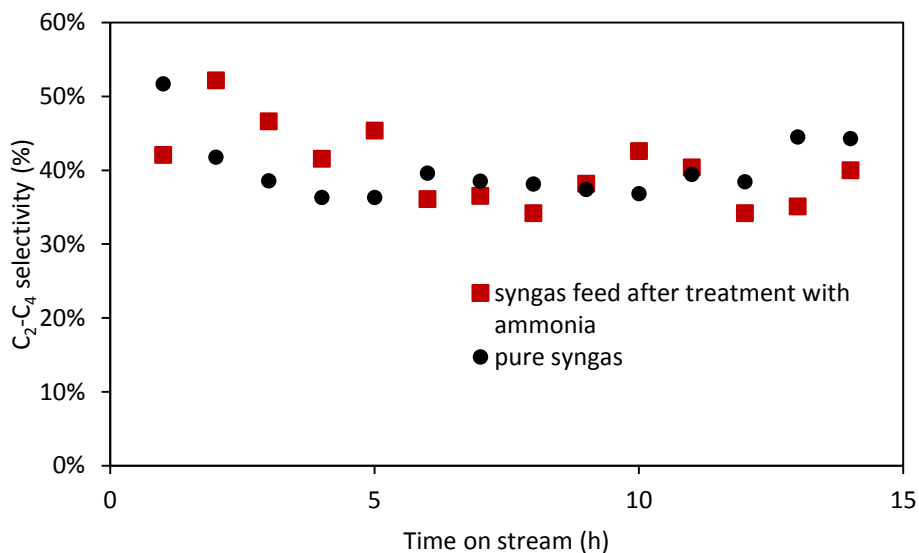after CH_3CN and NH_3 addition compared to pure syngas. Interestingly, the methane and C_{5+} hydrocarbon selectivities were respectively much lower and higher at the same conversion levels on the supported cobalt catalysts during and after addition of the nitrogen containing compounds. Previously, similar effects on hydrocarbon selectivities on cobalt catalysts were observed after addition of small amounts of water [26, 44, 45, 46] and ammonia [25] to the syngas feed. One of the possible explanations of these phenomena could be selective poisoning of cobalt methanation sites by added ammonia and its derivatives.

The olefin to paraffin ratio is also affected by co-feeding. The olefin to paraffin ratio at similar carbon monoxide conversions significantly increases. The decrease in methane selectivity is accompanied by higher olefin to paraffin ratio which could result from the lower hydrogenation activity in the presence of ammonia. Note that the effect of added acetonitrile and ammonia on the reaction selectivity was rather irreversible on cobalt catalysts. The return to pure syngas after switching off acetonitrile and ammonia cofeeding does not result in full recovering the C_{5+} and methane selectivities to the values observed with the fresh catalyst in pure syngas (Figure 5.18). Only the olefin/paraffin ratio almost comes to the same values as they were before addition of N-containing compounds.

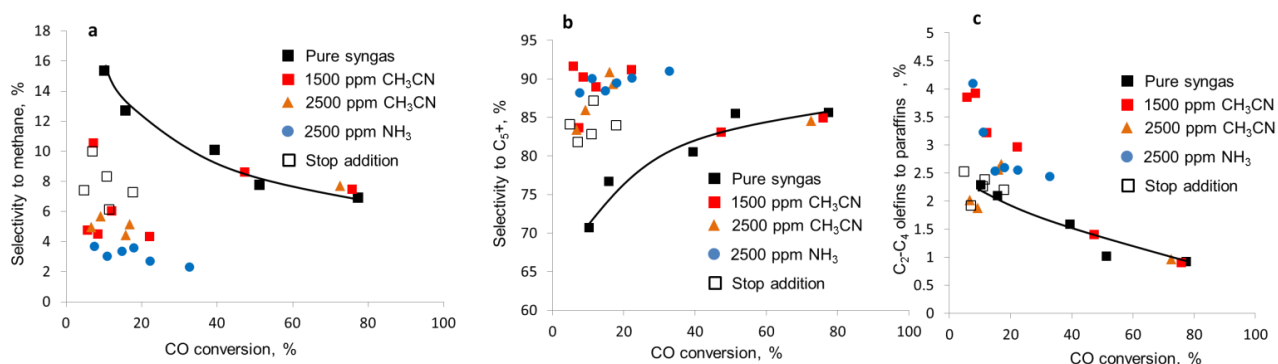**Figure 5.18** Methane (a), C_{5+} hydrocarbon (b) selectivities and C_2-C_4 olefins to paraffins ratios (c) measured on supported cobalt catalysts as functions of carbon monoxide conversion in the presence of added acetonitrile and ammonia.

Literature has provided some information about the effect of ammonia treatment on catalyst performance. Borg et al. [33] noticed no effect of ammonia on the catalytic performance of alumina and titania supported catalysts in the presence of 4 ppm of NH_3 in syngas. On the other hand, Pendyala et al. [34] observed a significant irreversible catalyst deactivation due to the effect of addition of ammonia for platinum promoted cobalt/alumina catalysts. In addition, in the presence of ammonia, the catalyst exhibited lower methane and higher C_{5+} hydrocarbon selectivity, which were attributed to selective poisoning of the methanation sites. Le Vinnes et al. [24] found that nitrogen compounds produce reversible effect on the catalytic performance of cobalt catalysts. The procedure in pure hydrogen was adopted to restore the catalyst activity.

The decrease in reaction rate can be due to the decrease in the concentration of active sites or to the decrease in the site intrinsic activity (Turnover Frequency). Note that both phenomena can occur simultaneously during the catalyst deactivation. Unfortunately, the steady state catalytic data do not allow discriminating between these different deactivation mechanisms.

SSITKA [47, 48, 49] addresses measuring the transient response of isotopic labels in the reactor following an abrupt change (switch) in the isotopic composition of one of the reactants. The switch involves only isotopic composition of the feed, while chemical composition remains unchanged. SSITKA provides independent information about the concentration of surface intermediates and their reactivity and thus it can be extremely helpful in elucidation of the mechanism of catalyst deactivation.

In order to provide further insights into the modification of the active sites due to treatment with ammonia, the catalysts were characterized by SSITKA. Table 5.6 shows SSITKA data for the catalysts treated and non-treated with ammonia.

Table 5.6 SSITKA and GC data for $Co25\%0.1\%Pt/Al_2O_3$ catalyst without and with NH_3 treatment.

Experiment with $Co25\%Pt0.1\%/Al_2O_3$	τ_{CO} (s)	τ_{CH4} (s)	N_{CO} (μmol/g)	N_{CH4} (μmol/g)	R_{SSITKA} (μmol/g s)	FT rate constant 10^{-6} (mol/g_{cat} s)
without NH_3 treatment	8.2	21.4	92.0	25.4	1.19	3.36
with NH_3 treatment	8.6	29.2	105	18.8	0.64	1.13

The number of intermediates leading to methane has been reduced in the catalysts exposed to ammonia. This result is consistent with an increase in the surface lifetime of intermediates. Interestingly, no significant modification of the reversible carbon monoxide adsorbed (N_{CO}) was observed. This leads to conclude that ammonia adsorption proceeded on the most active sites responsible for hydrogenation.

The best SSITKA parameter to detect the effect of ammonia treatment is the R_{SSITKA} (see Table 5.6). The reason is the ability of R_{SSITKA} to incorporate the comportment of surface lifetime of intermediates and the actual amount of hydrogenation sites. Hence, it is possible to observe a significantly reduction in the rate constant for the cobalt catalyst submitted to NH_3 treatment. Same trend is detected for FT rate constant determined by GC analysis. Thus, ammonia co-fed to the catalyst can affect the number and intrinsic activity of active sites for FTS. These modifications can be possibly attributed to the formation of cobalt nitride in the presence of ammonia.

In order to further confirm formation of cobalt nitride, the catalysts after exposure to ammonia during the catalytic tests were characterized by TPD-MS. Figure 5.19 shows the TPD-MS profiles of the alumina supported catalysts after the catalytic tests with detection of m/e = 28. The TPD-MS profiles of all the spend catalysts exhibited sharp peaks at 300 °C measured using both m/e = 28 and m/e = 14 signals. It can be suggested that these sharp peaks observed at 300 °C correspond to desorption of nitrogen. This nitrogen can be produced from cobalt nitrate decomposition.

The amount of nitrogen calculated from the area of this peak correlates with the amount of reduced cobalt in the catalysts: the N/Co ratios were 0.46 for Co15%/Al$_2$O$_3$, 0.74 for Co15%0.1%Pt/Al$_2$O$_3$ and 0.73 for Co25%0.1%Pt/Al$_2$O$_3$. Cobalt nitride formation in the presence of ammonia has been reported in previous works [50, 51, 52].
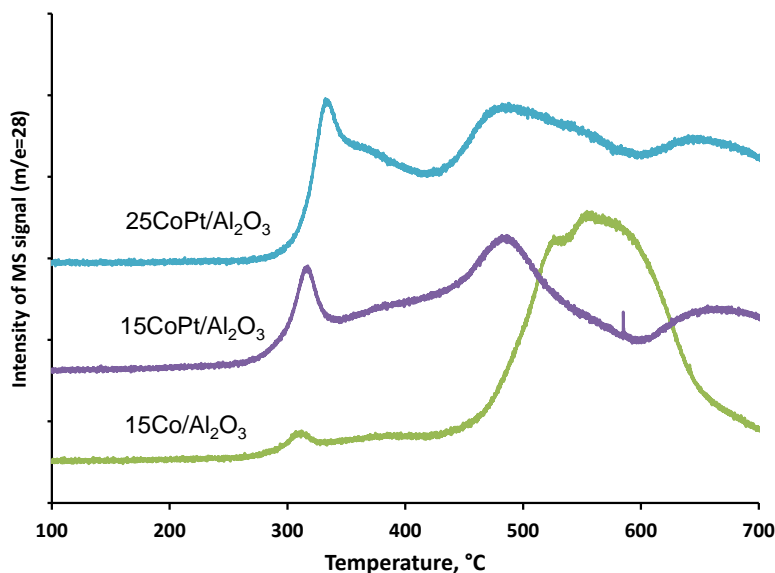
Figure 5.19 TPD-MS profiles of alumina supported cobalt catalysts after the catalytic tests with syngas containing acetonitrile.

The catalytic results obtained in this work suggest that cobalt nitride is not active in FTS. Indeed, formation of cobalt nitride during the catalyst exposure to acetonitrile leads to important catalyst deactivation. At the same time, cobalt nitride formation coincides with the modifications of FT catalyst selectivity patterns and leads to lower methane and higher C$_{5+}$ hydrocarbon selectivities. This suggests that the cobalt nitride formation proceeds selectively on the sites favoring methanation and block the most active cobalt hydrogenating sites.
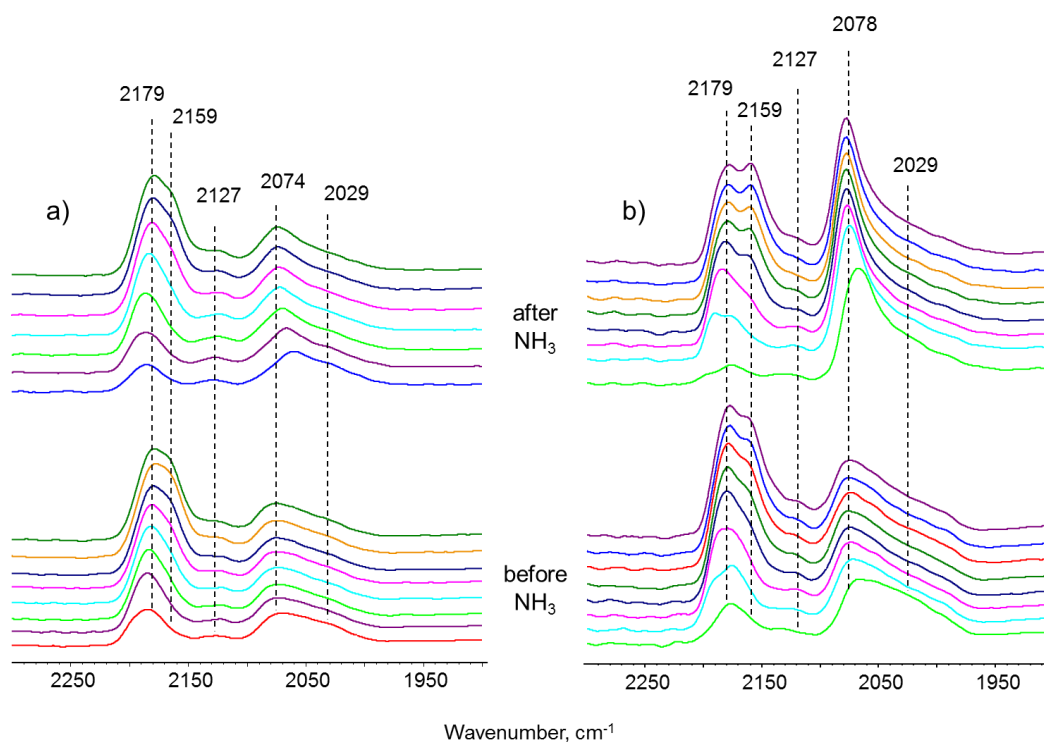
Figure 5.20 FTIR spectra of carbon monoxide adsorbed on the activated Co15%/Al$_2$O$_3$ (a) and Co25%0.1%Pt/Al$_2$O$_3$ (b) catalysts before and after exposure to NH$_3$.

Figure 5.20 shows the IR spectra of carbon monoxide adsorbed on the Co15%/Al$_2$O$_3$ and Co15%0.1%Pt/Al$_2$O$_3$ catalysts activated in hydrogen and then pre-treated with ammonia. The spectra exhibit a set of bands of adsorbed carbon monoxide. The broad band with the frequency from 2000 to 2100 cm^{-1} can be assigned to CO adsorption on cobalt sites, while the bands at 2179 and 2159 cm^{-1} seem to be attributed to CO adsorption on Lewis acid sites and hydroxyl groups of the alumina support, respectively.

Catalyst exposure to ammonia results in the modification of the shape of the broad low frequency CO band. In particular, the broad band gets narrower and contribution of the lower frequencies (νCO = 2029 cm^{-1}) branch is slightly reduced. This fact suggests that ammonia pre-treatment results in disappearance of electron enriched cobalt surface sites, associated with low-frequency shoulder.

Previous reports [53, 54, 55] attribute low frequency bands with the frequency of 2000-2030 cm^{-1} to the CO molecules in interaction with the edges or step sites of metal nanoparticles (Pt or Pd), while the band of CO with high frequencies (νCO = 2040-2060 cm^{-1}) corresponds to the adsorption on the terraces. It could be speculated therefore that cobalt nitride species could preferentially form on these highly unsaturated metal sites. The blockages of edges and steps of cobalt metal nanoparticles by nitrides could result in the decrease in the FT reaction rates and modify the reaction selectivity. Addition of platinum to the catalyst (Figure 5.19b) promotes this process and decreases the amount of unsaturated Co sites. Initially higher amount of active sites (bands at 2029 cm^{-1} in Figure 5.19a,b) leads to higher activity of Pt-promoted catalyst in comparison with unpromoted catalyst.

5.3 Conclusion

The SSITKA method combined with conventional catalytic tests and characterization of spent catalysts have provided new insights into the mechanisms of deactivation of silica supported cobalt catalysts for FTS. Exposure of cobalt catalysts to syngas under the methanation reaction conditions leads to carbon deposition and formation of cobalt nanoparticle agglomerates.

Catalyst deactivation in presence of pure syngas is accompanied by both a decrease in the number of cobalt active sites and their intrinsic activity for silica supported catalyst. Carbon deposition seems to preferentially occur on the most active cobalt sites presumably located on the steps and edges of cobalt nanoparticles and retards hydrogenation of CH_x adsorbed species. The sites favoring stronger reversibly adsorbed CO deactivate more rapidly during the reaction. Catalyst rejuvenation in hydrogen partially restores the most active methanation sites, while the sites for reversibly adsorbed carbon monoxide remain largely unaffected. Kinetic modeling suggests the presence of two carbon pools on the

catalyst surface, which are probably due to the sequential hydrogenation of adsorbed reactive carbon species to methane.

The addition of ammonia resulted in significant irreversible deactivation of alumina supported cobalt catalyst. It can be concluded that the ammonia treatment was responsible for the drop of the CO conversion due to the decrease in the number of intermediates leading to methane and the increase in the surface lifetime of intermediates. Ammonia seems to block the most active cobalt sites. The catalytic data were explained by irreversible formation of inactive cobalt nitrides in cobalt catalysts. Cobalt nitride possibly forms on the steps and edges of cobalt nanoparticles and selectively blocks the sites responsible for methanation. The intrinsic hydrogenation activity of cobalt sites decreases after cobalt nitride formation. Consequently, lower methane and higher C_{5+} hydrocarbon selectivities were observed on cobalt catalysts exposed to acetonitrile and ammonia.

_____

References

1.   van de Loosdrecht, J.; Ciobîcă, I. M.; Gibson, P.; Govender, N. S.; Moodley, D. J.; Saib, A. M.; Weststrate, K.-J.; Niemantsverdriet, J. W., Providing fundamental and applied insights into Fischer-Tropsch catalysis: Sasol-Eindhoven University of Technology collaboration. *ACS Catalysis* **2016**.

2.   Saib, A. M.; Moodley, D. J.; Ciobîcă, I. M.; Hauman, M. M.; Sigwebela, B. H.; Weststrate, C. J.; Niemantsverdriet, J. W.; van de Loosdrecht, J., *Catal. Today* **2010,** *154*, 271.

3.   Jacobs, G.; Das, T. K.; Zhang, Y.; Li, J.; Racoillet, G.; Davis, B. H., *Applied Catalysis A: General* **2002,** *233* (1–2), 263-281.

4.   Jacobs, G.; Ma, W.; Gao, P.; Todic, B.; Bhatelia, T.; Bukur, D. B.; Davis, B. H., *Catalysis today* **2013,** *214*, 100-139.

5.   van de Loosdrecht, J.; Balzhinimaev, B.; Dalmon, J. A.; Niemantsverdriet, J. W.; Tsybulya, S. V.; Saib, A. M.; van Berge, P. J.; Visagie, J. L., *Catalysis Today* **2007,** *123* (1–4), 293-302.

6.   Karaca, H.; Hong, J.; Fongarland, P.; Roussel, P.; Griboval-Constant, A.; Lacroix, M.; Hortmann, K.; Safonova, O. V.; Khodakov, A. Y., *Chemical Communications* **2010,** *46* (5), 788-790.

7.   Sadeqzadeh, M.; Chambrey, S.; Piché, S.; Fongarland, P.; Luck, F.; Curulla-Ferré, D.; Schweich, D.; Bousquet, J.; Khodakov, A. Y., *Catalysis Today* **2013,** *215* (0), 52-59.

8.   Pena, D.; Griboval-Constant, A.; Lecocq, V.; Diehl, F.; Khodakov, A. Y., *Catalysis today* **2013,** *215*, 43-51.

9.   Lancelot, C.; Ordomsky, V. V.; Stéphan, O.; Sadeqzadeh, M.; Karaca, H. l.; Lacroix, M.; Curulla-Ferré, D.; Luck, F.; Fongarland, P.; Griboval-Constant, A., *ACS Catalysis* **2014,** *4* (12), 4510-4515.

10.   Jacobs, G.; Das, T. K.; Patterson, P. M.; Li, J.; Sanchez, L.; Davis, B. H., *Applied Catalysis A: General* **2003,** *247* (2), 335-343.

11.   Jacobs, G.; Patterson, P. M.; Zhang, Y.; Das, T.; Li, J.; Davis, B. H., *Applied Catalysis A: General* **2002,** *233* (1), 215-226.

12.   Moodley, D. J.; van de Loosdrecht, J.; Saib, A. M.; Overett, M. J.; Datye, A. K.; Niemantsverdriet, J. W., *Applied Catalysis A: General* **2009,** *354* (1–2), 102-110.

13.   Peña, D.; Griboval-Constant, A.; Lancelot, C.; Quijada, M.; Visez, N.; Stéphan, O.; Lecocq, V.; Diehl, F.; Khodakov, A. Y., *Catalysis Today* **2014,** *228* (0), 65-76.

14.   Visconti, C. G.; Lietti, L.; Tronconi, E.; Forzatti, P.; Zennaro, R.; Rossini, S., *Catalysis Today* **2010,** *154* (3), 202-209.

15.   Ehrensperger, M.; Wintterlin, J., *Journal of Catalysis* **2015,** *329*, 49-56.

16.   Saib, A. M.; Gauché, J. L.; Weststrate, C. J.; Gibson, P.; Boshoff, J. H.; Moodley, D. J., *Industrial & Engineering Chemistry Research* **2013,** *53* (5), 1816-1824.

17.   Bambal, A. S.; Guggilla, V. S.; Kugler, E. L.; Gardner, T. H.; Dadyburjor, D. B., *Industrial & Engineering Chemistry Research* **2014,** *53* (14), 5846-5857.

18.   Sparks, D. E.; Jacobs, G.; Gnanamani, M. K.; Pendyala, V. R. R.; Ma, W.; Kang, J.; Shafer, W. D.; Keogh, R. A.; Graham, U. M.; Gao, P.; Davis, B. H., *Catalysis Today* **2013,** *215* (0), 67-72.

19.   Galvis, H. M. T.; Koeken, A. C. J.; Bitter, J. H.; Davidian, T.; Ruitenbeek, M.; Dugulan, A. I.; de Jong, K. P., *Catalysis today* **2013,** *215*, 95-102.

20.   Galvis, H. M. T.; Koeken, A. C. J.; Bitter, J. H.; Davidian, T.; Ruitenbeek, M.; Dugulan, A. I.; de Jong, K. P., *Journal of catalysis* **2013,** *303*, 22-30.

21.   Borg, Ø.; Hammer, N.; Enger, B. C.; Myrstad, R.; Lindvåg, O. A.; Eri, S.; Skagseth, T. H.; Rytter, E., *Journal of Catalysis* **2011,** *279* (1), 163-173.

22.   Pansare, S. S.; Allison, J. D., *Applied Catalysis A: General* **2010,** *387* (1), 224-230.

23.   Visconti, C. G.; Lietti, L.; Tronconi, E.; Forzatti, P.; Zennaro, R.; Rossini, S., *Catalysis Today* **2010,** *154* (3–4), 202-209.

24.   Leviness, S. C.; Mart, C. J., Slurry hydrocarbon synthesis with downcomer fed product filtration (LAW552). Google Patents: 1998.

25.   Pendyala, V. R. R.; Gnanamani, M. K.; Jacobs, G.; Ma, W.; Shafer, W. D.; Davis, B. H., *Applied Catalysis A: General* **2013,** *468*, 38-43.

26.   Ma, W.; Jacobs, G.; Sparks, D. E.; Pendyala, V. R. R.; Hopps, S. G.; Thomas, G. A.; Hamdeh, H. H.; MacLennan, A.; Hu, Y.; Davis, B. H., *Journal of Catalysis* **2015,** *326*, 149-160.

27.   Sango, T.; Fischer, N.; Henkel, R.; Roessner, F.; van Steen, E.; Claeys, M., *Applied Catalysis A: General* **2015,** *502*, 150-156.

28.   Saib, A. M.; Moodley, D. J.; Ciobîcă, I. M.; Hauman, M. M.; Sigwebela, B. H.; Weststrate, C. J.; Niemantsverdriet, J. W.; van de Loosdrecht, J., *Catalysis Today* **2010,** *154* (3–4), 271-282.

29.   Tsakoumis, N. E.; Rønning, M.; Borg, Ø.; Rytter, E.; Holmen, A., *Catalysis Today* **2010,** *154* (3–4), 162-182.

30.   Kalamaras, C. M.; Petallidou, K. C.; Efstathiou, A. M., *Appl. Catal., B* **2013,** *136–137*, 225.

31.   Khodakov, A. Y.; Peregryn, B.; Lermontov, A. S.; Girardon, J. S.; Pietrzyk, S., *Catalysis Today* **2005,** *106* (1), 132-136.

32.   Govender, N. S.; de Croon, M. H. J. M.; Schouten, J. C., *Applied Catalysis A: General* **2010,** *373* (1–2), 81-89.

33.   Karaca, H.; Safonova, O. V.; Chambrey, S.; Fongarland, P.; Roussel, P.; Griboval-Constant, A.; Lacroix, M.; Khodakov, A. Y., *Journal of Catalysis* **2011,** *277* (1), 14-26.

34.   Munnik, P.; De Jongh, P. E.; De Jong, K. P., *Journal of the American Chemical Society* **2014,** *136* (20), 7333-7340.

35.   Gruver, V.; Young, R.; Engman, J.; Robota, H. J., *Preprints-American Chemical Society. Division of Petroleum Chemistry* **2005,** *50* (2), 164-166.

36.   Claeys, M.; Dry, M. E.; van Steen, E.; du Plessis, E.; van Berge, P. J.; Saib, A. M.; Moodley, D. J., *Journal of Catalysis* **2014,** *318*, 193-202.

37.   Cats, K. H.; Weckhuysen, B. M.,. *ChemCatChem* **2016,** *8* (8), 1531-1542.

38.   Ge, Q.; Neurock, M., *The Journal of Physical Chemistry B* **2006,** *110* (31), 15368-15380.

39.   Gong, X.-Q.; Raval, R.; Hu, P., *Surface science* **2004,** *562* (1), 247-256.

40.   Inderwildi, O. R.; Jenkins, S. J.; King, D. A., *The Journal of Physical Chemistry C* **2008,** *112* (5), 1305-1307.

41.   Ojeda, M.; Li, A.; Nabar, R.; Nilekar, A. U.; Mavrikakis, M.; Iglesia, E., *The Journal of Physical Chemistry C* **2010,** *114* (46), 19761-19770.

42.   Tuxen, A.; Carenco, S.; Chintapalli, M.; Chuang, C.-H.; Escudero, C.; Pach, E.; Jiang, P.; Borondics, F.; Beberwyck, B.; Alivisatos, A. P., *Journal of the American Chemical Society* **2013,** *135* (6), 2273-2278.

43.   Huo, C.-F.; Li, Y.-W.; Wang, J.; Jiao, H., *The Journal of Physical Chemistry C* **2008,** *112* (36), 14108-14116.

44.   Borg, Ø.; Storsæter, S.; Eri, S.; Wigum, H.; Rytter, E.; Holmen, A., *Catal. Lett.* **2006,** *107*, 95.

45.   Storsæter, S.; Borg, Ø.; Blekkan, E. A.; Holmen, A., *Journal of Catalysis* **2005,** *231* (2), 405-419.

46.   Dalai, A. K.; Davis, B. H., *Applied Catalysis A: General* **2008,** *348* (1), 1-15.

47.   Legras, B.; Ordomsky, V. V.; Dujardin, C.; Virginie, M.; Khodakov, A. Y., *ACS Catalysis* **2014,** *4* (8), 2785-2791.

48.   Shannon, S. L.; Goodwin Jr, J. G., *Chemical reviews* **1995,** *95* (3), 677-695.

49.   Efstathiou, A. M.; Gleaves, J. T.; Yablonsky, G. S.; Che, M.; Vedrine, J. C., *Characterization of Solid Materials and Heterogeneous Catalysts: From Structure to Surface Reactivity*. 2012; p 1013.

_____

50.   Yao, Z.; Zhu, A.; Chen, J.; Wang, X.; Au, C. T.; Shi, C., *Journal of Solid State Chemistry* **2007,** *180* (9), 2635-2640.

51.   Marchand, R.; Tessier, F.; DiSalvo, F. J., *Journal of Materials Chemistry* **1999,** *9* (1), 297-304.

52.   Shi, Y.; Wan, Y.; Zhang, R.; Zhao, D., *Advanced Functional Materials* **2008,** *18* (16), 2436-2443.

53.   Wolter, K.; Seiferth, O.; Kuhlenbeck, H.; Bäumer, M.; Freund, H. J., *Surface Science* **1998,** *399* (2-3), 190-198.

54.   Kunimatsu, K.; Sato, T.; Uchida, H.; Watanabe, M., *Langmuir* **2008,** *24* (7), 3590-3601.

55.   Rainer, D. R.; Wu, M. C.; Mahon, D. I.; Goodman, D. W., *Journal of Vacuum Science & Technology A: Vacuum, Surfaces, and Films* **1996,** *14* (3), 1184-1188.

53 V.V. Ordomsky, A. Carvalho, B. Legras, S. Paul, M. Virginie, V.L. Sushkevich, A.Y. Khodakov, *Catal. Today* **2016**, 275, pp. 84-93

54 van Dijk, H. A. J.; Hoebink, J. H. B. J.; Schouten, J. C., *Chemical Engineering Science* **2001,** *56* (4), 1211-1219.54 -8.

55 Govender, N. S.; Botes, F. G.; de Croon, M. H. J. M.; Schouten, J. C., *Journal of Catalysis* **2008,** *260* (2), 254-261.

56 Yang, J.; Qi, Y.; Zhu, J.; Zhu, Y.-A.; Chen, D.; Holmen, A., *Journal of Catalysis* **2013,** *308* (0), 37-49.

Chapter 6. General conclusions and perspectives

The concept of active sites is central in heterogeneous catalysis and dates back to the pioneering works by Taylor in the 1920s. The catalytic performance of numerous catalysts is strongly affected by the number, intrinsic activity (Turnover frequency), localisation and stability of these active sites. The present thesis explores an approach to heterogeneous catalysis, which is based on the design and characterization of these active sites in cobalt and iron catalysts for syngas conversion reactions. Transient kinetics methods such as SSITKA alongside with extended catalyst characterization techniques were applied to evaluate the role of promoters for cobalt and iron catalysts, to elucidate the effect of different supports on the localization of active sites in cobalt-zeolite bifunctional catalysts, to provide further insights in catalyst deactivation-regeneration phenomena and their influence on the number and intrinsic activity of surface sties.

In Chapter 3, promotion of iron catalysts with soldering metals was used to enhance the activity of the catalyst active sites in direct olefin synthesis from syngas. Promotion led to scavenging of oxygen atoms sprouted on carbon monoxide hydrogenation and their migration in the catalysts. In the same chapter, SSITKA supplied interesting data about the effect of the zeolite on cobalt active sites and catalytic performance of cobalt catalysts.

In Chapter 4, we found that localization of cobalt active sites in bifunctional cobalt-zeolite catalysts had a major impact on the reaction rate and in particular on the hydrocarbons selectivity. The proximity between the cobalt active site and Brønsted active sites was a key parameter to obtain the higher selectivity and yield of isomerized hydrocarbons. A new original method for the design of the bifunctional catalysts

_____

containing cobalt metal nanoparticles in a close proximity with the acid sites based on the extraction with heterepoly acid was developed in this chapter.

SSITKA experiments and modeling were used to identify methane reaction mechanism as well to distinguish the manner how catalyst deactivation by carbon deposition and exposure to nitrogen containing compounds can influence the kinetics of elementary steps. Chapter 5 suggests that catalyst deactivation results initially at the deactivation of the most active sites in cobalt catalysts, which are probably located on the steps and edges of cobalt nanoparticles.

6.1 Promoter and support influence on the intrinsic catalytic activity of cobalt and iron FT catalysts

The knowledge concerning the manner how the catalyst promoters and supports affect the intrinsic catalytic activity is important for the appropriate catalyst design and then, for the catalyst performance optimization. In Chapter 3, iron and cobalt based catalysts with different composition were evaluated by SSITKA at different FT reaction conditions.

Promotion with Bi and Pb had a major effect on the catalytic activity, which increased 5-10 times compared to the unpromoted catalysts. The promoted catalysts exhibited noticeable catalytic activity even at atmospheric pressure. The both iron Bi-promoted and non-promoted produced carbon dioxide due to WGS. However, the iron non-promoted catalyst had lower CO_2 rate formation. The enhanced activity of the Bi and Pb promoted catalysts was attributed to a much easier removal of oxygen species formed on carbon monoxide dissociation by the promoters.

The SSITKA experiments also gave information about the total number of active sites in cobalt/zeolite catalysts. The amount of CO molecular adsorption in the promoted sample was higher than that for the non-promoted cobalt catalyst. Under CO hydrogenation reaction, a better catalytic performance was observed for the Pt-promoted cobalt catalysts at different partial pressures. SSITKA was capable to identify why Pt caused the activity increment. This occurred because Pt-promoter increased the number

_____

of intermediates leading to methane (N_{CH4}). One of the reasons responsible for these phenomena could better cobalt reducibility in the presence of platinum.

Higher concentration of sites was observed in CoPt/SiO$_2$. This may be attributed to better reducibility of larger cobalt particles. For the microporous ZSM-5 used as a support for cobalt, smaller amount of N_{CO} was found. Between the cobalt supported on the zeolites, CoPt/MOR demonstrated larger amount of active sites. TEM images of CoPt/BEA and CoPt/MOR showed that the cobalt nanoparticles for these catalysts are located inside and outside of the support surface. This was different to ZSM-5 which exhibited the cobalt nanoparticles only on the external surface of support.

SSITKA was capable to measure τ_{CH4} and N_{CH4} which were functions of the H$_2$/CO feed ratio for the CoPt/SiO$_2$, CoPt/BEA and CoPt/MOR catalysts. For CoPt/ZSM-5 there was only a slight effect of the H$_2$/CO ratio on τ_{CO}.

6.2 Synthesis of FT cobalt-zeolite composite catalysts using extraction with heteropoly acid

Impregnation is a well-known and easy method of catalyst preparation, however, it does not guarantee nanoparticle localization only inside of zeolite pores.

Chapter 4 demonstrates a new method for the synthesis of metal-zeolite composites. The method consists in a selective removal of metal non-incorporated in the pores of zeolite. It has been attained by dissolution of metal oxide nanoparticles from external surface of zeolite by bulky heteropoly acids. These large molecules cannot enter the pores of zeolites. New metal-composite materials has been applied in the FTS to produce isoparaffins from syngas in a single step. These new materials contained metallic and acid active sites in a close proximity in zeolite matrix.

Interesting phenomena were observed in terms of catalytic performance for the prepared cobalt-zeolite composites for FTS. The use of these catalysts resulted in significantly higher C$_5$-C$_{12}$ hydrocarbon fractions in the products in comparison with the parent catalysts with the maximum ratio of isoparaffins to n-paraffins. The proximity of

_____

metal and acid sites in the new composite catalysts was responsible of the selectivity improvements.

Figure 6.1 illustrates the effect of the heteropoly acid treatment in a cobalt-zeolite catalyst on the distribution of the metallic phase between the external and internal surfaces of the zeolite support.
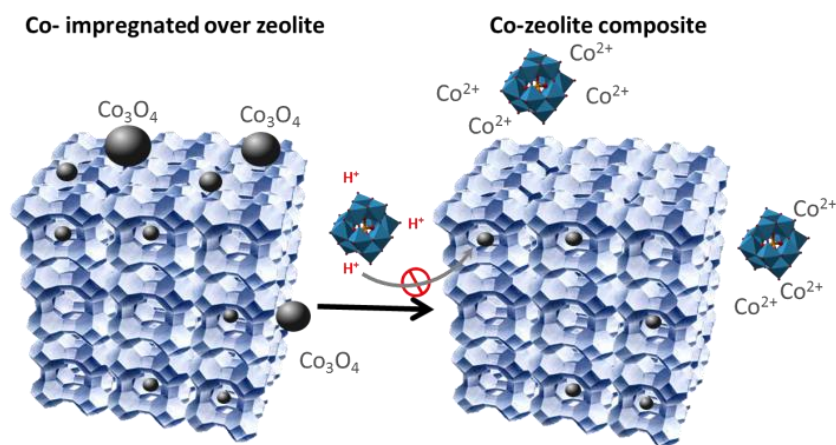

Figure 6.1 General scheme of the procedure for the synthesis of metal-zeolite composite material.

6.3 Elucidation of deactivation phenomena in cobalt catalysts for Fischer Tropsh synthesis using SSITKA

Deactivation is currently one of the most important challenges of FTS on cobalt catalysts, which reduces overall efficiency of the whole technology. Catalyst deactivation affects both catalyst structure and catalytic performance including the rate of elementary reaction steps.

The SSITKA method combined with conventional catalytic tests and extended characterization of spent catalysts have provided new insights into the mechanisms of deactivation of silica supported cobalt catalysts for FTS. Exposure of cobalt catalysts only to syngas under the methanation reaction conditions led to carbon deposition and formation of cobalt nanoparticle agglomerates. Catalyst deactivation was accompanied by both a decrease in the number of cobalt active sites and their intrinsic activity.

_____

The first mechanism of catalyst deactivation is relevant to carbon deposition on the most active cobalt sites presumably located on the steps and edges of cobalt nanoparticles and retards hydrogenation of CH_x adsorbed species. The sites favoring stronger reversibly adsorbed CO deactivate more rapidly during the reaction. It can be suggested that during deactivation the most active cobalt sites are selectively blocked by carbon. This leads to the lower overall activity, longer residence time of the reactive CH_x species and lower turnover frequency over the partially deactivated catalyst compared to the freshly activated one. The most active sites involved in FTS are probably those, which facilitate direct or hydrogen-assisted dissociation of CO. At longer time on stream, carbon deposition also occurs on less active cobalt sites not necessarily located on steps and edges of cobalt nanoparticles. This represents the second mechanism of catalyst deactivation.

The contribution of these two mechanisms to catalyst deactivation depends on the catalyst, operating conditions and reaction time. Note that these deactivation mechanisms can often operate simultaneously. In practice, it is rather difficult to distinguish between the deactivation mechanisms from the conventional catalytic tests. Figure 6.2 tentatively displays the buildup of carbon species on the steps of cobalt nanoparticles during the reaction and their partial removal after the catalyst rejuvenation in hydrogen.
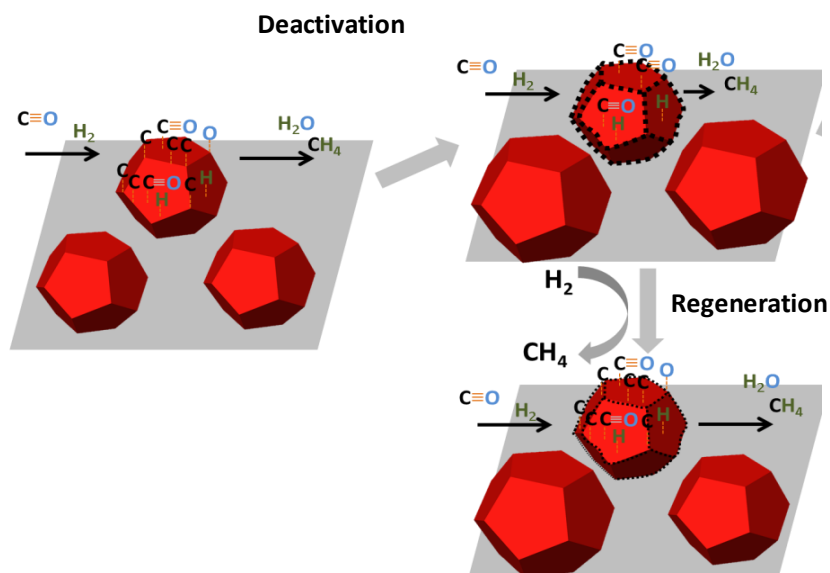

Figure 6.2 Preferential carbon deposition on the steps of cobalt nanoparticles and their removal during the rejuvenation.

_____

Six models were tested for the cobalt catalyst supported on silica using SSITKA experimental data of the deactivated cobalt catalyst. The objective was to reveal how the deactivation phenomena could affect the methanation routes and their kinetic constants of adsorption/desorption as well methane formation via intermediates. The models involving two carbon pools remain the most acceptable for both fresh and deactivated catalyst in terms of statistical analysis compared to other studied mechanisms.

The total amounts of adsorbed reactive carbon species decrease, though the ratio between the two carbon pools varies differently in these two models during the catalyst deactivation. Interestingly, catalyst deactivation involving carbon deposition and formation of cobalt nanoparticle agglomerates does not produce any significantly effect on the kinetic relevance of these models.

The study of poisoning for the cobalt catalysts with ammonia co-fed with syngas in the FTS using cobalt supported on alumina conducted with pure syngas showed a significantly drop in the carbon monoxide conversion. SSITKA technique showed lower amount of CH_4 intermediates for the catalyst treated with ammonia, however, no significant modification of the number of molecularly adsorbed CO molecules was observed. Therefore, it can be concluded that ammonia proceeds on the most active sites responsible for hydrogenation. These sites, as showed in Figure 6.3, are probably located on the steps and corners of cobalt nanoparticles. During the exposure to NH_3, these sites were blocked by the nitrogen species. The decay of the catalytic performance is explained by the irreversible formation of inactive cobalt nitrides in cobalt catalysts.
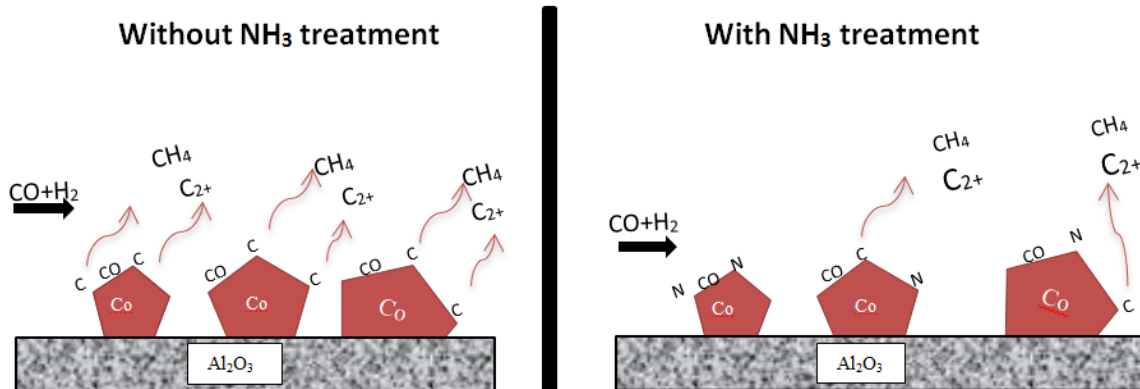
Figure 6.3 Effect of NH_3 treatment in the alumina supported cobalt catalyst. The poisoning of NH_3 blocked the steps and corner sites of cobalt particles causing the loss on catalytic activity.

Perspectives

The current thesis provided valuable information about the localization, activity and stability of active sites in cobalt and iron based FTS catalysts. We identified further studies that can be performed using SSITKA combined with catalyst characterization for the design and optimization of FT catalysts.
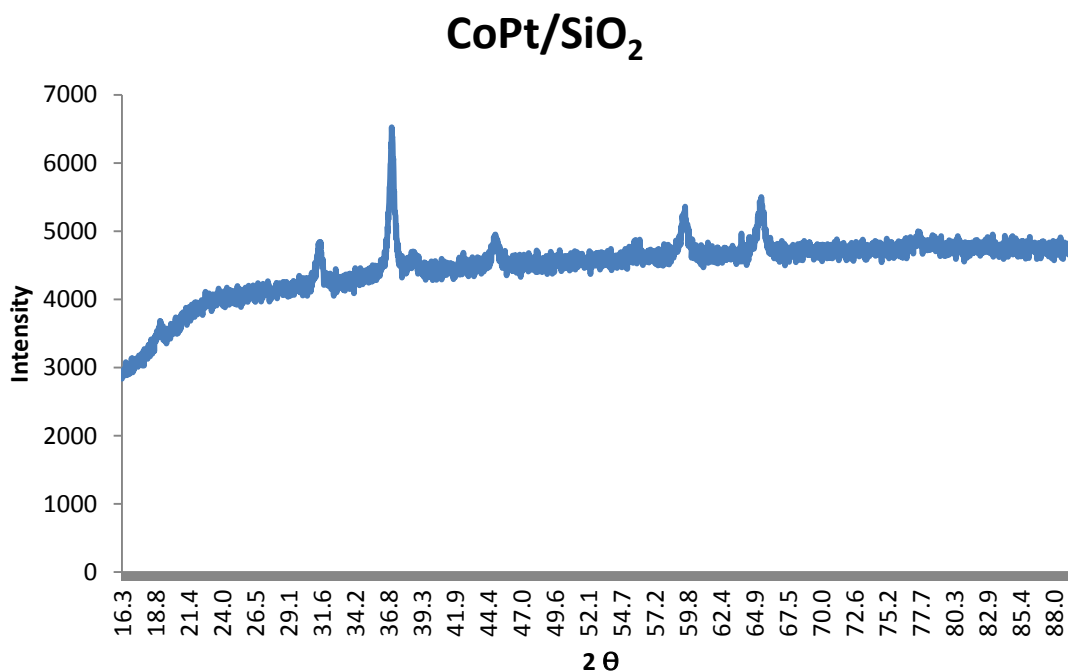
- Use of different isotope labels (D_2, ^{18}O) to perform FT experiments in order to obtain additional information about the reaction mechanism.
- DFT modeling of CO dissociation and oxygen scavenging.
- Heat and mass transfer studies.
- Application of different regeneration procedures (e.g. oxidation) at different times on stream during FTS.
- Use of other bulky acids for selective cobalt extraction for the zeolite outer surface in bifunctional catalysts.
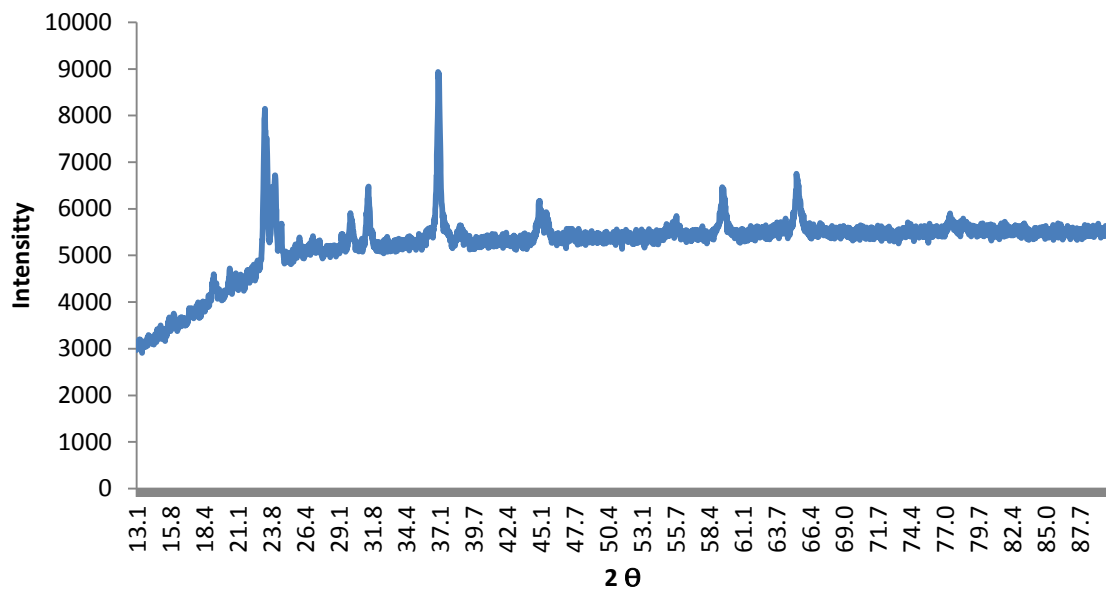
_____

APPENDIX 1

XRD patterns of the samples of cobalt catalysts supported on silica and zeolites ZSM-5, MOR and BEA are shown in Chapter 3.

XRD patterns were measured in the catalysts after calcination in air flow at 450°C during 7 h.

Integration of the peak of Co_3O_4 at 37.1° was done using Software Eva 4.0. The obtained value was used in the Scherrer Equation.

CoPt/SiO$_2$

_____

CoPt/ZSM-5

CoPt/MOR

_____

CoPt/BEA